The Dissertation Committee for Ruichen Zhao certifies that this is the approved version of the following dissertation:

Analysis, Modeling, and Control of Highly-Efficient Hybrid DC-DC Conversion Systems

Committee:

Alexis Kwasinski, Supervisor

William Mack Grady

Maruthi Akella

Aristotle Arapostathis

Mircea Driga

Analysis, Modeling, and Control of Highly-Efficient Hybrid DC-DC Conversion Systems

by

Ruichen Zhao, B.S.; M.S.

Dissertation

Presented to the Faculty of the Graduate School of

The University of Texas at Austin

in Partial Fulfillment

of the Requirements

for the Degree of

Doctor of Philosophy

The University of Texas at Austin

December 2012

Dedication

This work is dedicated to my loving parents:

Yingfang Zhao and Hefeng Ji.

Acknowledgements

I wish to thank my supervisor, Professor Alexis Kwasinski, for his supervision, support, and guidance. I am extremely grateful to the opportunities his has offered from the beginning to the end during my graduate study in the Power Electronics Research Group (PERG). Accepting me as a Ph.D. student, Dr. Kwasinski opened the door to this journey in the spring of 2008. The patience, freedom and flexibility from Dr. Kwasinski have allowed me to keep working and make it through. His constant trust and well-organized training in various aspects has allowed me to accumulate knowledge, improve research skills, and develop the ability of management. I am particularly grateful to Dr. Kwasinski for the lessons learned from painful but valuable mistakes in my graduate study. Thanks for his patience and guidance on my cavemanlike writing. I greatly appreciate the opportunities of two research projects during my Ph.D. study. I thank him for his support of my attendances of *ECCE* 2009/2011, *APEC* 2011, and *COMPEL* 2012. I also thank him for the freedom he gave to work with the Samsung Electronics in the summer of 2010. I am extraordinarily fortunate and honored to be supervised by such a professional, humble, and knowledgeable supervisor, indeed.

I convey special acknowledgement to other members of my doctoral committee: Profs. W. Mack Grady, Aristotle Arapostathis, Mircea Driga, and Maruthi Akella. Classes taught by Prof. Maruthi Akella and many discussions with him are very invaluable to my research in the UT Austin.

I am indebted to an experienced engineer, good lab mate and friend, Sheng-Yang Yu. Thanks to Sheng-Yang for sharing with me the knowledge, insight, and experimental

skills on power electronics; I highly appreciate the power electronics components generously provided by Sheng-Yang during my graduate study, too. The power from role models is endless. I always remember the time working with the role models, Dr. Chimaobi Onwuchekwa, from 2008 to 2011, and Mr. Greg Dahlberg, from 2011 to 2012. It was a pleasure to work with the pioneers of the PERG—Drs. Seunghoon Choung, Seunghyun Chun, Sungwoo Bae, and Junseok Song—and current fellow students—Harsha Kumar, Vaidyanathan Krishnamurthy, Amir Toliyat, Juyoung Jung, and Myungchin Kim. Thanks to Mr. Xingbin Zhao from Huazhong University of Science and Technology in China for the help with the printed circuit board design in spring 2011. Thanks to Ms. Christine McCourt for helping me to practice qualifying exam presentation in spring 2011. Thanks to Mr. Eric Dean for the help with the National Instruments software and hardware in spring 2012.

I would like to acknowledge the financial support from SolarBridge Technologies and the Office of Naval Research.

I'd like to express my gratitude to people in the Harbin Institute of Technology. Thanks to Profs. Shukang Chen, Shumei Cui, Qianfan Zhang, and my undergraduate advisor Prof. Ping Zheng, for their guidance on my undergraduate study. Thanks to Prof. Shujuan Wang for the inspirational course, *Electronics Technique*, which she taught in fall 2006. Thanks to Mr. Xi Ye for introducing me to *Carpe Diem*. Acknowledgments are owed to teachers in the Jiangsu Hualuogeng Junior and Senior Middle School where I

spent 6 years, from 1998 to 2004. I am also benefited from the education from Changsheng Elementary School and the care from Ms. Huijuan Wu from 1992 to 1997.

Many thanks go to my colleagues in Samsung Electronics. Particular thanks to Mr. Byungon Han for being such a great mentor and friend. Thanks to Mr. Soojung Lee and Mr. Mingjun Kim for their kind help during the internship. I would like to thank my future colleagues including but not limited to Mr. Randy Gold and Mr. Erwin Hernaez, for the opportunity to let me join Baker Hughes Incorporated.

Words fail me to express my appreciation to my parents. Thanks for their truly selfless love while watching their only child travel further and further geographically. Thanks for their encouragement since the days when I was very little. I can always feel the pride and love from their deep hearts. I express my sincerely gratitude to my fiancée, Yeyi Zhu, for her dedication, support, and love; for always trusting me and for all the sacrifices she has made; and for the warm and joyful life she has brought to me in this endeavor.

Finally, a lot of names have been left out. Credit is due to everyone who is important to the realization of this dissertation.

Analysis, Modeling, and Control Design of Highly-Efficient Hybrid DC-DC Conversion Systems

Zhao, Ruichen, Ph.D.

The University of Texas at Austin, 2012

Supervisor: Alexis Kwasinski

This dissertation studies hybrid dc-dc power conversion systems based on multiple-input converters (MICs), or more generally, multiport converters. MICs allow for the integration of multiple distributed generation sources and loads. Thanks to the modular design, an MIC yields a scalable system with independent control in all sources. Additional characteristics of MICs include the improved reliability and reduced cost. This dissertation mainly studies three issues of MICs: efficiency improvement, modeling, and control.

First, this work develops a cost-effective design of a highly-efficient non-isolated MIC without additional components. Time-multiplexing (TM) MICs, which are driven by a time-multiplexing switching control scheme, contain forward-conducting-bidirectional-blocking (FCBB) switches. TM-MICs are considered to be subject to low efficiency because of high power loss introduced by FCBB switches. In order to reduce the power loss in FCBB switches, this work adopts a modified realization of the FCBB switch and proposes a novel switching control strategy. The design and experimental verifications are motivated through a multiple-input (MI) SEPIC converter. Through the design

modifications, the switching transients are improved (comparing to the switching transients in a conventional MI-SEPIC) and the power loss is significantly reduced. Moreover, this design maintains a low parts-count because of the absence of additional components. Experimental results show that for output power ranging from 1 W to 220 W, the modified MIC presents high efficiency (96 % optimally). The design can be readily extended to a general *n*-input SEPIC. The same modifications can be applied to an MI-Ćuk converter.

Second, this dissertation examines the modeling of TM-MICs. In the dynamic equations of a TM-MIC, a state variable from one input leg is possible to be affected by state variables and switching functions associated with other input legs. In this way, inputs are coupled both topologically and in terms of control actions through switching functions. Coupling among the state variable and the time-multiplexing switching functions complicate TM-MICs' behavior. Consequently, substantial modeling errors may occur when a classical averaging approach is used to model an MIC even with moderately high switching frequencies or small ripples. The errors may increase with incremental number of input legs. In addition to demonstrating the special features on MIC modeling, this dissertation uses the generalized averaging approach to generate a more accurate model, which is also used to derive a small-signal model. The proposed model is an important tool that yields better results when analyzing power budgeting, performing large-signal simulations, and designing controllers for TM-MICs via a more precise representation than classical averaging methods. Analyses are supported by simulations and experimental results.

Third, this dissertation studies application of a decentralized controller on an MI-SEPIC. For an MIC, a multiple-input-multiple-output (MIMO) state-space representation can be derived by an averaging method. Based on the averaged MIMO model, an MIMO

small-signal model can be generated. Both conventional method and modern multivariable frequency analysis are applied to the small-signal model of an MI-SEPIC to evaluate open-loop and closed-loop characteristics. In addition to verifying the nominal stability and nominal performance, this work evaluates robust stability and robust performance with the structured singular value, μ. The robust performance test shows that a compromised performance may be expected under the decentralized control. Simulations and experimental results verify the theoretical analysis on stability and demonstrate that the decentralized PI controller could be effective to regulate the output of an MIC under uncertainties.

Finally, this work studies the control of the MIMO dc-dc converter serving as an active distribution node in an intelligent dc distribution grid. The unified model of a MIMO converter is derived, enabling a systematical analysis and control design that allows this converter to control power flow in all its ports and to act as a power buffer that compensates for mismatches between power generation and consumption. Based on the derived high-order multivariable model, a robust controller is designed with disturbance-attenuation and pole-placement constraints via the linear matrix inequality (LMI) synthesis. The closed-loop robust stability and robust performance are tested through the structured singular value synthesis. Again, the desirable stability and performance are verified by simulations and experimental results.

Table of Contents

List of Tables

List of Figures

Chapter 1: Introduction

MOTIVATIONAL EXAMPLE 1

The past decade has witnessed the fast growth of dc micro-grids, in which power from dc inputs (such as distributed generation [1] sources) is directly delivered to dc loads (such as many newly proposed residential appliances and variable speed drives). Moreover, for special loads such as those in electric ship power systems or datacenters [2-3], it is of particular interest to have a complete dc distribution system that could be easily reconfigurable in case one portion fails. The same feature is desired for dc micro-grids or an utility dc distribution system [4] in order to reduce vulnerabilities for extreme events, such as natural disasters [5].

Electric ships are propelled by electric machines. Nowadays, electric ships are still powered by conventional gas engines and/or gas turbines [2]. The debate on electric ships of the type of motor drive (an induction motor or a synchronous motor) is giving way to the integration of the shipboard power system with the propulsion system and power distribution architecture. To be able to feed critical and heavy shipboard loads on an electric ship, an integrated power and propulsion system with high controllability, reliability, and robustness is desirable [2]. These design goals could be achieved with active distribution nodes [5-6] that act like power routers [5]. Reference [7] proposes an architecture in which loads, generators, and energy storages devices are interfaced by conventional power converters [8]. A study in [5] shows that conventional single-input-single-output (SISO) converters could be expanded into multiple-input-multiple-output (MIMO) converters to realize active distribution nodes. Figure 1.1 exemplifies in a potential application of MIMO converters in the power system of an electric ship, in which active distribution nodes are realized by MIMO converters.

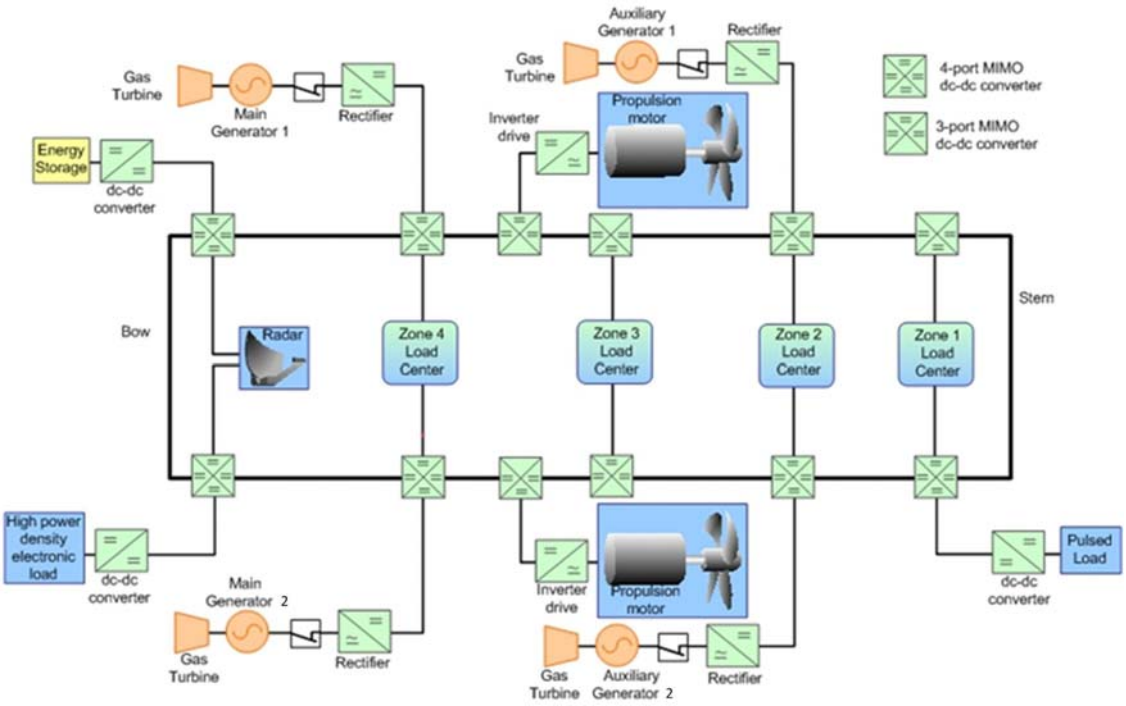

Figure 1.1: Example of a dc Power Distribution Architecture for an Electric Ship Based on MIMO Converters as Active Power Distribution Nodes [5].

MOTIVATIONAL EXAMPLE 2

Overview of Photovoltaic Systems

The previous example shows a potential application of MIMO converters serving as active distribution nodes in a dc distribution system. The next example presents the application of multiple-input converters (MICs) as power electronic interfaces for photovoltaic (PV) systems.

Photovoltaic systems use solar panels to convert incident sunlight to dc electric power. In a conventional grid-connected PV system, an inverter is required to convert the dc output from a PV module string or array to ac power. The single inverter accounts for a significant portion of the cost for the entire system. Besides the high price of the inverter, other issues such as poor reliability and flexibility are also important. Power electronics technologies may allow designers to address these issues.

PV Power System Architectures

1. Centralized Inverter

In a conventional installation of PV modules shown in Fig. 1.2, the PV modules are interconnected in series and/or parallel; then, all PV modules are connected to a single centralized inverter. Main problems of this architecture may be design inflexibility, poor energy harvest, low reliability, and high initial cost.

The overall performance of a PV string (or array) is limited by the module presenting the worst performance, so this centralized architecture is not flexible or scalable because of the difficulty in connecting PV modules with distinct characteristics together (in a string or array). Additionally, PV modules' capability in power generation is not fully exploited and thus, the energy harvest is not optimal. The single inverter may affect the reliability of the entire system because the inverter may become a single point of failure. The centralized inverter leads to expensive initial design in order to address future load increases. Additional issues such as the partial shading condition and uneven dirt collection may further reduce the amount of power generated by the PV modules.

2. Centralized Inverter with Multiple dc-dc Converters

An alternative of the architecture shown in Fig. 1.2 is presented in Fig. 1.3, in which a dc-dc converter is connected to each PV module. Due to the additional stage of dc-dc converters, the interactions among PV modules are reduced because all the PV modules are operating independently. Moreover, this architecture could increase the power generation of a PV system by tracking maximum power point (MPP) for each PV module. However, this configuration still gives rise to high initial costs due to the increased parts-count of the dc-dc converters. In addition, this architecture still has the reliability issue due to the centralized inverter.

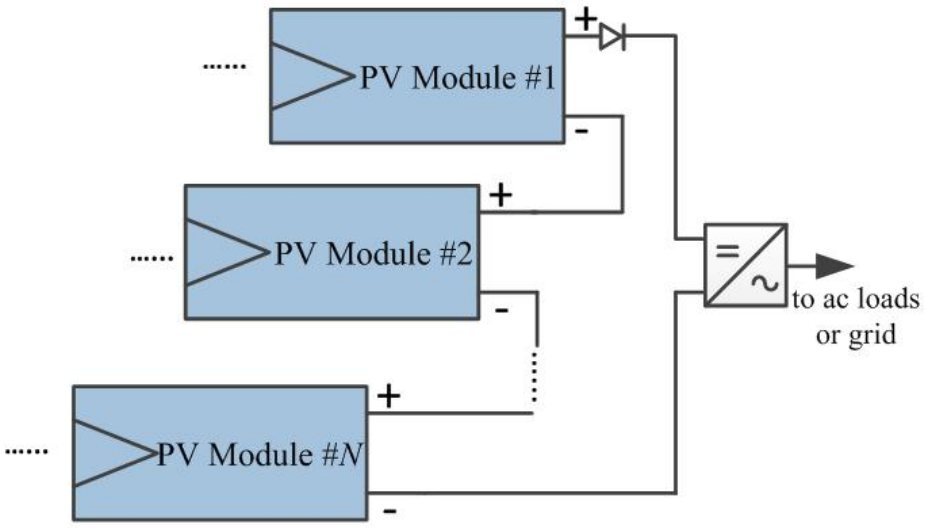

Figure 1.2: A Photovoltaic Generation Architecture with a Centralized Single Inverter.

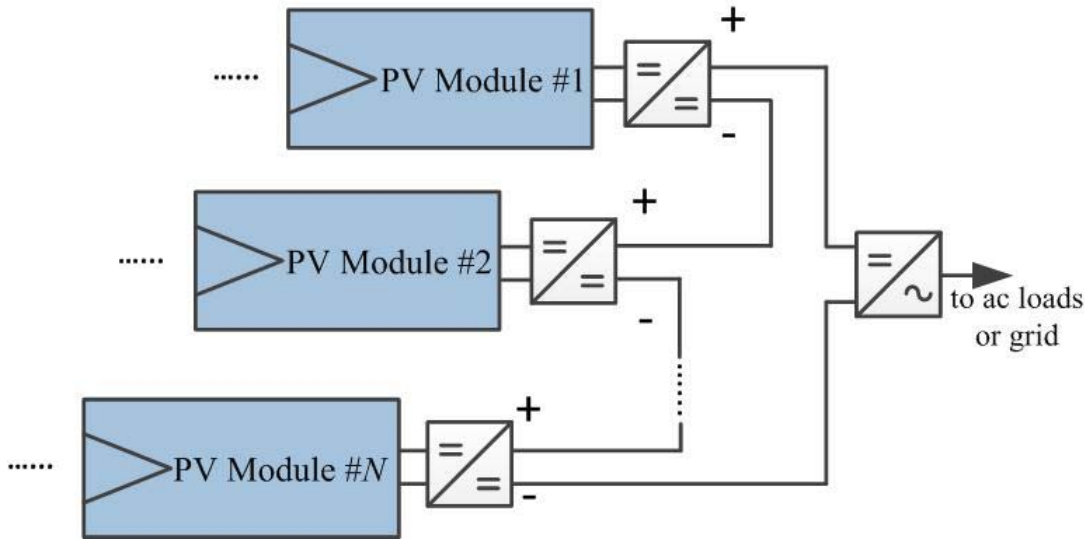

Figure 1.3: A Photovoltaic Generation Architecture with a Centralized Single Inverter and Multiple dc-dc Converters.

3. Centralized Inverter with MICs

Between the aforementioned two extreme alternatives in Figs 1.2 and 1.3, an intermediate solution can be realized through MICs. The input legs of a MIC share a common output stage, which obtains a reduced parts-count. Consequently, the MIC is a cost-effective and highly-available power electronic interface for systems incorporating

multiple power sources. This architecture, shown in Fig. 1.4, is based on modular MICs. Yet, this configuration could still become a single point of failure due to the single inverter.

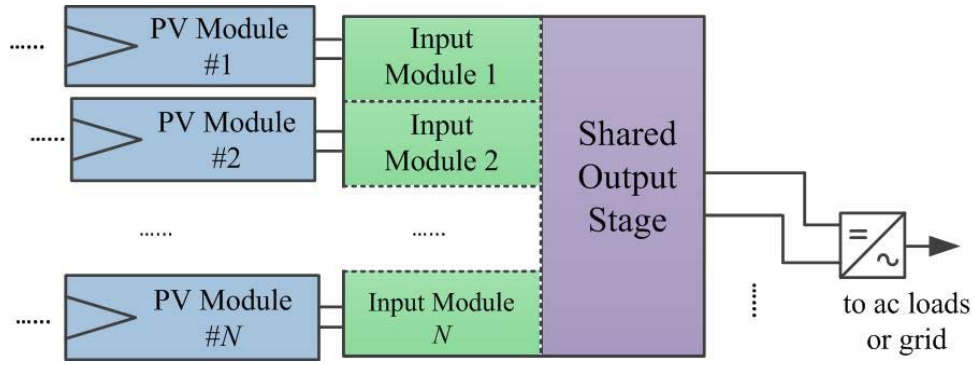

Figure 1.4: A Photovoltaic Generation Architecture with a Centralized Single Inverter and Multiple-Input dc-dc Converters.

4. String Inverters

The string inverter system, in which the PV modules are modularized into several strings [9], represents a more distributed version of the centralized system. In this architecture shown in Fig. 1.5, the output of each string is connected to a distributed inverter. Such a distributed architecture allows for an increased energy harvest and improved reliability of the entire power system.

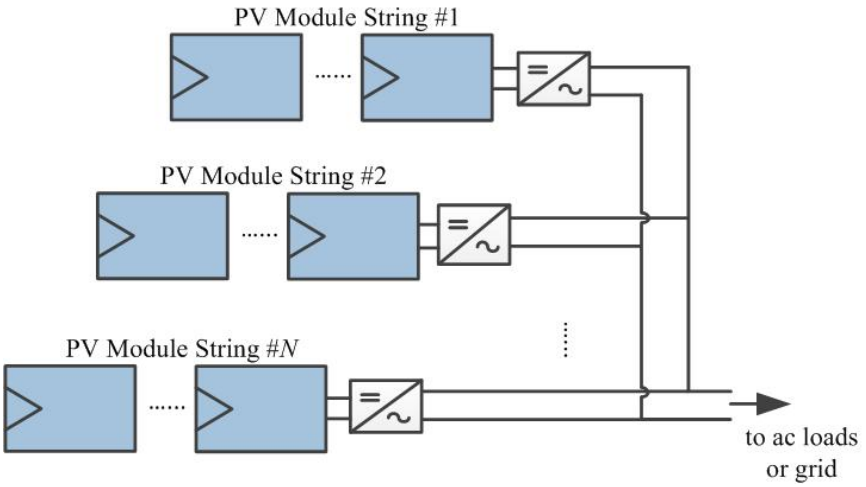

Figure 1.5: A Photovoltaic Generation Architecture with String Inverters.

5. Micro-Inverters

The issues caused by the centralized inverter, such as the lack of flexibility and scalability, low energy harvest, and poor reliability, can be addressed with micro-inverters or module-incorporated inverters [9-11]. In an architecture based on micro-inverters, a PV module incorporates its own power electronic interface. Then, the output of a PV module becomes ac due to the PV module-based inverter. A micro-inverter consists of two stages connected in a cascade fashion. The first stage is configured by a dc-dc converter that both controls a PV string at its MPP and steps up the relatively low input voltage to a higher dc voltage. The second stage is a dc-ac stage that provides a sinusoidal output. The distributed locations of micro-inverters (in each PV module frame) avoid the single point of failure. In addition, this architecture increases power generation through independent control of each PV modules. Therefore, a more flexible, efficient, and reliable system is achieved using this architecture based on micro-inverters. The scheme shown in Fig. 1.6 is also known as the distributed MPP tracking (MPPT) architecture.

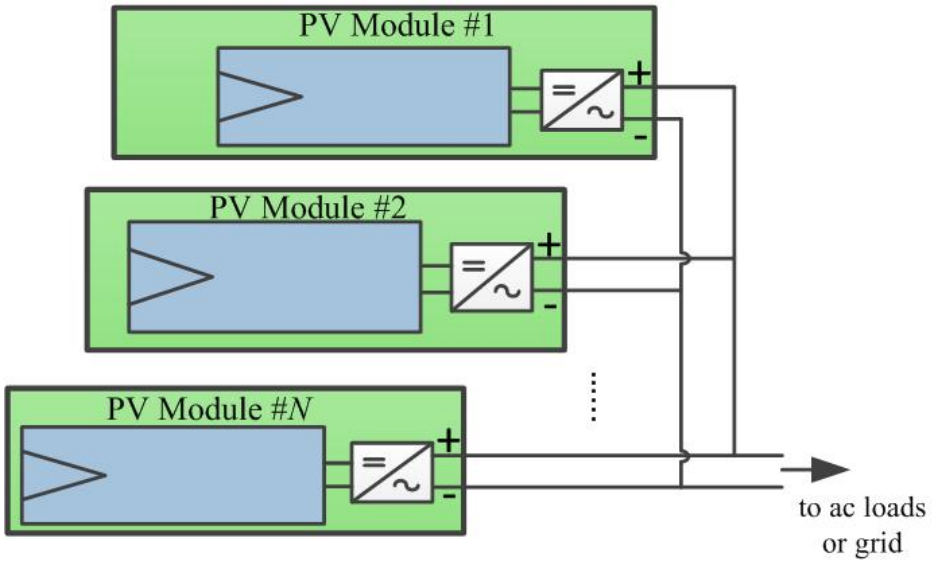

Figure 1.6: A Photovoltaic Generation Architecture with Micro-inverters.

6. Micro-Inverter with MICs

Currently, substantial issues of PV systems are still PV devices' high cost and low power conversion efficiency. Hence, it is desirable to further increase the output power from PV modules. The non-optimal energy harvest could be caused by partial shading or dirt-collection that may impact on only a relatively small part of all the cells in a module. However, due to the interconnection and interaction among PV cells, the power output of the entire module could be significantly reduced. This issue may be addressed by extending the distribution (or modularity) further into the PV module level. For example, a 72-cell PV module could be divided into four strings of 18 cells each. The configuration is described through Fig. 1.6. The first stage of a micro-inverter is configured with an MIC instead of a conventional dc-dc converter. Strings of PV cells are connected to the input modules of a front-to-end MIC. The power generation is maximized through the minimization of PV module mismatch. A previous study in [12] presents the enhanced energy harvest of a PV module under partial shading conditions through a multiple-input boost converter.

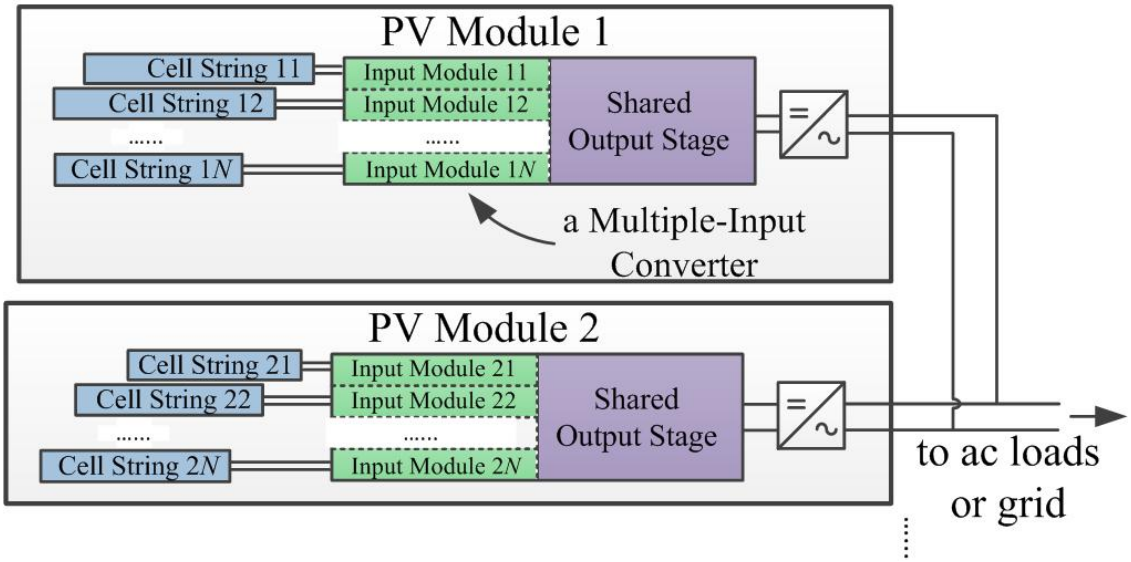

Figure 1.7: A Photovoltaic Generation Architecture with Micro-inverters and Multiple-Input Converters.

In summary, as an enabling technology, power electronics allow for the conversion of the dc power generated by PV modules. Recent technologies, such as the micro-inverter and the multiple-input power converter, further increase the energy capture of PV generation systems while achieving enhanced reliability.

THE HYBRID DC-DC CONVERSION SYSTEM BASED ON MULTIPORT CONVERTERS

Overview

Previous examples show the potential applications of multiport converters, including both MIMO converters and multiple-input converters, in the power system of an electric ship and a renewable energy application. Allowing bidirectional power flow among input legs, MIMO converters are the expansions of MICs [5, 13]. In the past decade, many multiple-input topologies have been proposed [5, 14-48]. Components are saved due to a common output stage shared by multiple input legs. Desirable characteristics, such as cost-effectiveness, high availability and reliability are found in MIC-based systems. In addition to the merits inherited from MICs, MIMO converters allow bidirectional power flow in each port. As an example, two possible MIMO converters, the MIMO boost-and-buck converter and the MIMO fly-back converter, are identified in [5]. Since the main focus of this dissertation is on several other key issues instead of the bidirectional power flow, unless specified, the MIC and the MIMO converter are not strictly differentiated throughout this dissertation.

Time-multiplexing MICs and an MI-SEPIC

A very first question on the MIC would be how to construct its topology. More specifically, the question becomes how to insert one or more input legs into a single-input dc-dc converter so that a common output can be shared. Reference [41] summarized a systematic way of generating MIC topologies, by excluding trivial topologies based on a multi-winding transformer [19]. One type of MIC topologies takes advantage of a time-multiplexing (TM) switching control (such as one illustrated in Fig. 1.8) to further

increases the parts-count saving [14, 20, 34]. The TM scheme is also excluded in [41], due to a seemingly limitation on simultaneous energy transfer. However, such as limitation of TM-MICs may not hold in general. For instance, a multiple-input (MI) Single-Ended-Primary-Inductor-Converter (SEPIC) topology shown in Fig. 1.9 can achieve simultaneous energy transfer for all the inputs. The MI-SEPIC shown in Fig. 1.9, which presents desirable flexibility for distributed generation (DG) applications, was initially proposed in [34] and studied in [35]. The MI-SEPIC allows for stepping up or down its input voltages. Its current interface may achieve a non-switched input current, which is necessary for the proper operation of sources like fuel cells [49]. The intrinsic modular design makes the MI-SEPIC flexible, scalable, and reliable. Time-multiplexing operation enables independent control of each source. Due to these characteristics, the MI-SEPIC is identified to be one of the most suitable MIC topologies for dc micro-grid applications. However, an important limitation of the MI-SEPIC is its low efficiency, which is in the range of high 80 % as indicated in [35].

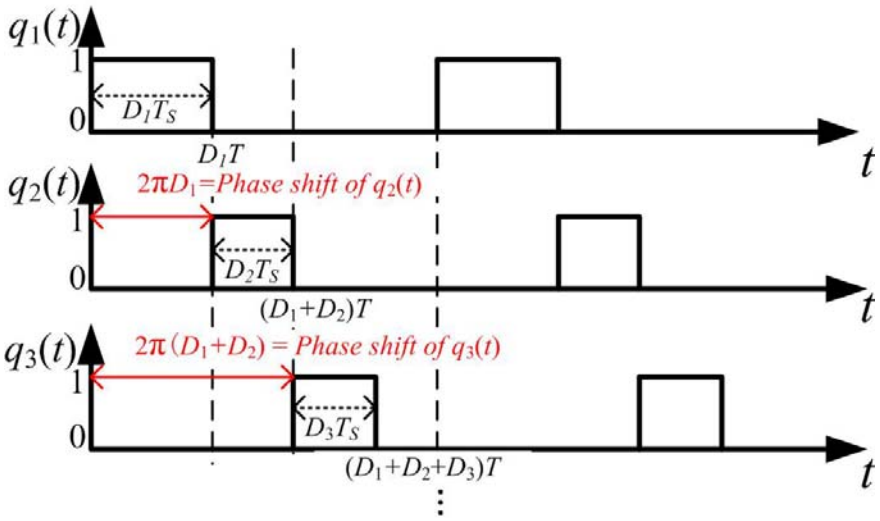

Figure 1.8: Effective Switching Functions of a TM-MIC.

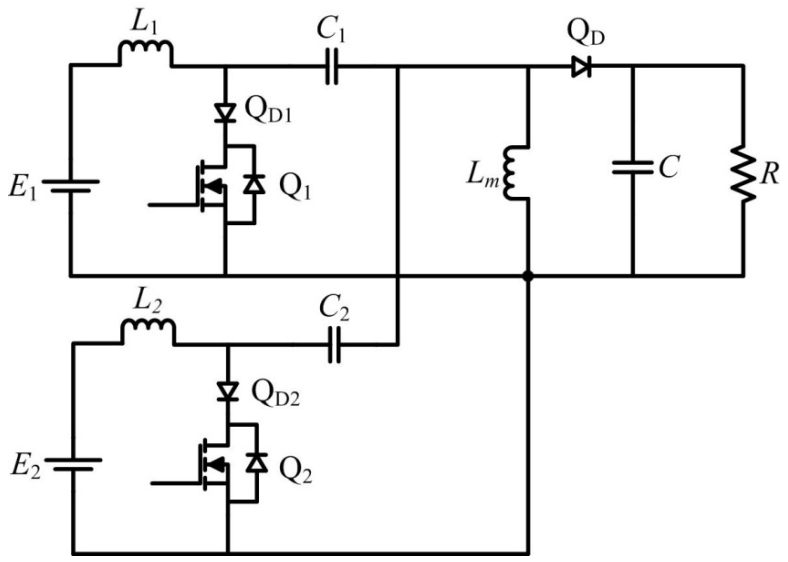

Figure 1.9: An MI-SEPIC Topology with Dual Inputs [34, 50].

Existing Issues of MICs and Proposed Solutions

In the past decade, work on MICs mainly focuses on proposing topologies with distinct characteristics [5, 19, 23, 29, 34, 40-41, 44]. Issues of MICs, particularly for those involved in renewable energy generation have not been adequately addressed in the system design.

Relatively Low Efficiency

One of these issues is low efficiency. Most previous work on MICs fails to address the problem of power conversion efficiency which in many cases remained below 90 % [19, 27, 29, 51]. Only a limited amount of work focuses MICs efficiency optimization. Two exceptions are found in [52] and [44]. Reference [44] takes advantage of an auxiliary circuit to achieve zero-voltage switching (ZVS) and thus high efficiency. Reference [52] similarly applies an auxiliary circuit to achieve ZVS, thereby improving the efficiency of an isolated MI-SEPIC (IMI-SEPIC). However, the auxiliary circuit may compromise the low parts-count advantage of MICs and introduce additional conduction loss.

Maximized parts-count saving favors TM-MICs which generally require forward-conducting-bidirectional-blocking (FCBB) switches [34]. The FCBB switch, however, introduces high power loss and leads to low efficiency of TM-MICs. For example, relatively low efficiency is observed in the MI-SEPIC and other TM-MICs with FCBB switches [20, 35, 53]. The power loss in an MI-SEPIC is analyzed in Chapter 2. Then, an efficiency improvement design through a novel switching control of an MI-SEPIC is presented. The high efficiency of an MI-SEPIC is verified through a prototype-based test.

Modeling of Time-multiplexing Multiple-input Converters

Generally speaking, a TM-MIC is an MIC involving TM switching functions—i.e., only one switch conducts current at a given instant—which may lead to effective switching functions as indicated in [34]. Therefore, in a TM switching control scheme, interactions exist among switching functions. Such interactions can be represented by the time delays (or phase shifts) among the switching functions shown in Fig. 1.8. Furthermore, TM-MICs are subject to a system-level coupling: the time derivatives of state variables of an input leg are dependent on the state variables from other input legs (a topological coupling) and on other legs effective switching functions (a control coupling).

The state-space averaging (SSA) has been adopted as a standard tool for analysis and modeling for pulse-width modulation (PWM) converters. With a small ripple assumption, the SSA considers that the periodic state variable's dc component dominates its ac components so high order harmonics are neglected. For a conventional single-input converter (SIC) operating in continuous conduction mode (CCM), the SSA usually achieves a satisfactory modeling accuracy. On the other hand, the SSA has been mechanically applied to MIC modeling in a number of cases, such as [54] and [23], yet, it has never been formally extended for application in MICs. In fact, an MIC formed by series/parallel combinations of SICs has been decomposed into several SICs so the analysis of such an MIC could be performed according to conventional methods which are

feasible for SICs. This dissertation shows, however, considerable discrepancy is found between the behaviors of a TM-MIC switched model and its SSA model even under small-ripple condition. In the derivation of an SSA model, time-dependent switching functions are simplified into numerical duty ratios so phase-shift information depicted in Fig. 1.8 is lost. Hence, the SSA method may be inadequate in order to model TM switching functions. On the other hand, TM-MICs are subject to more complicated interactions among state variables in their full harmonic representation, due to coupling and TM switching functions. Consequently, TM-MICs are more sensitive to higher order harmonics (or waveform ripple) than SICs. Thus, neglecting high-order harmonics, the SSA may cause substantial modeling errors for TM-MICs. In summary, given switching function representation over simplification and high order harmonics truncation, SSA may not be an effective approach for the modeling of TM-MICs.

This dissertation presents a more accurate model for TM-MICs based on a multi-frequency (MF) approach. Derived based on the switched dynamic equations, the SSA model only considers the topological coupling but fails to represent the time-dependence of switching functions (interactions). The MF approach is also derived from the switched dynamic equations but, contrary to the SSA, it is also able to represent the time-dependence of switching functions by considering their phase shifts among switching functions. The MF modeling approach significantly improves the modeling accuracy of TM-MICs comparing to the SSA. The MF model of an TM-MIC also allows for performing power budgeting numerically, thus it avoids the complicated analytical analysis in [24].

Control of Multiport Converters in a dc Distribution System

In the control of multiport converters (including both MICs and MIMO converters), two main problems need to be addressed: how to perform a controller design

that could address control limitations of multiport converters and how to evaluate the stability of the entire system including sources and loads.

Formal analysis of multiport converters' control characteristics and strategies can be challenging. Firstly, from a control perspective, an multiport converter is a multivariable system [55-57] rather than a combination of independent SISO systems, as it is typically considered in previous studies [18, 23, 39, 48, 58]. Generally, in a multivariable system, all the output variables are affected by all the input variables and vice versa. In a multivariable plant, control limitations caused by right-half-plane (RHP) zeros and disturbances become less prominent compared with those in a conventional single-input-single-output (SISO) system. Nevertheless, the control limitation caused by model uncertainties is worth more attention in a multivariable control system due to the directionality [56]. Secondly, multiport converters are typically used in DG applications where renewable energy sources' varying operating point may introduce significant control disturbances. Such disturbances further cause uncertainties of the operating variables (e.g., varying duty ratios and the operating point) of multiport converters. Therefore, given the sensitivity of multiport converters and the potentially complicated disturbances/uncertainties of DG systems, it is desired to find a general framework of controller design and synthesis, which is able to resolve issues found when using multiport converters in DG applications.

On the other hand, to validate a controller design of a multiport converter, an efficient and accurate model of the renewable energy source is necessary. Reference [59] shows that the internal impedance of a PV module significantly affects its dynamic behavior over the entire operation region. However, in many previous studies, PV modules are treated as ideal voltage sources and the nonlinear and time-varying factors are completely neglected [35]. Potential instability or limitation in closed-loop performance may not be predicted without considering the worst operation caused by the varying internal impedance. Therefore, previous work that uses methods more

appropriate for SISO systems and defective model of a renewable energy source may not adequately address the modeling and control problems.

In this work, two control schemes, the decentralized control and the multivariable control, are studied for multiport converters. A decentralized is studied in Chapter 4 to achieve the simplest control scheme. Furthermore, in Chapter 5, a robust multivariable controller is studied to guarantee stability and performance specifications under uncertainties.

Chapter 2: A Multiple-Input SEPIC and Its Efficiency Improvement

This chapter explores an MI-SEPIC topology. The basic operation of an MI-SEPIC under time-multiplexing switching control is discussed. The desired characteristics of the MI-SEPIC when applied to distributed generation applications are commented. Extended topologies based on the MI-SEPIC, which lead to further flexibility for different applications, are reviewed and summarized. At the end of this chapter, a novel approach to improve the efficiency of an MI-SEPIC efficiency is revealed. Two key design modifications enhance the efficiency of the MI-SEPIC without comprising its cost-effectiveness.

INTRODUCTION OF THE MI-SEPIC

Non-Isolated Version

Figure 1.9 shows an MI-SEPIC topology with dual inputs. The input leg #1 is formed by an inductor (L_1), a FCBB switch—which is herein made of a MOSFET (Q_1) and a reverse current-blocking diode (Q_{D1})—and a center capacitor (C_1). The same configuration is found in input leg #2. The common output stage is formed by an output diode (Q_D), an output inductor (L), and an output capacitor (C). Consider a dual-input SEPIC in Fig. 1.9 driven by the switching control in Fig. 2.1. The dynamic equations are

$$\begin{cases} L_1 \dfrac{di_{L1}}{dt} = E_1 - q_{2,eff}(v_{C1} - v_{C2}) - q_D(v_{C1} + v_C) \\ L_2 \dfrac{di_{L2}}{dt} = E_2 - q_1(v_{C2} - v_{C1}) - q_D(v_{C2} + v_C) \\ L \dfrac{di_L}{dt} = q_1 v_{C1} + q_{2,eff} v_{C2} - q_D v_C \\ C_1 \dfrac{dv_{C1}}{dt} = -q_1(i_L + i_{L2}) + (q_{2,eff} + q_D) i_{L1} \\ C_2 \dfrac{dv_{C2}}{dt} = (q_1 + q_D) i_{L2} - q_{2,eff}(i_{L1} + i_L) \\ C \dfrac{dv_C}{dt} = q_D(i_{L1} + i_{L2} + i_L) - \dfrac{v_C}{R} \end{cases} \tag{2.1}$$

where $q_{2,eff} = q_2 - q_1$; q_1 and $q_{2,eff}$ are the effective time-dependent switching functions of the input leg #1 and #2, respectively, as indicated in Fig. 2.1. Another switching function q_D is defined as $1-q_1-q_{2,eff}$, which can be viewed as the switching function of the output diode. Coupling between inputs are observed in these MI-SEPIC switched dynamic equations. For example, the voltage across inductor L_1 in input leg #1 depends on v_{C2} and the effective duty cycle $q_{2,eff}$ from input leg #2.

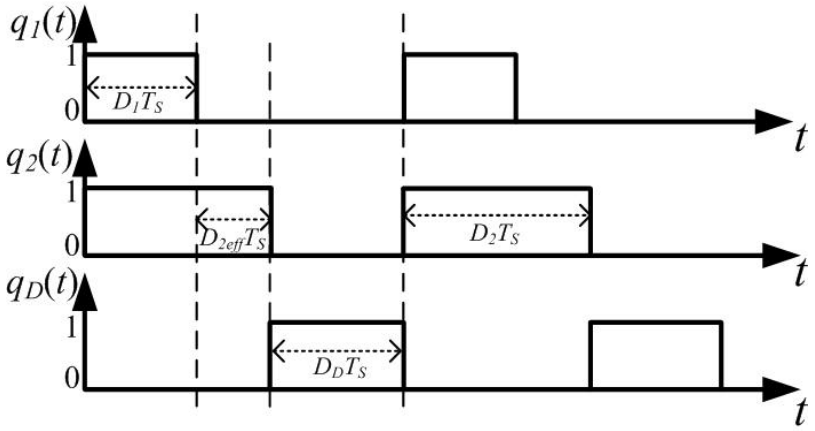

Figure 2.1: Switching Control Strategy 1.

The operation of the MI-SEPIC was studied in [35] through the topology in Fig. 1.9 and the switching control strategy shown in Fig. 2.1. As shown in Fig. 2.1, the MI-SEPIC is driven by a time-multiplexing fashion which implies that only one switch conducts current at a time. Readers are referred to [35] and [34] for more details of the topology and operation of the MI-SEPIC.

A Comparison with MI-boosts and MI-Ćuk Converters

It may be argued that, the MI-SEPIC in Fig. 1.9 may not provide significant cost benefits because an FCBB leg usually requires one more switch. However, it should be emphasized that more other components that are among the costliest components in the circuit—an inductor, a switch, a capacitor—are shared at the output. Furthermore, it provides more flexibility with hybrid generation topologies. In particular, the choice of

MI-SEPIC instead of an MI-boost converter [23] (Fig. 2.2) can be justified based on voltage integration, input-to-output voltage ratios, and isolation needs. In a MI-boost converter, input voltages must be lower than its common output voltage. However, according to [60], a wide input voltage range is generally required for solar applications, which restricts MI-boost's applications. Voltage boosting only characteristic also limits MPP tracking implementation because the MPP cannot be reached for load resistances lower than the ratio of the PV module's output voltage and current at its MPP. The proposed MI-SEPIC is not subject to such restrictions, so it is able to operate even with significantly distinct input voltages. Another important issue in the MI-boost is that its step-up ratio is limited. On the contrary, in the MI-SEPIC, both voltage step up and step down can be significantly extended by simply replacing the output inductor by a pair of coupled inductors. The addition of the couple inductors for the MI-SEPIC also provides input-output isolation, whereas MI-boost converters cannot provide such feature. Thus, a boost topology was discarded early in the analysis process because it was clear that despite some potential virtues of a boost circuit, it was impossible to meet our design goals, e.g. for PV systems, with such boost topology. A seemingly similar choice to the SEPIC presented here is the MI-Ćuk (see Fig. 2.3) converter proposed in [60]. Note that the FCBB legs in the MI-SEPIC in Fig. 2.12 (a) are configured by a series connection of two MOSFETs, instead of a MOSFET and a diode in Fig. 1.9. Different FCBB configurations will be discussed later in this chapter. An obvious issue with a MI-Ćuk is that it has a negative output voltage. Another issue with a Ćuk converter or an MI-Ćuk converter is found when attempting isolation. An isolated MI-Ćuk requires one more capacitor and one more inductor than the isolated multiple-input (IMI) SEPIC, as shown in Fig. 2.4. Hence, while there are no significant advantages in selecting a Ćuk topology over a SEPIC, the former adds some disadvantages when compared with the latter.

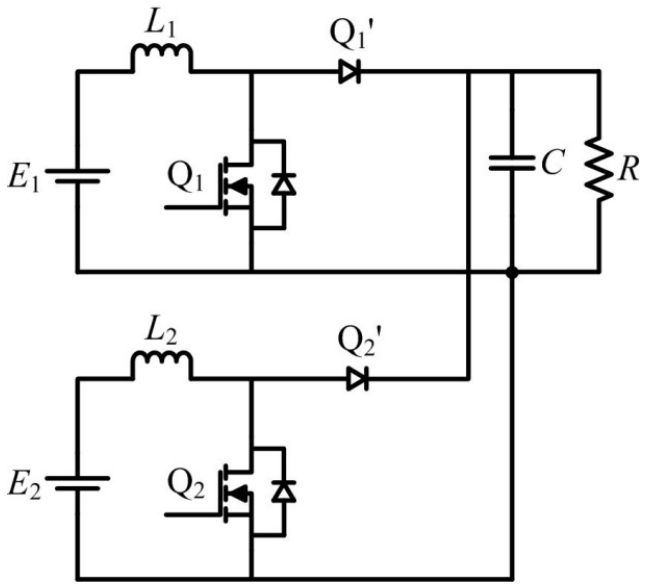

Figure 2.2: An MI-Boost Converter.

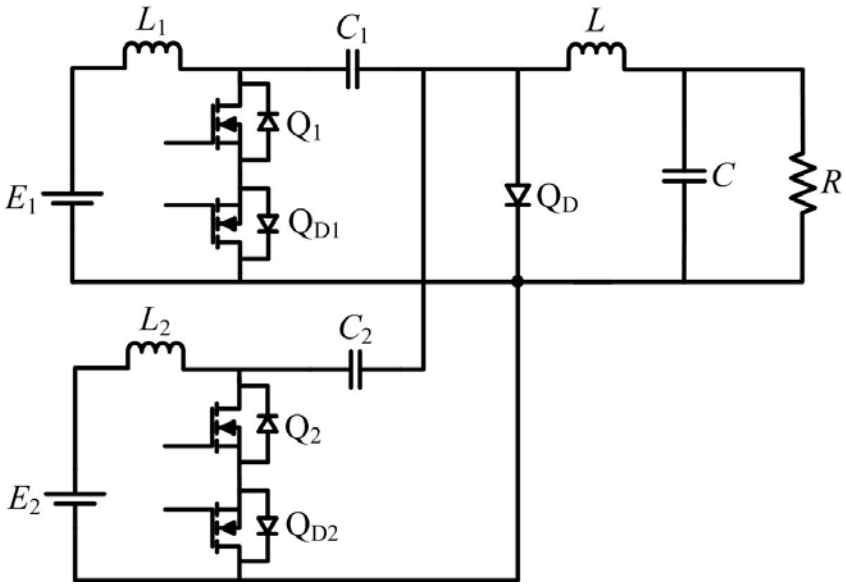

Figure 2.3: An MI-Ćuk Converter.

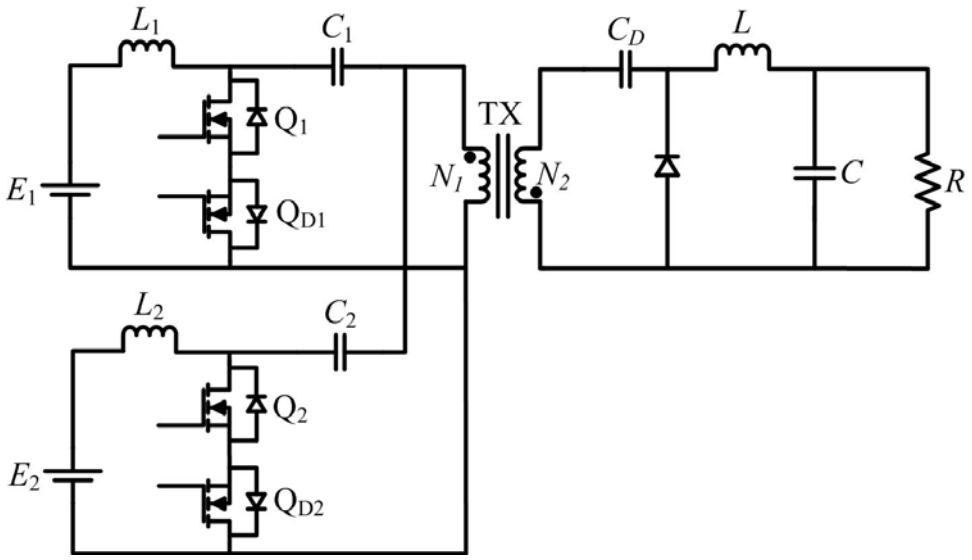

Figure 2.4: An Isolated MI-Ćuk Converter.

Isolated Version

The topology of an IMI-SEPIC is shown in Fig. 2.5. The advantage of adding isolation to MI converters is to reduce the duty cycle limitations of time-multiplexing MICs. According to the analysis in [50], the following conditions of the duty ratios can be derived

$$D_{1,i}^{*} = \frac{rD_1^{*}}{1+(r-1)(D_1^{*}+D_2^{*})} \quad , \quad D_{2,i}^{*} = \frac{rD_2^{*}}{1+(r-1)(D_1^{*}+D_2^{*})} \tag{2.2}$$

where $D_{1,i}^{*}$ and $D_{2,i}^{*}$ are the duty ratios of the IMI-SEPIC at the MPP, and D_1^{*} and D_2^{*} are the duty cycles of the non-isolated MI-SEPIC at the same MPP.

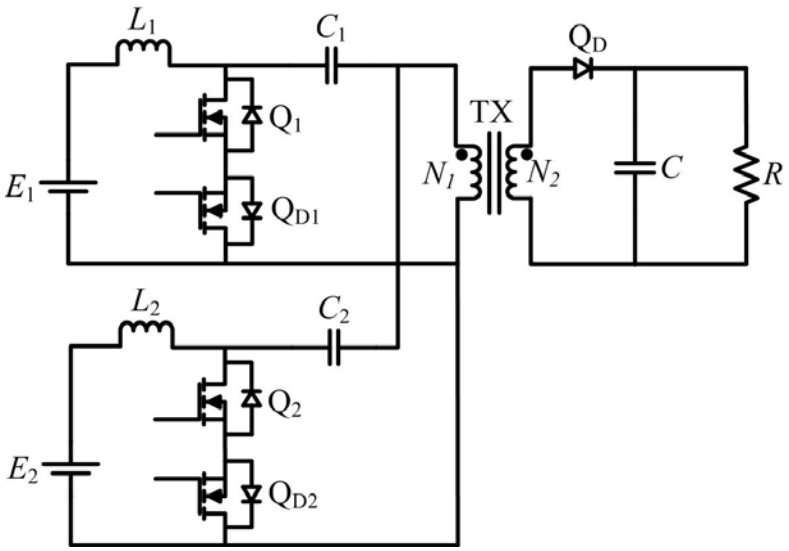

Figure 2.5: An Isolated MI-SEPIC Topology.

As indicated in [50], an n-input IMI-SEPIC, the k-th duty ratio (k = 1, 2, 3… n) is given by

$$D_{k,i}^{*} = \frac{rD_k^{*}}{1+(r-1)\sum_{k=1}^{n} D_k^{*}}. \tag{2.3}$$

It is straightforward to show that $N_2 > N_1$ leads to $D_{k,i}^{*} < D_k^{*}$. Hence, an $r > 1$ allows for reducing the duty ratios of an IMI-SEPIC under the same operational condition of an MI-SEPIC. For completeness, MPP tracking was inspected with a simulation. Its results in Fig. 2.6 show that MPPs tracking of the previous example with a three-input IMI-SEPIC and with r = 1/4. The simulation also considers the PV module described in [61] and adopts ripple correlation control (RCC) detailed in [51] and [62]. It demonstrates that the IMI-SEPIC is able to track the MPP both, initially, when the incident solar power level is 1000W/m^2 and, after 0.10s, when the PV modules are subject to a sudden insolation drop. Since MPP is provided here as a relevant practical example but it is out of the scope of this dissertation as its main focus, readers can gain insight of MPP tracking implementation and stability issue through [51], [63], and [64].

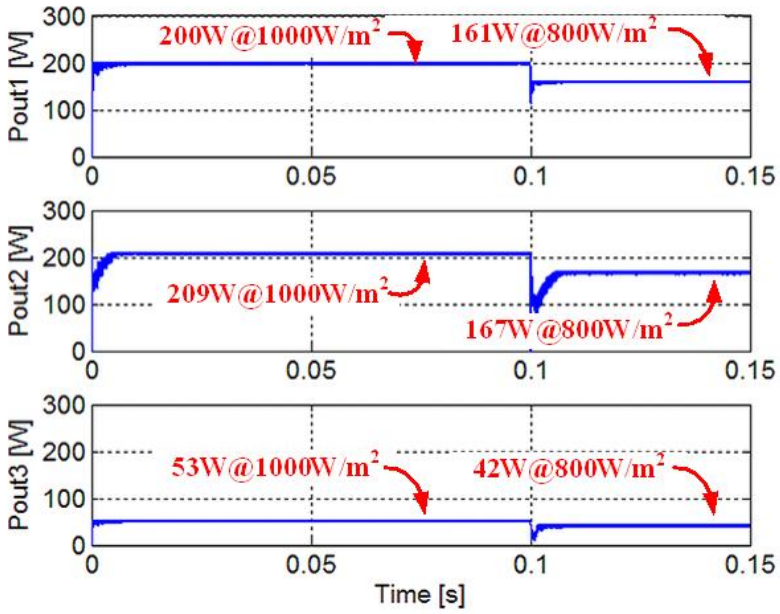

Figure 2.6: Simulated Simultaneous MPPs Tracking by a Three-input IMI-SEPIC.

Circuit Topology Variations

One of the features of the MI-SEPIC's is its simple way of incorporating practical topology variations that improve efficiency, flexibility, and reliability. This next discussion explores these possible variations.

Switch Realization

Four possible combinations listed in Fig. 2.7 allow realizing the FCBB switches in time-multiplexing MICs. Two options left out here would be an insulated-gate bipolar transistor (IGBT) and a gate turn-off thyristor (GTO), which are beneficial choices when delivering a high current because of its lower power dissipation [65]. Since in here the MI-SEPIC is considered as a solution for low power applications, only F1 to F4 shown in Fig. 2.7 are considered in this dissertation.

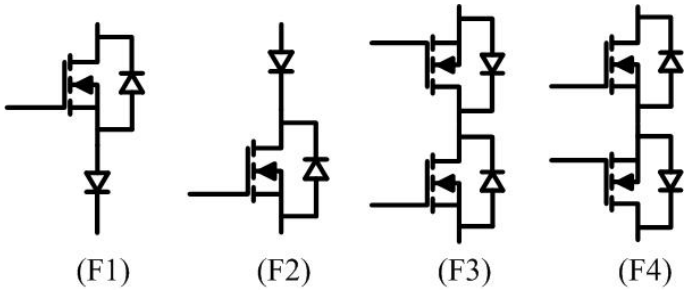

Figure 2.7: Four Possible Realizations of FCBB switches with MOSFETs and/or Diodes.

Isolated Version with an Active Clamping Circuit [66]

As aforementioned, the MI-SEPIC can be conveniently extended to its isolated version as described in Fig. 2.5, to achieve an extended voltage transfer ratio. However, a subsequent issue of isolation is the additional loss and high voltage stress caused by the coupled inductor leakage inductance L_r, because the energy stored in L_r remains on the primary side while the energy stored in the magnetizing inductor L_m is transferred to the secondary side. When FCBB switches are off, the energy stored in L_r is transferred to the parasitic capacitors of the primary switches. The energy stored in parasitic capacitors eventually dissipates as additional switching losses in the main switches during turn-on transients. Reference [66] addresses this issue through a compact active clamping leg (see Fig. 2.8) adopted from [67]. One of the advantages of the solution in [66] is that only one active clamping leg is needed for all input legs regardless of the number of inputs. This solution reaches an optimal efficiency of 94 % at 200 W [66].

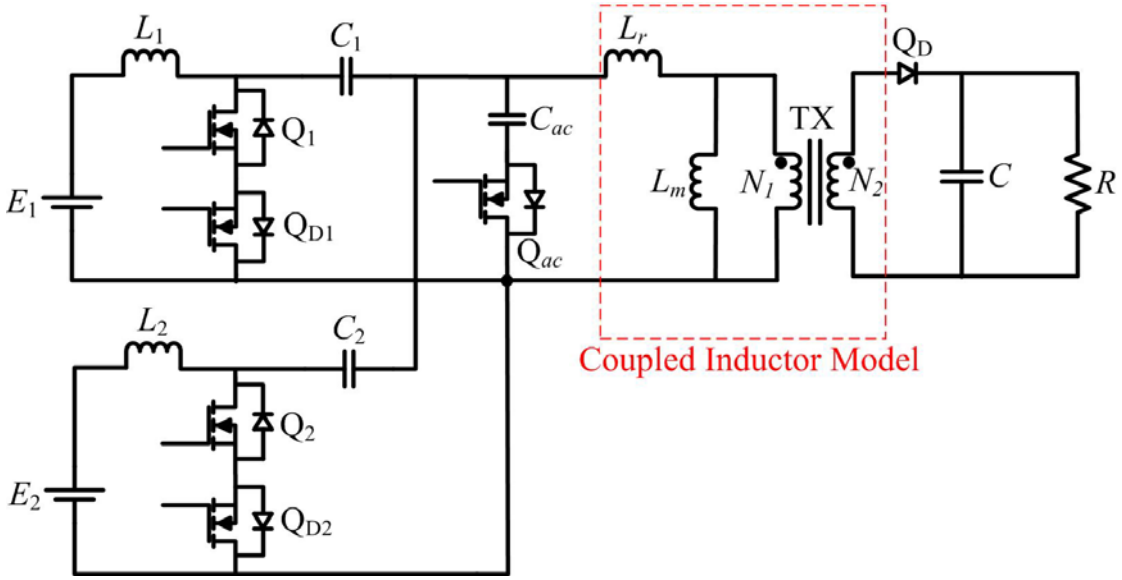

Figure 2.8: Isolated Dual-input SEPIC with Active Clamping Circuit [52].

Reliability Improvement [68]

In most converters, bulk electrolytic capacitors are used to filter the voltage interface ripple. However, these capacitors are among the most unreliable components in power electronic converters. According to [68], coupled-filter configuration [69] previously explored for single-input converters can also be applied to an IMI-SEPIC to reduce the capacitance of C and voltage ripple of v_C, as shown in Fig. 2.9. The relationships of the currents in the coupled-filter are

$$i_s = i_{DC} + i_{AC} = i_d + i_a \tag{2.4}$$

$$i_{AC} = \left(-n_c + 1\right) i_a \tag{2.5}$$

Note that i_{DC} and i_{AC} are the dc and ac components of i_s; $n_c = N_{AC} : N_{DC}$, denotes the turns ratio of coupled inductor TX. If n_c is much smaller than 1, the ac harmonics in i_{DC} are considerably reduced because almost all ripple current components flow through the ac port. Hence, zero-ripple current on the output port is achieved. As a result, a large capacitance C is not necessary anymore and other more reliable capacitor technologies can be used to replace electrolytic capacitors.

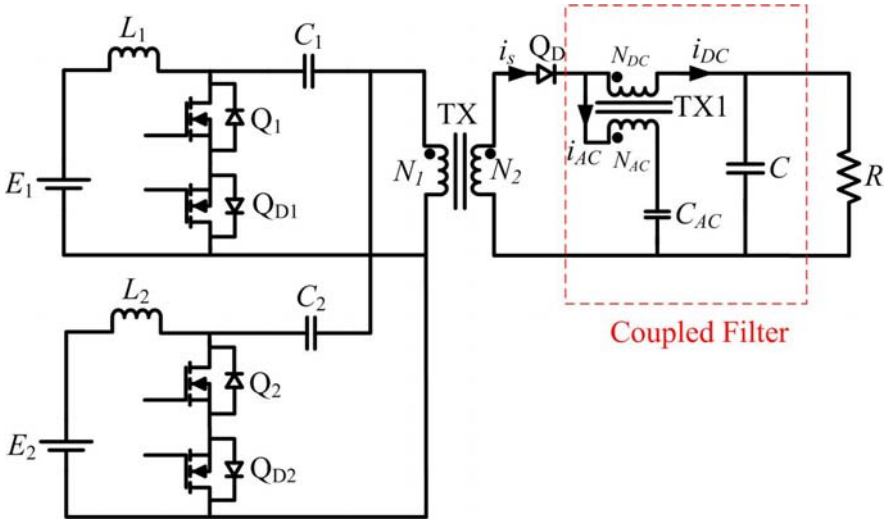

Figure 2.9: Isolated Dual-input SEPIC with a Coupled Filter [68].

Bi-directional Power Flow [70]

The input stage of the MI-SEPIC topology can be expanded to provide bi-directional power flow capability for energy storage devices [70], as shown in Fig. 2.10. In charging mode, the coupled-inductor TX_{in} is energized by the source of the other input leg and the currents flowing through Q_{Din1} and L_2 are both negative. Thus, reversed power flow can be achieved.

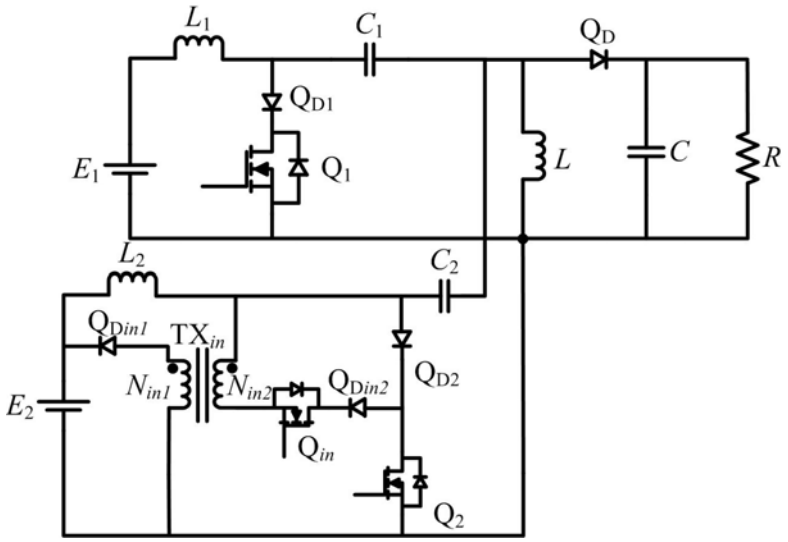

Figure 2.10: Dual-input SEPIC with a Bi-directional Input Leg [70].

EFFICIENCY IMPROVEMENT OF A NON-ISOLATED MI-SEPIC

High Power Loss Introduced by FCBB switches

The efficiency of the MI-SEPIC in Fig. 1.9 was found to be around 85 % up to about 100 W as indicated in [50]; the output power was not further increased in [50] because the power loss went up quickly when the output power exceeded 100 W. It was found in experimentation that MOSFETs Q_1 and Q_2 shown in Fig. 1.9 were the hottest components, whose temperatures were about 70 degree Celsius under a 25 degree Celsius ambient temperature. Considering the output power was still relatively low (below 100 W), such a temperature was already high.

The power loss is mainly caused by turn-on switching of MOSFETs Q_1 and Q_2. Generally in a hard-switched dc-dc converter, the power loss incurred in turn-off transients of MOSFETs is negligible; substantial energy loss incurs when MOSFETs turns on [8]. A snapshot in Fig. 2.11 (a) shows the voltages and the currents of the FCBB switches in an MI-SEPIC which is configured through Fig. 1.9 and driven through Fig. 2.1. Snapshots in Fig. 2.11 (b-c) reveal that, energy is stored in the output capacitance of the MOSFETs during turn-off transients. Due to the blocking function of the diode, the stored energy can only be dissipated in the on-resistances (R_{DS_ON}) of MOSFETs during the next turn-on transients. Therefore, the MOSFETs in the MI-SEPIC in Fig. 1.9 driven by switching functions in Fig. 2.1 are subject to substantial turn-on loss. Snapshots shown in Fig. 2.11 (b) and (c) verify the observation of MOSFETs' high temperature in experiments.

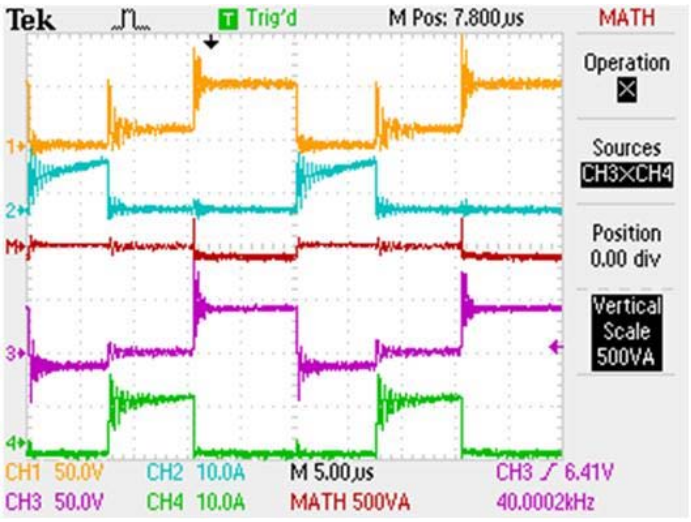
Tek
Trig'd
M Pos: 7.800µs
MATH
Operation
Sources
CH3×CH4
Position
0.00 div
Vertical
Scale
500VA
CH1 50.0V
CH2 10.0A
M 5.00µs
CH3 ⁄ 6.41V
CH3 50.0V
CH4 10.0A
MATH 500VA
40.0002kHz

(a)

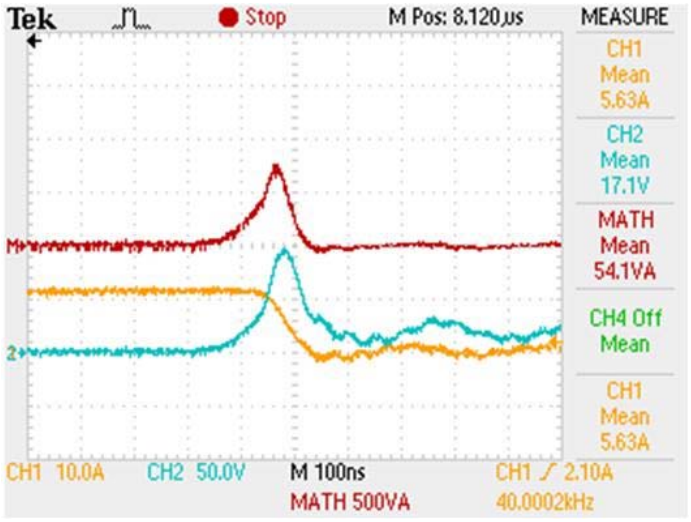
Tek
Stop
M Pos: 8.120µs
MEASURE
CH1
Mean
5.63A
CH2
Mean
17.1V
MATH
Mean
54.1VA
CH4 Off
Mean
CH1
Mean
5.63A
CH1 10.0A
CH2 50.0V
M 100ns
CH1 ⁄ 2.10A
MATH 500VA
40.0002kHz

(b)

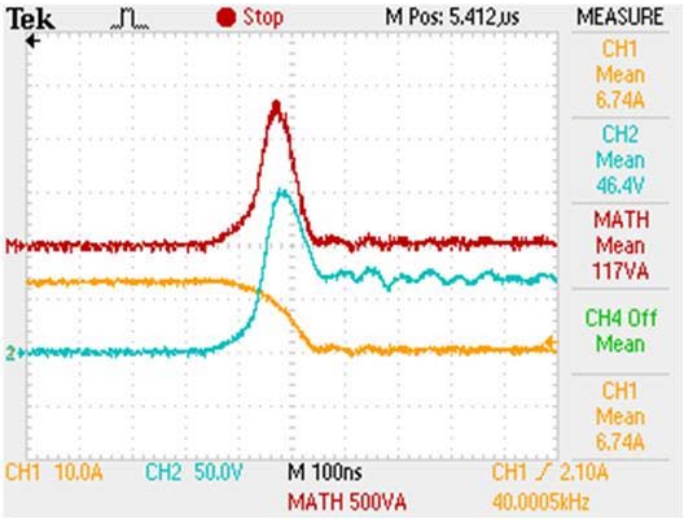

(c)

Figure 2.11: Turn-off Transients of the FCBB switches in the MI-SEPIC in Fig. 1.9. (a) CH1=v_{FCBB1}, CH2=i_{FCBB1}, CH3=v_{FCBB2}, CH4=i_{FCBB2}. (b) CH1=i_{FCBB1}, CH2=v_{FCBB1}, MATH=CH1 × CH2. (c) CH1=i_{FCBB2}, CH2=v_{FCBB2}, MATH=CH1×CH2.

A Modified Version of the MI-SEPIC

Snapshots in Fig. 2.11 (b) and (c) reveal that switch F2 (see Fig. 2.7) may introduce high turn-on loss. This issue can be addressed by modifying the topology and switching control strategy of the MI-SEPIC.

Four configurations shown in Fig. 2.7 are four possible realizations of FCBB switches. In an MI-SEPIC, switch F2 shows grounding ease compared to switch F1 since the MOSFETs in the input legs share a common ground. In addition, switch F4 may be more advantageous than switch F3 since MOSFETs from the same input leg share a common ground. Configurations F3 and F4 can also be viewed as the synchronous rectification version of switches F2 and F1, respectively. All the realizations of FCBB switches shown in Fig. 2.7 could be successfully used in an MI-SEPIC with proper switching strategies.

Figure 2.12 (a) shows a modified MI-SEPIC converter with FCBB legs having configuration F4. Unless specified in this chapter, the parameters of the configuration shown in Fig. 2.12 (a) are given in Table 1.

Parameter	Value	Unit
L_1, L_2, L	320	μH
C_1, C_2	34	μF
C	1200	μF
E_1	40.0	V
E_2	45.0	V
f	50	kHz

Table 1: Parameters of an MI-SEPIC.

High efficiency cannot be achieved without a sophisticated driving strategy. Figure 2.12 (b) shows the proposed switching control strategy allowing for high efficiency. Note that this efficiency-improvement scheme (Fig. 2.12) works without an extra auxiliary circuit. Let FCBB switch i represent the i-th FCBB switch in leg #i (i = 1, 2). Assume that, the input voltage of sources are all close in magnitude, that is, in the MI-SEPIC shown in Fig. 2.12, I have $E_1 \approx E_2$. Moreover, to motivate the analysis, consider that $E_1 < E_2$ and define their voltage difference by $\Delta E = E_2 - E_1$. In summary, the assumptions can be expressed by the following equation

$$0 < \Delta E << E_1 < E_2. \tag{2.6}$$

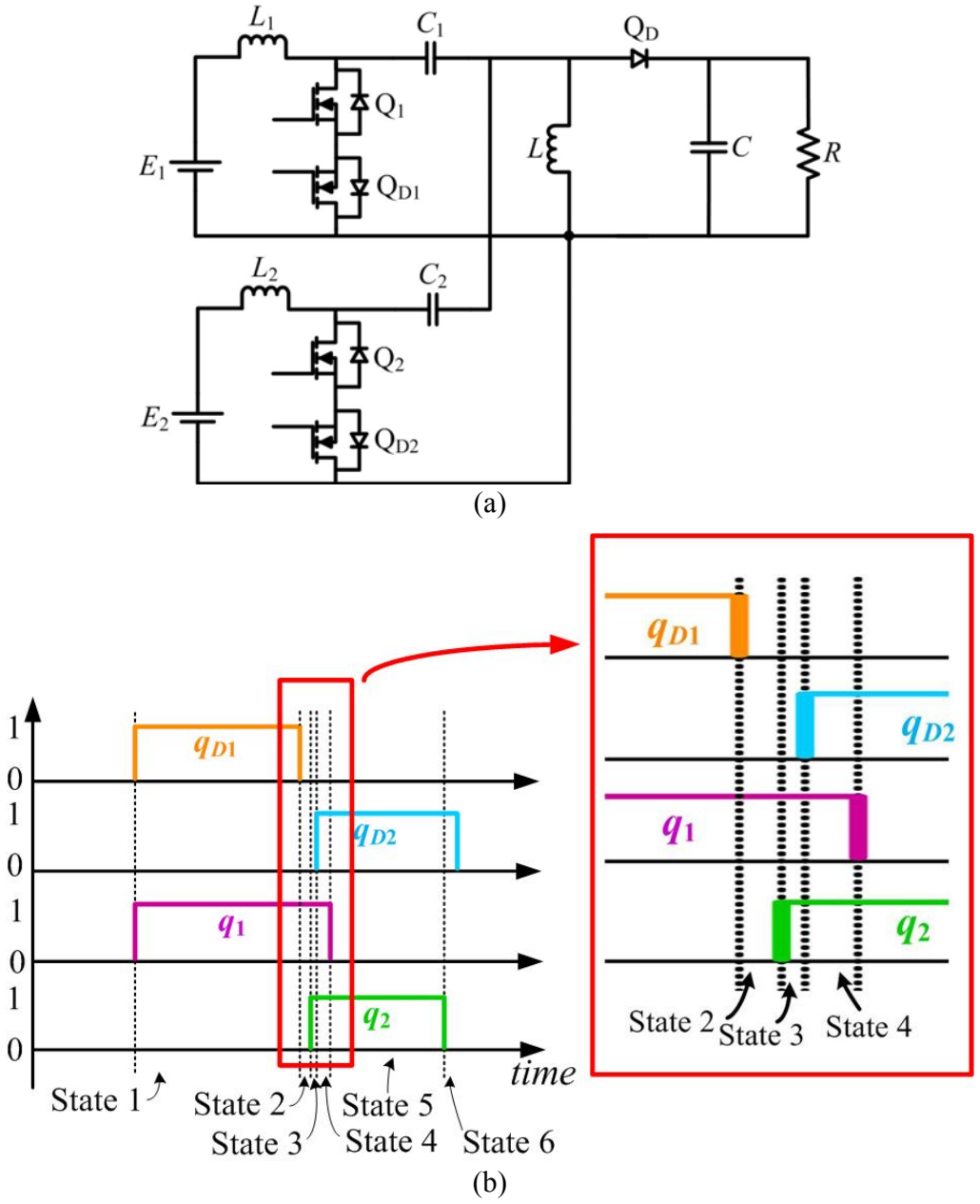

Figure 2.12: A Modified MI-SEPIC Topology and A Proposed Switching Control Strategy. (a) A Modified MI-SEPIC. (b) Switching Control Strategy 2.

State-by-State Analysis of the MI-SEPIC in Fig 2.12

According to the on-off states of the MOSFETs, one period can be divided into 6 states as displayed in Fig. 2.12 (b) and Table 2.

State	1	2	3	4	5	6	
v_{Q1} (V)	0	0	0	0	0	≈100	≈100
v_{QD1} (V)	0	0	0	0	-5 (reverse biased)	0	0
v_{Q2} (V)	11	11	0	0	0	≈100	≈100
v_{QD2} (V)	-6	-6	0	0	0	0	0
On Switches	Q_1 Q_{D1}	Q_1	Q_1 Q_2	Q_1 Q_2 Q_{D2}	Q_2 Q_{D2}	Q_D Q_{D2}	Q_D

Table 2: Experimentally Measured Voltages across MOSFETs during Six States in a Complete Period of the Proposed Driving Strategy in Fig. 2.12 (b).

State 1

Q_1, Q_{D1} are on. Q_2, Q_{D2} are off. In this state the first FCBB switch conducts current while the second FCBB switch and the output diode Q_D are open. This state corresponds to the first state in a conventional TM-MIC.

State 2

Q_{D1} turns off and only Q_1 is on. FCBB switch 1 still has current flowing through it due to the conduction of the body diode of Q_{D1}. In this state, the FCBB switch 2 and the output diode Q_D are still off.

State 3

Q_2 turns on. During this state Q_1 and Q_2 are on. Since $E_1 < E_2$, the FCBB switch 1 has to stop conducting current (because the body diode of the Q_{D1} would become reverse biased due to the voltage difference of the center capacitors) and FCBB switch 2 begins to conduct current. However, due to the parasitic inductance (along the loop consisting of Q_1, Q_{D1}, Q_2, Q_{D2}, C_2, and C_1), the current through FCBB switch 2 increases gradually. Since two MOSFETs in FCBB switch 2 start to conduct current, v_{DS} of both MOSFETs are zero in this state. Consequently, at the beginning of the next state,

Q_{D2} turns on with zero voltage. Note that, at the beginning of this state, the turn-on loss of Q_2 is almost zero due to a low v_{DS_Q2} as shown in Fig. 2.13 (b).

State 4

Q_{D2} turns on. Q_1, Q_2, and Q_{D2} are on in this state. According the analysis of the previous state, Q_{D2} is turned on with zero voltage (Fig. 2.13 (d)) at the beginning of this state. FCBB switch 2 continues to conduct current. Q_1 turns off at the end of this state.

State 5

Q_1 turns off. Q_2 and Q_{D2} are on. Because Q_1 is off, only FCBB switch 2 conducts current from this state. Hence, this State 5 corresponds to the second state of a conventional driving strategy shown in Fig. 2.1. Since v_{DS_Q1} is zero when Q_1 turns off (Table 2 and Fig. 2.13 (a)), no energy will be stored in the output capacitor C_{DS_Q1} during the turn-off transient. Hence, no energy will be dissipated in R_{DS_ON} of Q_1 when it turns on.

State 6

Q_2 turns off. Q_{D2} can either be on or off. FCBB switch 2 does not conduct current even if Q_{D2} is on. Regarding MOSFET Q_2, it is found that due to the low level of v_{DS_Q2} and the slope of current i_{DS_Q2}, there is little turn-on loss of Q_2 (see Fig. 2.13 (b)). Therefore, the considerable turn-on loss is in Q_2 can be reduced. In this state both FCBB switches stop conducting current. The only switch that conducts current is Q_D. Note that v_{DS_QD1} is zero in this state, so Q_{D1} will turn on with zero voltage in State 1 (see Fig. 2.13 (c)). The analysis of v_{DS_QD1} in State 6 is shown in the design considerations discussed in a later subsection.

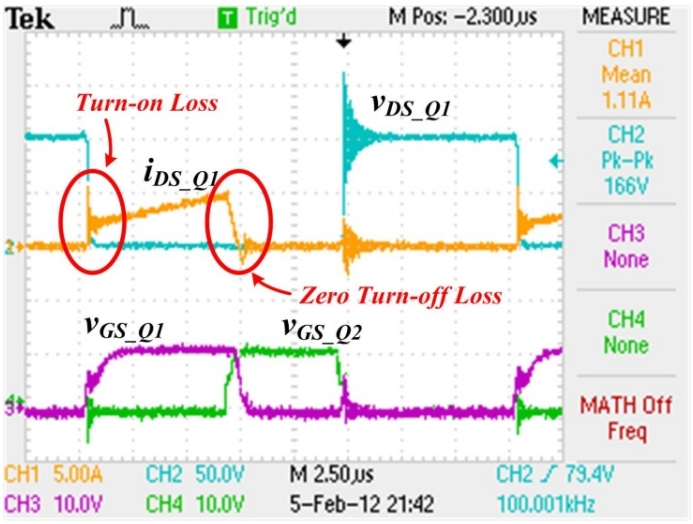
Tek
Trig'd
M Pos: -2.300µs
MEASURE
CH1
Mean
1.11A
CH2
Pk-Pk
166V
CH3
None
CH4
None
MATH Off
Freq
Turn-on Loss
v_{DS_Q1}
i_{DS_Q1}
Zero Turn-off Loss
v_{GS_Q1}
v_{GS_Q2}
CH1 5.00A
CH2 50.0V
M 2.50µs
CH2 ∕ 79.4V
CH3 10.0V
CH4 10.0V
5-Feb-12 21:42
100.001kHz

(a)

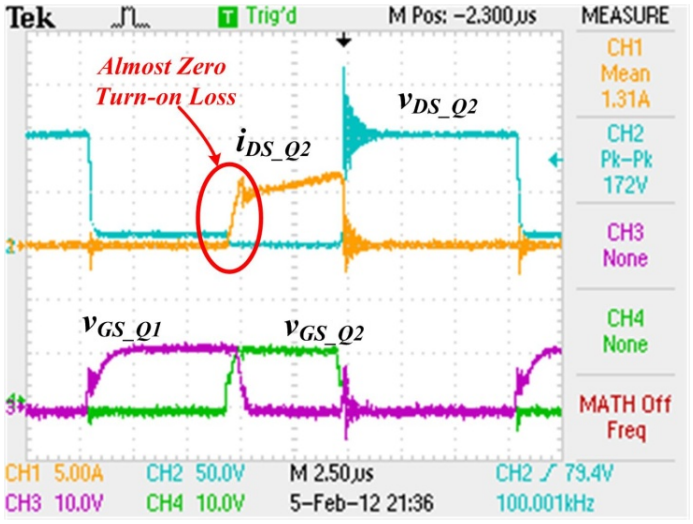
Tek
Trig'd
M Pos: -2.300µs
MEASURE
CH1
Mean
1.31A
CH2
Pk-Pk
172V
CH3
None
CH4
None
MATH Off
Freq
Almost Zero
Turn-on Loss
v_{DS_Q2}
i_{DS_Q2}
v_{GS_Q1}
v_{GS_Q2}
CH1 5.00A
CH2 50.0V
M 2.50µs
CH2 ∕ 79.4V
CH3 10.0V
CH4 10.0V
5-Feb-12 21:36
100.001kHz

(b)

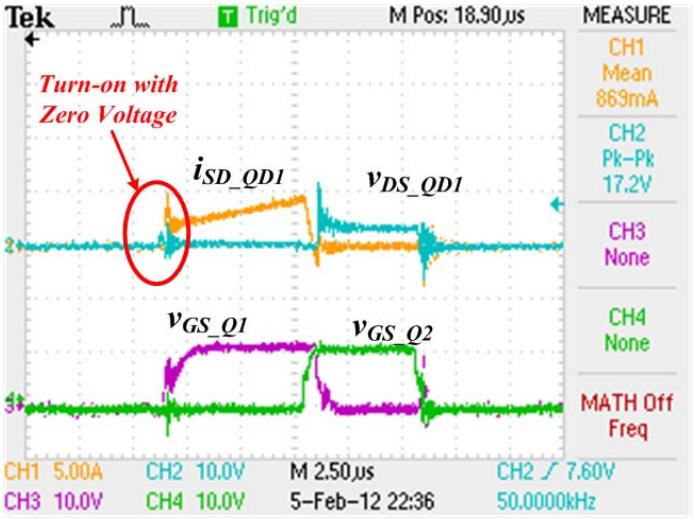

(c)

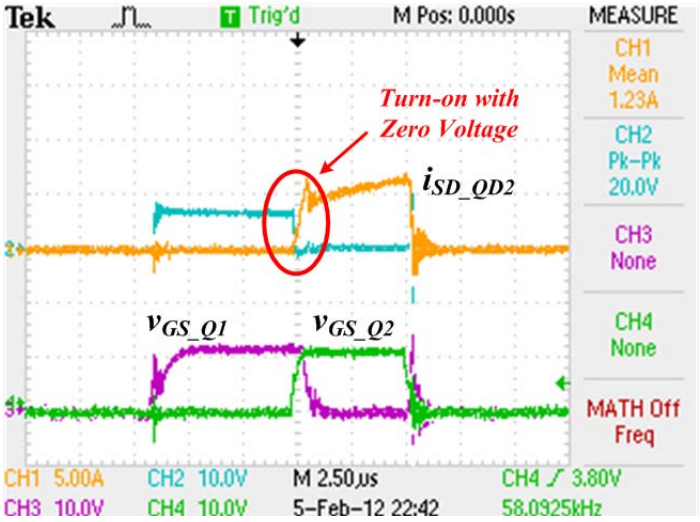

(d)

Figure 2.13: Current and Voltage Snapshots of the MOSFETs Q_1, Q_{D1}, Q_2, and Q_{D2}.

Switching Control Strategy Design Considerations

It is shown in the state-by-state analysis in the previous section that the switching control strategy in Fig. 2.12 (b) is essential in order to reduce loss in MOSFETs for the MI-SEPIC in Fig. 2.12 (a). From Fig. 2.12 (b) it is seen that the switching functions q_1 and q_{D1} (or q_2 and q_{D2}) are almost synchronized. The leading and trailing edges of the switching functions are carefully-designed to reduce switching loss. Key conditions satisfied by the proposed design (Fig. 2.12) are summarized as follows.

Condition 1

The first condition is that, for the switching strategy, q_1 and q_2 share a simultaneous on-time per period.

This condition ensures the current flowing through FCBB switch 1 is transferred (gradually) to FCBB switch 2, instead of the output switch Q_D. If this condition is not met, the output diode Q_D turns off twice per period, which would harm the efficiency. Since both MOSFETs in FCBB switch 2 conduct current right after Q_2 turns on, the MOSFET Q_{D2} can be turned on with zero voltage (Fig. 2.13 (d)). Also, note that this state leads to a transition of the currents in FCBB switches as shown in Fig. 2.14. During the current transition, all switches have current flowing through them. This transition becomes obvious when ΔE is small. Due to the parasitic inductance L_r along the path consists of C_1, Q_1, Q_{D1}, Q_{D2}, Q_2, and C_2, the loop current changes gradually with its slope equal to $\Delta E / L_r$. The current transition may further reduce the switching loss on Q_2 because the current is very small when turning on (Fig. 2.13 (b)).

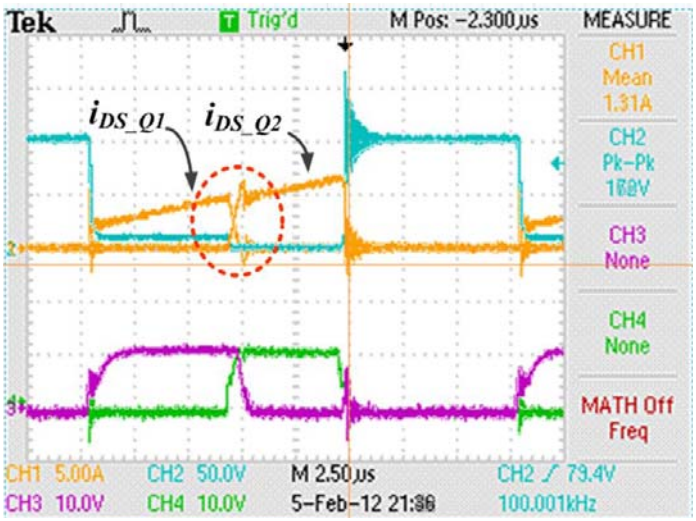

Figure 2.14: A Transition of the Currents Flowing through Q_1 and Q_2.

Condition 2

The second condition is that q_{D1} and q_2 are never on simultaneously.

In steady-states, $V_{C1}=E_1$, $V_{C2}=E_2$, and $V_{C1}<V_{C2}$ hold. As shown in Fig. 2.15, if Q_{D1} and Q_2 are both on, short circuit occurs in spite of the states of MOSFETs Q_1 and Q_{D2}. Figure 2.16 shows a large current in FCBB switch 2 is caused by the inappropriate state $q_{D1}=q_2=1$. The large current may deteriorate the efficiency and even damage the switches and needs to be strictly avoided. In the proposed driving strategy, the state $q_2=q_{D1}=1$ never occurs due to a dead time (State 3) is created, as shown in Fig. 2.12 (b).

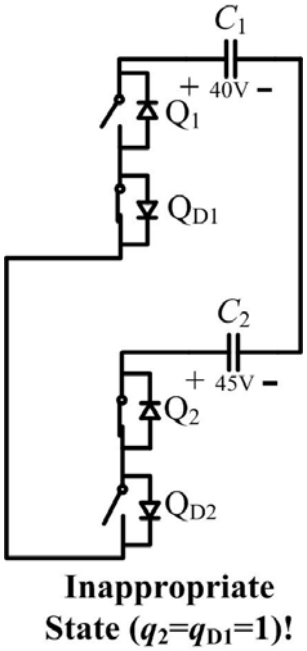

Figure 2.15: Short Circuit Occurs When $q_2=q_{D1}=1$.

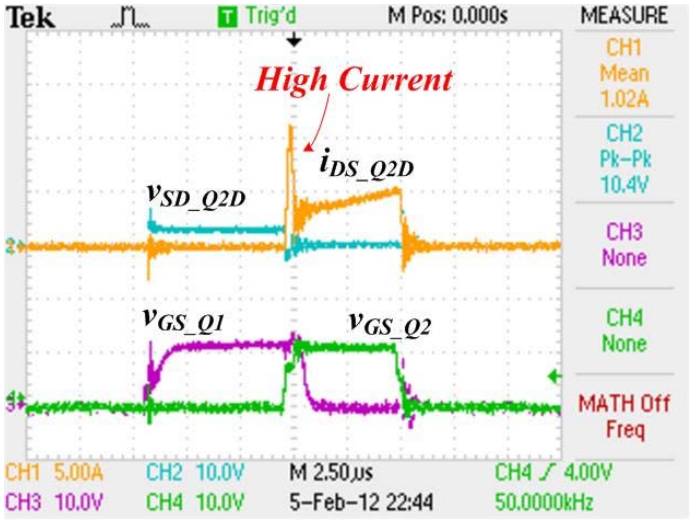

Figure 2.16: High Current Occurs Due to the Inappropriate State q_2=q_{D1}=1.

Condition 3

The upper MOSFETs (such as Q_1 and Q_2) are selected to have small output capacitance; The lower MOSFETs (such as Q_{D1}, Q_{D2}) are selected to have large output capacitance.

The third condition suggests the selection of the MOSFETs to achieve a low voltage level of v_{DS_Q2} in States 1. In State 6, v_{DS_Q2} and v_{DS_QD2} are v_{out}+E_2 and 0, respectively (see Fig. 2.13 (b) and (d)). Let the values of v_{DS_Q2}, v_{DS_QD2} in State 1 be x, y, respectively. Applying the Kirchhoff's voltage law to the loop consisting of Q_1, Q_{D1}, Q_2, Q_{D2}, C_2, and C_1 in State 1, it shows that

$$x + y = \Delta E \tag{2.7}$$

The output capacitance of a MOSFET is nonlinear because C_{DS} is dependent on v_{DS} [8]. The relationships hold for linear capacitors may not be extended to a nonlinear capacitor. Due to the series connection of MOSFETs and their reverse biased body diodes, both output capacitances of Q_2 and Q_{D2} conduct the same current (during the transient from State 6 to State 1):

$$i_{DS\_Q2}(t) = i_{DS\_QD2}(t) \tag{2.8}$$

which can be written as

$$C_{DS\_Q2}(v_{DS\_Q2})\frac{dv_{DS\_Q2}}{dt} = C_{DS\_QD2}(v_{DS\_QD2})\frac{dv_{DS\_QD2}}{dt}. \tag{2.9}$$

Integrating of both sides, it yields that

$$\int_{v_{out}+E_2}^{x} C_{DS\_Q2}(v_{DS\_Q2})dv_{DS\_Q2} = \int_{0}^{y} C_{DS\_QD2}(v_{DS\_QD2})dv_{DS\_QD2} \tag{2.10}$$

Then, x and y could be calculated once the C_{DS}-v_{DS} relationship of both MOSFETs are known, for example, by using an approximation given in [8].

A qualitative analysis could be performed by assuming that the output capacitances of the MOSFETs Q_2 and Q_{D2} are constants. Considering the charge flowing through C_{DS_QD2} and C_{DS_Q2} are the same and body diodes of Q_{D2} and Q_2 are both reverse-biased, the following equation can be derived:

$$C_{DS\_Q2} \cdot (V_{out} + E_2 - x) = C_{DS\_QD2} \cdot (0 - y). \tag{2.11}$$

Recall the assumption that ΔE is small and $V_{out} + E_2 >> \Delta E > 0$. With (2.7) and (2.11), x is solved and simplified as

$$x = \frac{C_{DS\_Q2}(V_{out} + E_2) + C_{DS\_QD2}\Delta E}{C_{DS\_Q2} + C_{DS\_QD2}} \approx \frac{V_{out} + E_2}{1 + C_{DS\_QD2} / C_{DS\_Q2}}. \tag{2.12}$$

Equation (2.12) shows that x decreases when C_{DS_QD2} / C_{DS_Q2} increases. Therefore, the third condition can be satisfied by choosing a relatively large C_{DS_QD2} / C_{DS_Q2}.

Similarly, v_{DS_QD1} in State 6 can be calculated by assuming constant C_{DS} of MOSFETs. In State 5, both MOSFETs in leg #1 are off. C_{DS_Q1}=0 V, $C_{DS\_QD1} = -\Delta E$ as shown in Table 2. Assume the voltage across MOSFETs Q_1 and Q_{D1} are x' and y', respectively. Then, the following relationships hold

$$x' + y' = v_{out} + E_1 \tag{2.13}$$

$$C_{DS\_QD1} \cdot (y' + \Delta E) = C_{DS\_Q1} \cdot x' \tag{2.14}$$

According to (2.13) and (2.14), it can be solved that

$$y' = \frac{C_{DS\_Q1} V_{out} + C_{DS\_Q1} E_1 - C_{DS\_QD1} \Delta E}{C_{DS\_Q1} + C_{DS\_QD1}} \tag{2.15}$$

Recall one of the assumptions that ΔE is small, (2.15) would yield a positive *y*'. However, a positive *y*' as large as the value in (2.15) is not realistic because the forward voltage drop of the body diode is almost zero (see Fig. 2.12 (a)); once the voltage across Q_{D1} increases from its initial negative value (e.g., -5 V in Table 2) to zero, it stops increasing due to the forward conduction voltage of the body diode of Q_{D1}. Therefore, the voltage across MOSFET Q_{D1} is zero before turning on, which allows Q_{D1} to turn on with zero voltage.

Summary of Efficiency Improvement

In summary, according to the illustration above, the efficiency improvement of the MI-SEPIC can be explained in three ways. Firstly, for MOSFET Q_2, although energy is stored to its output capacitance C_{DS_Q2}, its turn-on loss is little because v_{DS_Q2} drops to a very low level before Q_2 turns on. Small v_{DS_Q2} in State 1 and 2 is achieved because at the beginning of State 1 the energy stored in C_{DS_Q2} flows out of FCBB switch 2 and charges the center capacitors C_1 and C_2. Slow rising rate of i_{DS_Q2} in State 1 may further reduce the turn-on loss in Q_2 (Fig. 2.13 (b)). Secondly, both MOSFETs Q_{D1} and Q_{D2} turns on with zero voltages (Fig. 2.13 (c-d)). Thirdly, both MOSFETs Q_{D1} and Q_{D2} achieve synchronous rectification of the diodes MI-SEPIC in Fig. 1.9.

Note that the proposed design cannot completely eliminate the turn-on power loss in Q_1 because the energy stored in the C_{DS_Q1} still dissipates in the $R_{DS\_ON\_Q1}$ at the beginning of State 1. However, it can be found that the turn-on power loss is still reduced in the proposed design, because that 1) at the beginning of a period, the switch current

i_{DS_Q1} is relatively small (see Fig. 2.13 (a)); 2) the output capacitance of Q_1 is selected to be small so it stores less energy with a fixed v_{DS_Q1}. Hence, with the proposed design, the overall efficiency of the modified MI-SEPIC stays high because MOSFETs Q_{D1}, Q_{D2}, and Q_2 have little loss and MOSFET Q_1 has reduced loss.

Extension to a Three-input SEPIC

The design modifications on both switch realization and switching control for a dual-input SEPIC can be conveniently extended to a general case with more inputs. Without loss of generality, consider a three-input SEPIC for example (Fig. 2.17) and consider the added input leg incorporates a higher input voltage so the new input leg is named leg 3. Note that, $E_1<E_2<E_3$ and the differences among three-input voltages are small. The FCBB configuration design in input leg 3 follows leg 1 or 2. The extended switching functions allowing for high efficiency of a three-input SEPIC is plotted in Fig. 2.18. The operation of FCBB switch 3 in input leg 3 is analogous to FCBB switch 2 when driving by the switching functions in Fig. 2.18. The same power loss analysis as a dual-input SEPIC in Fig. 2.12 (a) extends to the three-input case in Fig. 2.17. It could be conveniently verified that, the additional switches do not introduce more losses and only Q_1 presents turn-on loss.

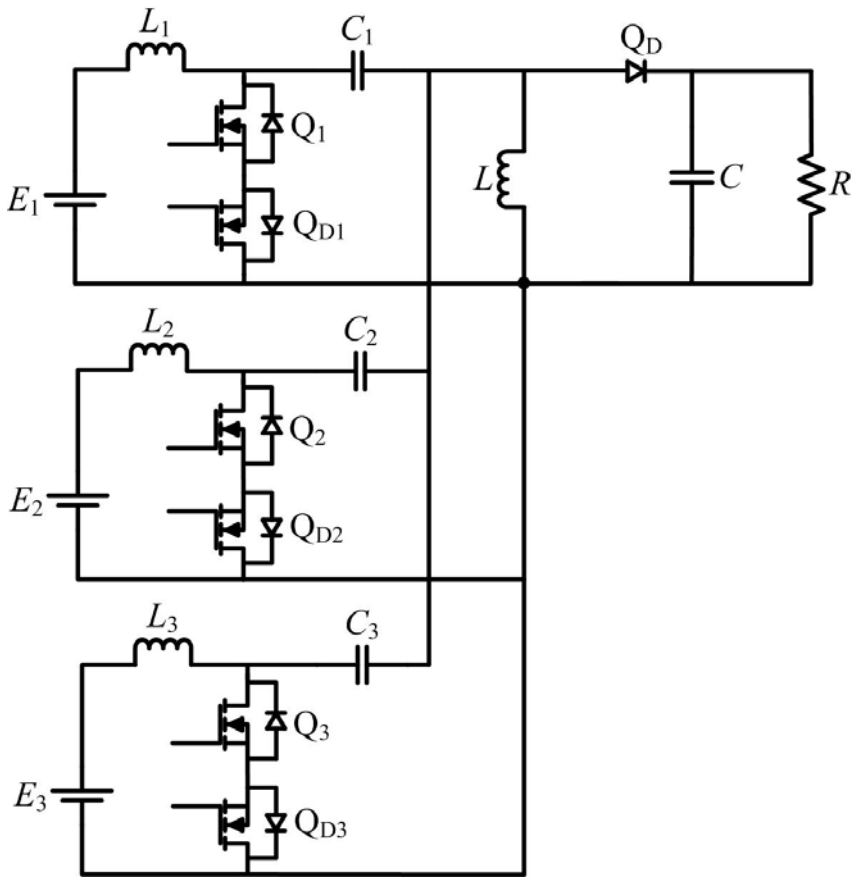

Figure 2.17: A Three-input SEPIC.

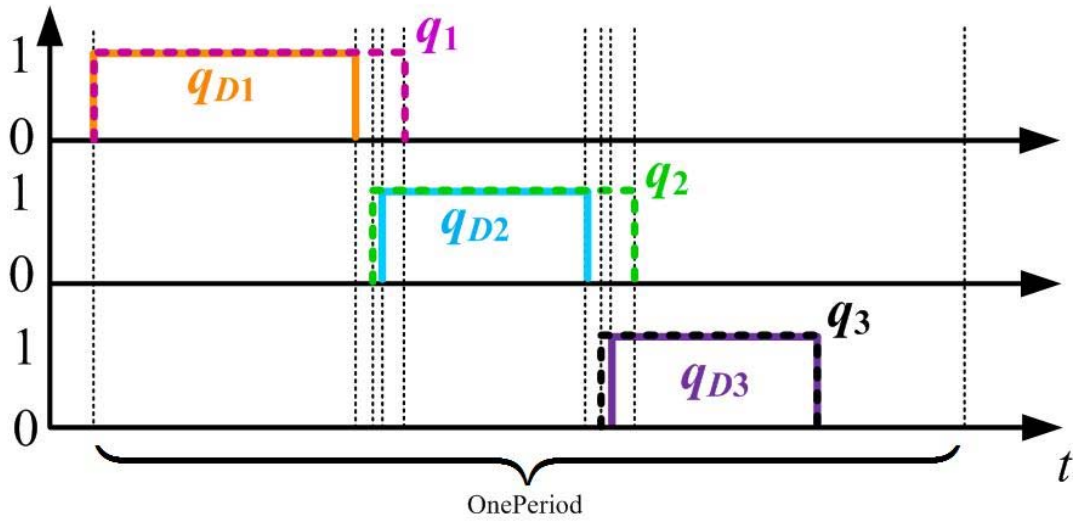

Figure 2.18: A Switching Control of a Highly-Efficient Three-input SEPIC.

Extension to Other TM-MICs

The MI-Ćuk

The proposed switching control can be directly applied to an MI-Ćuk converter in Fig. 2.3, since the analyses of the low turn-on loss conditions are similar to an MI-SEPIC: Q_{D2} can turn on with zero voltage right after Q_2 turns on; v_{DS_QD1} can reach zero in State 6 so Q_{D1} turns on with zero voltage; small v_{DS_Q2} can be verified by the same analysis for the MI-SEPIC.

The MI-buck-boost Converter

A conventional MI-buck-boost converter is shown in Fig. 2.19 (a). Difficulty is found when attempting to extend the proposed switching control in Fig. 2.12 (b) to a modified MI-buck-boost converter in Fig. 2.19 (b) due to the absence of (center) capacitors. For example, to analyze the power loss in Q_2 in the MI-buck-boost in Fig. 2.19 (b), the path consists of Q_1, Q_{D1}, Q_2, Q_{D2}, E_2, and E_1; the output capacitance C_{DS_Q2} discharges and creates a reverse current through E_2. The reverse current flowing through E_2 or E_1 may cause problems, e.g., it may lead to overheat and may even destroy PV modules [71]. This issue may be addressed by adding an internal diode and an input capacitor to each input leg, as shown in Fig. 2.19 (c). By applying the proposed switching control on the topology shown in Fig. 2.19 (c), the high power loss in Q_2 could be reduced.

Hence, the proposed switching control may not be suitable to the MI-buck-boost in Fig. 2.19 (b) because of the reverse current; on the other hand, it could be used to improve the efficiency of the topology in Fig. 2.19 (c) with a compromised parts-count.

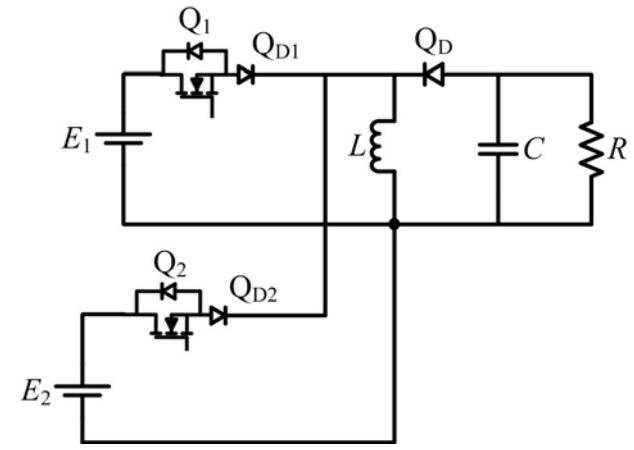

(a)

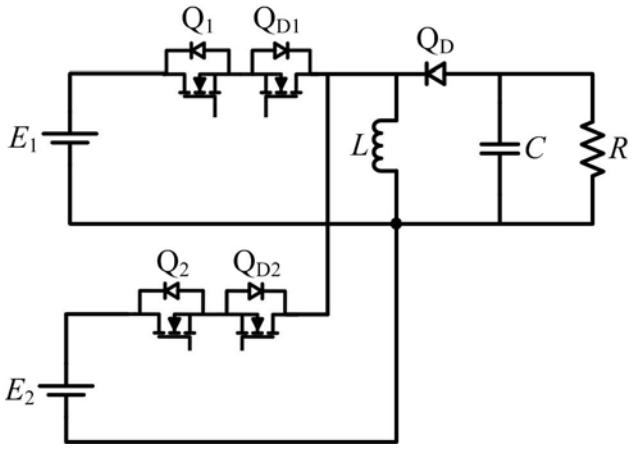

(b)

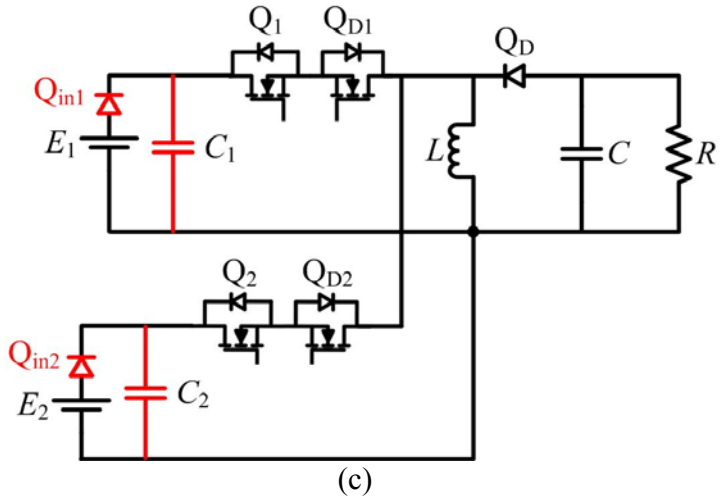

(c)

Figure 2.19: The MI-buck-boost Converter. (a) A Conventional Topology. (b) Modified Topology 1. (c) Modified Topology 2.

Experimental Results

The high efficiency of the MI-SEPIC in Fig. 2.12 (a) driven by the switching function shown in Fig 2.12 (b) is verified by experiments. To satisfy condition 3, MOSFETs Q_1 and Q_2 were realized with Fairchild Semiconductor FQA44N30 and MOSFETs Q_{D1} and Q_{D2} were realized with International Rectifier IRFPS3810PbF; Q_D was realized with STMicroelectronics STTH6003CW. The input and output power of the MI-SEPIC, shown in Fig. 2.12, was measured by the Yokogawa WT-500 power analyzer. Efficiency was evaluated by gradually increasing both input voltages from 5 V and 10 V to around 60 V. This was done while maintaining a difference of 5 V between sources and holding the duty ratios and load resistance constant. Then both duty ratios were increased to further raise the output power. The efficiency test is shown as the curve in Fig. 2.20. It is found that the efficiency reaches a maximum of almost 96 %. It remains above 95 % for up to 105 W, and over 94 % for the remainder of the intended operating range. Considering the relatively low voltage and laboratory environment involved in the prototyping—e.g. use of self wound inductors—these efficiency values are very high. The MI-SEPIC is therefore a good candidate for applications that require high power conversion efficiency such as photovoltaic modules [72] and computer servers [73].

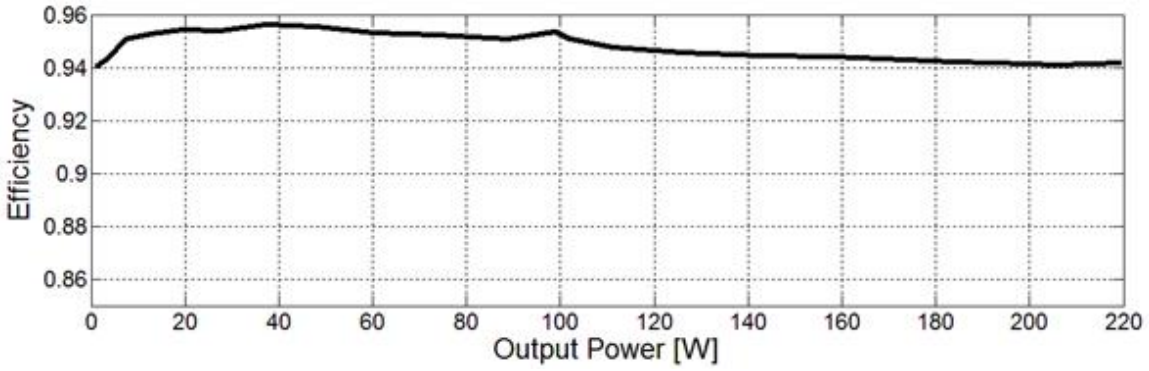

Figure 2.20: Efficiency Test Results with $R = 72\ \Omega$.

Chapter 3: Modeling of Multiple-Input DC-DC Converters Considering Switching Control Interactions

In this chapter, the modeling issue of multiple-input converters subject to the time-multiplexing switching control is discussed. The modeling error caused by a conventional approach, the state-space averaging method, is revealed. The modeling accuracy can be improved by a multi-frequency method (or a generalized averaging method).

MODELING ISSUE OF THE MI-SEPIC

Input Current Errors of an MI-SEPIC

Consider a classical averaging approach in [74-75] for conventional power converters in continuous conduction mode (CCM) that, under the linear assumption [74], when averaging step is applied to the switched dynamic equation, it is observed that the average of the terms $q_1 i_{L1}$ and $(1\text{-}q_1) i_{L1}$ are equal to $D_1 I_{L1}$ and $(1\text{-}D_1) I_{L1}$, respectively, as illustrated in Fig. 3.1. Similarly, if the average of $q \cdot x$ is approximated by $D \cdot X$ in a dual-input SEPIC, the SSA model of the MIC can be derived. The equilibrium point (EP) of the SSA model of the topology in Fig. 1.9 is given by

$$X_{SSA}{}^{T} = \begin{pmatrix} I_{L1} & I_{L2} & I_L & V_{C1} & V_{C2} & V_C \end{pmatrix} = \begin{pmatrix} \frac{D_1 V_{out}}{(1-D_2)R} & \frac{D_{2,eff} V_{out}}{(1-D_2)R} & \frac{V_{out}}{R} & E_1 & E_2 & V_{out} \end{pmatrix}. \quad (3.1)$$

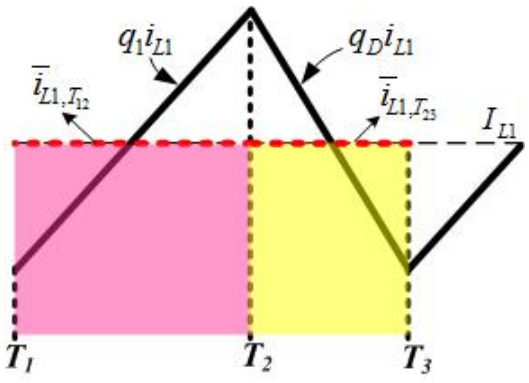

Figure 3.1: Inductor Current of an SIC.

Assume that a switching function in Fig. 2.1 is used here for illustration. By definition, the exact approach to calculate the average values of the state variables of an MI-SEPIC is by integrating their time function over a complete period, as presented in

$$X = \frac{1}{T}[\int_{t}^{t+D_1T} x(\tau)d\tau + \int_{t+D_1T}^{t+D_2T} x(\tau)d\tau + \int_{t+D_2T}^{t+T} x(\tau)d\tau] \tag{3.2}$$

where T denotes the period. Based on (3.2), assume the state variables are piecewise linear, the EP is given by

$$\begin{aligned} X^T &= \begin{pmatrix} I_{L1} & I_{L2} & I_L & V_{C1} & V_{C2} & V_C \end{pmatrix} \\ &= \begin{pmatrix} \dfrac{D_1V_{out}}{(1-D_2)R} - \dfrac{D_1D_{2,eff}E_2}{2L_ef} & \dfrac{D_{2,eff}V_{out}}{(1-D_2)R} + \dfrac{D_1D_{2,eff}E_1}{2L_ef} & \dfrac{V_{out}}{R} & E_1 & E_2 & V_{out} \end{pmatrix} \end{aligned} \tag{3.3}$$

where L_e is the parallel combination of all the inductors. Comparing (3.1) and (3.3), one dc offset term appears in input currents I_{L1} and I_{L2}, respectively. This offset is proportional to the input voltage and effective duty ratios of the other leg, and inversely proportional to an equivalent parallel inductor L_e and to the switching frequency f. Still, (3.3) shows that the center capacitor voltage values are the same as their corresponding input voltages, which can be verified by a steady state dc analysis. The inductor current value i_L can also be determined by the same dc analysis.

Explanations of the Error Given by the SSA

A fundamental assumption of the SSA is violated in the case of the MI-SEPIC, that the A matrices that represent the dynamic behavior of each individual switch state commute. That is, the steady state average value of a state variable obtained from the SSA model is exact only if any two matrices of A_1, A_2 , and A_3 are commutable, that is $A_iA_j = A_jA_i$ (i, j=1, 2, 3, $i \neq j$). However, according to their analytical forms derived from (2.1), none of the commutable conditions holds.

Reference [76] reveals that the SSA approach does not necessarily average the state variables of single-input PWM converters operating in discontinuous conduction

mode (DCM). A similar issue occurs when SSA is applied to MICs. This approach leads to issues when representing the fast average products of state variables and switching functions. For instance, as shown in Fig. 3.2, the average of the term $q_1 i_{L1}$ is clearly smaller than I_{L1}. These discrepancies show that, although the SSA approach uses the fast average to approximate the true average of the state variable, in the case of the TM-MIC modeling, the approximation fails because of the TM nature of the MI-SPIEC: the switching functions of FCBB switches are interacting or dependent on each other. This work focuses on addressing this issue caused by the switching control interaction.

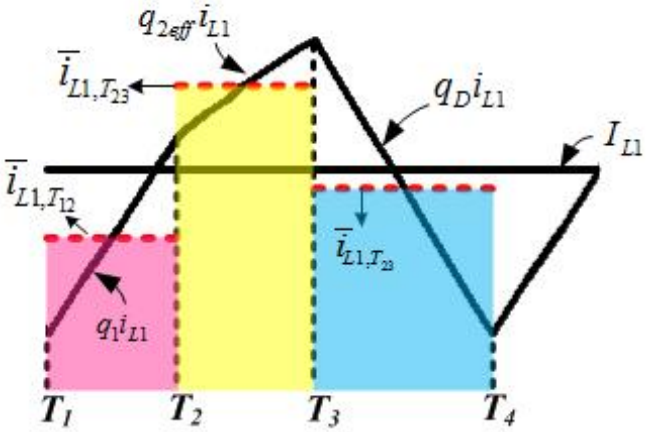

Figure 3.2: Inductor Current (i_{L1}) of an MI-SEPIC.

Input Current Errors of other MICs

In some other MICs such as a two-input buck-boost converter shown in Fig. 2.19, the average current of the common output inductor calculated based on (3.2) shows a parameter-dependent behavior analogous to that obtained for I_{L1} and I_{L2} in (3.3). The result is presented through (3.4):

$$I_{L\_MI\text{-}Buck\text{-}Boost} = \frac{V_{out}}{(1-D_2)R} + \frac{D_1 D_{2,eff}(E_1 - E_2)}{2Lf}. \tag{3.4}$$

It can be found from (3.4) that, when E_1=E_2, the inductor current dc offset terms disappear for the MI-buck-boost. However, the input currents dc offsets still exist because,

when the average input currents are calculated, the dc-offset terms are found to be the same as those of an MI-SEPIC, by substituting L_e with L.

The average input currents are also derived for a three-input SEPIC:

$$\begin{bmatrix} I_{L1} \\ I_{L2} \\ I_{L3} \end{bmatrix} = \begin{bmatrix} \frac{D_1 V_{out}}{(1-D_3)R} - \frac{D_1 D_{2,eff} E_2}{2L_e f} - \frac{D_1 D_{3,eff} E_3}{2L_e f} \\ \frac{D_{2,eff} V_{out}}{(1-D_3)R} + \frac{D_{2,eff} D_1 E_1}{2L_e f} - \frac{D_{2,eff} D_{3,eff} E_3}{2L_e f} \\ \frac{D_{3,eff} V_{out}}{(1-D_3)R} + \frac{D_{3,eff} D_1 E_1}{2L_e f} + \frac{D_{3,eff} D_{2,eff} E_2}{2L_e f} \end{bmatrix} \tag{3.5}$$

The offsets in both two-input and three-input cases show that each input current is affected by input voltages and effective duty cycles of all other inputs; the sign of the one input current's offset depends on the conduction sequence of each respective switch. For example, the offset term of E_3 on I_{L1} is negative because in any given period the switch of input leg #3 conducts current after the switch input leg #1. Hence, for the n-input case, the first input current—the one corresponding to $q_1(t)$—and the last input current—the one corresponding to $q_{n,eff}(t)$—may present the highest offsets.

MULTI-FREQUENCY MODELING FOR THE MI-SEPIC

In [76], based on the SSA model, a simple coefficient matrix merely depending on duty cycles is derived to model SICs in DCM. A similar coefficient matrix for the case of TM-MICs is more complex because it depends on duty cycles, component parameters, the operating point, and the converter topology. Although its derivation is still possible, it is eventually an indirect way to address control coupling effects because there is no appropriate model for the time-dependent switching functions.

Previous work on the multi-frequency (MF) method focuses on its application on conventional converters. Those studies come up with representations with higher accuracy for conventional power converters, which are known as frequency-dependent models. This dissertation studies switching control interaction effects in TM-MICs through the MF

approach. The choice of the MF approach can be justified by the fact that the frequency and phase information of switching functions can be included in an MF model. Therefore, in contrast to the frequency-dependent model in previous work, a frequency-phase-dependent model will be derived for an MI-SEPIC (Fig. 1.9 (a)).

In this section, MF approach fundamentals are reviewed. For more details of the application of the MF approach on conventional power converters, readers can refer to [77-80]. Although the MF method has been applied to MICs in this one case in the past [81] for MI-Boost and MI-buck-boost converters, its application in [81] seems limited. One reason is that the MI-Boost is effectively a parallel combination of single-input boost converters, so the SSA may achieve sufficient modeling accuracy. Furthermore, for the MI-buck-boost, the modeling issue of the SSA, which is caused by the TM switching function, is not clearly stated. Also, the converter was only studied at the common output stage. Thus, behavior of individual input currents was not considered as part of the MF model in [81]. One alternative not explored in [81] could have been to use current input filters so input currents would become state variables that could be directly included in the MF model. In here, an MI-SEPIC, in Fig. 1.9 was used to motivate the discussion because of its operational advantages over other MICs. Yet, the analysis can be easily generalized to other MIC topologies, such as the MI-Ćuk in [34, 53], the MI-buck-boost in [24], and any other MICs that are based on a TM scheme. The modeling error of SSA and the improvement of the derived model were demonstrated via simulations and experiments.

Definition of Fourier Series

The MF method involves time-dependent Fourier coefficients. Based on the complex Fourier series, the real-valued signal $x(t)$, can be expressed on the interval $t \in [t-T, t]$ as

$$x(t) = \sum_{n=-\infty}^{\infty} \langle x \rangle_n (t) e^{jn\omega\tau} \tag{3.6}$$

where $\omega = 2\pi / T$, $j = \sqrt{-1}$, n is integer, and the $\langle x \rangle_n (t)$—which is referred to as the index-n average or index-n coefficient—are the complex Fourier coefficients given by

$$\langle x \rangle_n (t) = \frac{1}{T} \int_{t-T}^{t} x(\tau) e^{-jn\omega\tau} d\tau \,. \tag{3.7}$$

The accuracy of generalized averaging model can be improved by considering more harmonics.

Fundamental Properties

Multi-frequency modeling involves obtaining the time-derivatives of the index-n coefficients of state variables. Some important properties that simplify the analysis are briefly summarized next.

Differentiation with Respect to Time

The time derivative of the index-n average is given by

$$\frac{d\langle x \rangle_n (t)}{dt} = \left\langle \frac{dx}{dt} \right\rangle_n (t) - jn\omega \cdot \langle x \rangle_n (t) \,. \tag{3.8}$$

Discrete Convolution

In order to calculate the index-n average of a product term such as $q(t)x(t)$, the relationship presented in (3.9) is useful:

$$\langle x(t) \cdot y(t) \rangle_n = \sum_{i=-\infty}^{\infty} \langle x(t) \rangle_{n-i} \langle y(t) \rangle_i \,. \tag{3.9}$$

Fourier Series Coefficients of a Switching Function

The Fourier series coefficients of a switching function $q(t)$ can be calculated with the following formulas

$$\langle q \rangle_0 = D \tag{3.10}$$

$$\langle q \rangle_n = \frac{1}{2jn\pi} \cdot (1 - e^{-2\pi njD}) \cdot e^{-jn\phi} \tag{3.11}$$

where D is the duty ratio and ϕ is the phase shift of the switching function $q(t)$. Hence, both duty ratio and phase shift are included in the MF model. Note that, the information of phase shifts of switching functions could not be included in an SSA model.

Additionally, useful properties include

$$\langle x \rangle_n = \langle x \rangle_{-n}^* \tag{3.12}$$

where the star symbol denotes complex conjugate. If X is constant, the Fourier coefficients are given by

$$\langle X \rangle_0 = X, \ \langle X \rangle_n = 0 \tag{3.13}$$

where n is a non-zero integer.

MF Model Description

We consider n—the order of the averages—up to ± 1 for a dual-input SEPIC shown in Fig. 1.9. That is, only index-0 and index-1 components are considered. Higher order averages are considered negligible. In order to avoid involving the calculation of complex numbers, a transformation illustrated in [78] was applied in this analysis. Based on the dynamic equations in (2.1) and properties indicated by (3.8)-(3.13), the MF model for an MI-SEPIC can be expressed through an 18 by 18 system in (3.14)

$$\frac{d}{dt}\begin{bmatrix} \langle x \rangle_0(t) \\ \langle x \rangle_{1'}(t) \end{bmatrix} = A_{MF} \cdot \begin{bmatrix} \langle x \rangle_0(t) \\ \langle x \rangle_{1'}(t) \end{bmatrix} + B_{MF} \qquad A_{MF} = \begin{bmatrix} A_{11} & A_{12} \\ A_{21} & A_{22} \end{bmatrix} \tag{3.14}$$

where the variables are given in (3.15)-(3.16) and the matrices A_{11} to A_{22} are detailed in (3.17)-(3.20). In particular, the SSA model is a special case of the MF model when the effects of harmonics are completely neglected. Note that $\langle x \rangle_{1'}(t)$ in (3.14) is not strictly the vector of index-1 averages but it includes the real parts and imaginary parts of the index-1 averages. As described in [78], the index-1 averages $\langle x \rangle_1(t)$ can be calculated through simple algebra from $\langle x \rangle_{1'}(t)$.

As indicated in (3.14), A_{MF} can be partitioned into four matrices. The seemingly complicated matrix A_{MF} can be conveniently derived by partitioning the 18 by 18 matrix into matrices A_{11} to A_{22}, which share a similar structure. The dynamic relationships can be illustrated in Fig. 3.3. Notice that the dynamics of $\langle x \rangle_0(t)$ and $\langle x \rangle_{1'}(t)$ interact with each other through A_{12} and A_{21}. A_{11} is a 6 by 6 matrix, which is of the same form than the A matrix of the SSA model; A_{12}, A_{21}, A_{22} are 6 by 12, 12 by 6, and 12 by 12 matrices, respectively, which represent the interactions from high index to index-0 averages, from the index-0 to high index averages, and among high index averages, respectively, as shown in Fig. 3.3; B_{MF} is an 18 by 1 vector, in which all terms are 0 except for the first two which are E_1/L_1 and E_2/L_2, respectively.

$$\langle x \rangle_0(t) = [\langle i_{L1} \rangle_0 \quad \langle i_{L2} \rangle_0 \quad \langle i_L \rangle_0 \quad \langle v_{C1} \rangle_0 \quad \langle v_{C2} \rangle_0 \quad \langle v_C \rangle_0]^T \tag{3.15}$$

$$\langle x \rangle_{1'}(t) = [\langle i_{L1} \rangle_1^R \quad \langle i_{L1} \rangle_1^I \quad \langle i_{L2} \rangle_1^R \quad \langle i_{L2} \rangle_1^I \quad \langle i_L \rangle_1^R \quad \langle i_L \rangle_1^I \quad \langle v_{C1} \rangle_1^R \quad \langle v_{C1} \rangle_1^I \quad \langle v_{C2} \rangle_1^R \quad \langle v_{C2} \rangle_1^I \quad \langle v_C \rangle_1^R \quad \langle v_C \rangle_1^I]^T \tag{3.16}$$

$$A_{11} = \begin{bmatrix} 0 & 0 & 0 & \dfrac{-\langle q_{2,eff} \rangle_0 - \langle q_D \rangle_0}{L_1} & \dfrac{\langle q_{2,eff} \rangle_0}{L_1} & -\dfrac{\langle q_D \rangle_0}{L_1} \\ 0 & 0 & 0 & \dfrac{\langle q_1 \rangle_0}{L_2} & \dfrac{-\langle q_1 \rangle_0 - \langle q_D \rangle_0}{L_2} & -\dfrac{\langle q_D \rangle_0}{L_2} \\ 0 & 0 & 0 & \dfrac{\langle q_1 \rangle_0}{L} & \dfrac{\langle q_{2,eff} \rangle_0}{L} & -\dfrac{\langle q_D \rangle_0}{L} \\ \dfrac{1-\langle q_1 \rangle_0}{C_1} & -\dfrac{\langle q_1 \rangle_0}{C_1} & -\dfrac{\langle q_1 \rangle_0}{C_1} & 0 & 0 & 0 \\ -\dfrac{\langle q_{2,eff} \rangle_0}{C_2} & \dfrac{\langle q_1 \rangle_0 + \langle q_D \rangle_0}{C_2} & -\dfrac{\langle q_{2,eff} \rangle_0}{C_2} & 0 & 0 & 0 \\ \dfrac{\langle q_D \rangle_0}{C} & \dfrac{\langle q_D \rangle_0}{C} & \dfrac{\langle q_D \rangle_0}{C} & 0 & 0 & -\dfrac{1}{R \cdot C} \end{bmatrix} \tag{3.17}$$

$$A_{12}=\begin{bmatrix} 0 & 0 & 0 & 0 & 0 & 0 & \frac{-2\langle q_{2,eff}\rangle_1^R-2\langle q_D\rangle_1^R}{L_1} & \frac{-2\langle q_{2,eff}\rangle_1^I-2\langle q_D\rangle_1^I}{L_1} & \frac{2\langle q_{2,eff}\rangle_1^R}{L_1} & \frac{2\langle q_{2,eff}\rangle_1^I}{L_1} & \frac{-2\langle q_D\rangle_1^R}{L_1} & \frac{-2\langle q_D\rangle_1^I}{L_1} \\ 0 & 0 & 0 & 0 & 0 & 0 & \frac{2\langle q_1\rangle_1^R}{L_2} & \frac{2\langle q_1\rangle_1^I}{L_2} & \frac{-2\langle q_1\rangle_1^R-2\langle q_D\rangle_1^R}{L_2} & \frac{-2\langle q_1\rangle_1^I-2\langle q_D\rangle_1^I}{L_2} & \frac{-2\langle q_D\rangle_1^R}{L_2} & \frac{-2\langle q_D\rangle_1^I}{L_2} \\ 0 & 0 & 0 & 0 & 0 & 0 & \frac{2\langle q_1\rangle_1^R}{L} & \frac{2\langle q_1\rangle_1^I}{L} & \frac{2\langle q_{2,eff}\rangle_1^R}{L} & \frac{2\langle q_{2,eff}\rangle_1^I}{L} & \frac{-2\langle q_D\rangle_1^R}{L} & \frac{-2\langle q_D\rangle_1^I}{L} \\ \frac{-2\langle q_1\rangle_1^R}{C_1} & \frac{-2\langle q_1\rangle_1^I}{C_1} & \frac{-2\langle q_1\rangle_1^R}{C_1} & \frac{-2\langle q_1\rangle_1^I}{C_1} & \frac{-2\langle q_1\rangle_1^R}{C_1} & \frac{-2\langle q_1\rangle_1^I}{C_1} & 0 & 0 & 0 & 0 & 0 & 0 \\ \frac{-2\langle q_{2,eff}\rangle_1^R}{C_2} & \frac{-2\langle q_{2,eff}\rangle_1^I}{C_2} & \frac{-2\langle q_{2,eff}\rangle_1^R}{C_2} & \frac{-2\langle q_{2,eff}\rangle_1^I}{C_2} & \frac{-2\langle q_{2,eff}\rangle_1^R}{C_2} & \frac{-2\langle q_{2,eff}\rangle_1^I}{C_2} & 0 & 0 & 0 & 0 & 0 & 0 \\ \frac{2\langle q_D\rangle_1^R}{C} & \frac{2\langle q_D\rangle_1^I}{C} & \frac{2\langle q_D\rangle_1^R}{C} & \frac{2\langle q_D\rangle_1^I}{C} & \frac{2\langle q_D\rangle_1^R}{C} & \frac{2\langle q_D\rangle_1^I}{C} & 0 & 0 & 0 & 0 & 0 & 0 \end{bmatrix} \tag{3.18}$$

$$A_{21}=\begin{bmatrix} 0 & 0 & 0 & \frac{-\langle q_{2,eff}\rangle_1^R-\langle q_D\rangle_1^R}{L_1} & \frac{\langle q_{2,eff}\rangle_1^R}{L_1} & \frac{-\langle q_D\rangle_1^R}{L_1} \\ 0 & 0 & 0 & \frac{-\langle q_{2,eff}\rangle_1^I-\langle q_D\rangle_1^I}{L_1} & \frac{\langle q_{2,eff}\rangle_1^I}{L_1} & \frac{-\langle q_D\rangle_1^I}{L_1} \\ 0 & 0 & 0 & \frac{\langle q_1\rangle_1^R}{L_2} & \frac{-\langle q_1\rangle_1^R-\langle q_D\rangle_1^R}{L_2} & \frac{-\langle q_D\rangle_1^R}{L_2} \\ 0 & 0 & 0 & \frac{\langle q_1\rangle_1^I}{L_2} & \frac{-\langle q_1\rangle_1^I-\langle q_D\rangle_1^I}{L_2} & \frac{-\langle q_D\rangle_1^I}{L_2} \\ 0 & 0 & 0 & \frac{\langle q_1\rangle_1^R}{L} & \frac{\langle q_{2,eff}\rangle_1^R}{L} & \frac{-\langle q_D\rangle_1^R}{L} \\ 0 & 0 & 0 & \frac{\langle q_1\rangle_1^I}{L} & \frac{\langle q_{2,eff}\rangle_1^I}{L} & \frac{-\langle q_D\rangle_1^I}{L} \\ \frac{-\langle q_1\rangle_1^R}{C_1} & \frac{-\langle q_1\rangle_1^R}{C_1} & \frac{-\langle q_1\rangle_1^R}{C_1} & 0 & 0 & 0 \\ \frac{-\langle q_1\rangle_1^I}{C_1} & \frac{-\langle q_1\rangle_1^I}{C_1} & \frac{-\langle q_1\rangle_1^I}{C_1} & 0 & 0 & 0 \\ \frac{-\langle q_{2,eff}\rangle_1^R}{C_2} & \frac{-\langle q_{2,eff}\rangle_1^R}{C_2} & \frac{-\langle q_{2,eff}\rangle_1^R}{C_2} & 0 & 0 & 0 \\ \frac{-\langle q_{2,eff}\rangle_1^I}{C_2} & \frac{-\langle q_{2,eff}\rangle_1^I}{C_2} & \frac{-\langle q_{2,eff}\rangle_1^I}{C_2} & 0 & 0 & 0 \\ \frac{\langle q_D\rangle_1^R}{C} & \frac{\langle q_D\rangle_1^R}{C} & \frac{\langle q_D\rangle_1^R}{C} & 0 & 0 & 0 \\ \frac{\langle q_D\rangle_1^I}{C} & \frac{\langle q_D\rangle_1^I}{C} & \frac{\langle q_D\rangle_1^I}{C} & 0 & 0 & 0 \end{bmatrix} \tag{3.19}$$

$$A_{22}=\begin{bmatrix}
0 & \omega & 0 & 0 & 0 & 0 & \frac{-\langle q_{2,eff}\rangle_0-\langle q_D\rangle_0}{L_1} & 0 & \frac{\langle q_{2,eff}\rangle_0}{L_1} & 0 & \frac{-\langle q_D\rangle_0}{L_1} & 0\\
-\omega & 0 & 0 & 0 & 0 & 0 & 0 & \frac{-\langle q_{2,eff}\rangle_0-\langle q_D\rangle_0}{L_1} & 0 & \frac{\langle q_{2,eff}\rangle_0}{L_1} & 0 & \frac{-\langle q_D\rangle_0}{L_1}\\
0 & 0 & 0 & \omega & 0 & 0 & \frac{\langle q_1\rangle_0}{L_2} & 0 & \frac{-\langle q_1\rangle_0-\langle q_D\rangle_0}{L_2} & 0 & \frac{-\langle q_D\rangle_0}{L_2} & 0\\
0 & 0 & -\omega & 0 & 0 & 0 & 0 & \frac{\langle q_1\rangle_0}{L_2} & 0 & \frac{-\langle q_1\rangle_0-\langle q_D\rangle_0}{L_2} & 0 & \frac{-\langle q_D\rangle_0}{L_2}\\
0 & 0 & 0 & 0 & 0 & \omega & \frac{\langle q_1\rangle_0}{L} & 0 & \frac{\langle q_{2,eff}\rangle_0}{L} & 0 & \frac{-\langle q_D\rangle_0}{L} & 0\\
0 & 0 & 0 & 0 & -\omega & 0 & 0 & \frac{\langle q_1\rangle_0}{L} & 0 & \frac{\langle q_{2,eff}\rangle_0}{L} & 0 & \frac{-\langle q_D\rangle_0}{L}\\
\frac{1-\langle q_1\rangle_0}{C_1} & 0 & \frac{-\langle q_1\rangle_0}{C_1} & 0 & \frac{-\langle q_1\rangle_0}{C_1} & 0 & 0 & \omega & 0 & 0 & 0 & 0\\
0 & \frac{1-\langle q_1\rangle_0}{C_1} & 0 & \frac{-\langle q_1\rangle_0}{C_1} & 0 & \frac{-\langle q_1\rangle_0}{C_1} & -\omega & 0 & 0 & 0 & 0 & 0\\
\frac{-\langle q_{2,eff}\rangle_0}{C_2} & 0 & \frac{1-\langle q_{2,eff}\rangle_0}{C_2} & 0 & \frac{-\langle q_{2,eff}\rangle_0}{C_2} & 0 & 0 & 0 & 0 & \omega & 0 & 0\\
0 & \frac{-\langle q_{2,eff}\rangle_0}{C_2} & 0 & \frac{1-\langle q_{2,eff}\rangle_0}{C_2} & 0 & \frac{-\langle q_{2,eff}\rangle_0}{C_2} & 0 & 0 & -\omega & 0 & 0 & 0\\
\frac{\langle q_D\rangle_0}{C} & 0 & \frac{\langle q_D\rangle_0}{C} & 0 & \frac{\langle q_D\rangle_0}{C} & 0 & 0 & 0 & 0 & 0 & -\frac{1}{RC} & \omega\\
0 & \frac{\langle q_D\rangle_0}{C} & 0 & \frac{\langle q_D\rangle_0}{C} & 0 & \frac{\langle q_D\rangle_0}{C} & 0 & 0 & 0 & 0 & -\omega & -\frac{1}{RC}
\end{bmatrix}$$

(3.20)

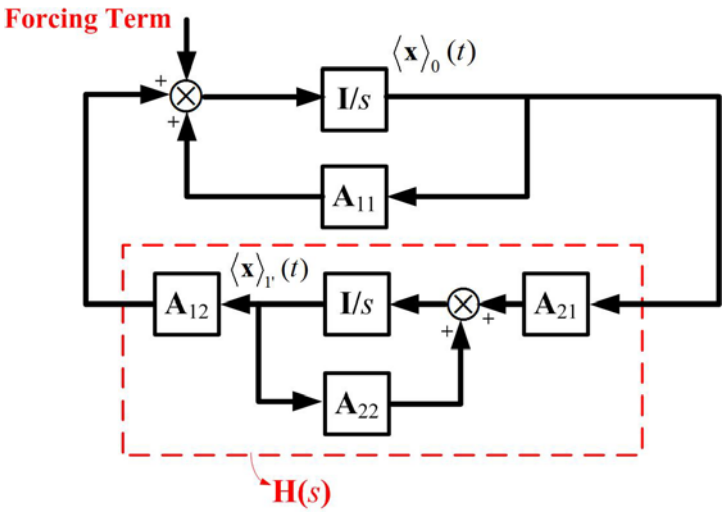

Figure 3.3: An Equivalent Block Diagram of (3.14).

MF Model Order Reduction

Selective modal analysis (SMA) [82] is used to reduce the order of the MF model. The selective modal analysis focuses on the index-0 averages and eliminates higher order averages in a way that leaves the behavior of the index-0 average intact. In SMA framework, the dynamics of the high order harmonics $H(s)$ in Fig. 3.3 is replaced by a

constant M. The constant M is generated by choosing a 6 by 6 matrix $P=[p_1,...,p_6]$— whose columns are the first six coordinates of the eigenvectors that correspond to the six eigenvalues associated with the index-0 averages of A_{MF}. In order to exactly preserve the first six eigenvalues of A_{MF}, the constant matrix M must satisfy

$$M \cdot p_i = H(\lambda_i) \cdot p_i \tag{3.21}$$

where i=1, 2, …, 6. Then, the reduced-order MF (RMF) model, which exactly contains the eigenvalues of A_{MF}'s first six eigenvectors, is given by

$$\frac{d}{dt}\langle \bar{x} \rangle_0 (t) = (A_{11} + M) \cdot \langle \bar{x} \rangle_0 (t) + B \tag{3.22}$$

where $\langle \bar{x} \rangle_0 (t)$ contains the variables of the RMF model, B is a 6 by 1 vector with all terms 0 except the first two are E_1/L_1 and E_2/L_2 , respectively. The derived $A_{11} + M$ matrix contains exactly the same eigenvalues as those six associated with the index-0 averages of A_{MF}; the eigenvectors of $A_{11} + M$ are the same as the first six coordinates of the eigenvectors that correspond to the six eigenvalues associated with the index-0 averages of A_{MF}.

Alternatively, M could be selected as the dc gain of $H(s)$:

$$M = H(0) = -A_{12} A_{22}^{-1} A_{21}. \tag{3.23}$$

The approximation given by (3.23) represents the result of a standard singular perturbation problem [83].

Small-signal Model Derivation

The small-signal model is derived based on the proposed MF model. The state-space form of the small-signal model can be written as

$$\begin{cases} \dot{\tilde{x}} = A_M \tilde{x} + B_{d\_M} \tilde{d} + B_{w\_M} \tilde{w} \\ \tilde{y} = C\tilde{x} \end{cases} \tag{3.24}$$

where $B_{w\_M} = B_w = \begin{bmatrix} \frac{1}{L_1} & 0 & 0 & 0 & 0 & 0 \\ 0 & \frac{1}{L_2} & 0 & 0 & 0 & 0 \\ 0 & 0 & 0 & 0 & 0 & -\frac{1}{C} \end{bmatrix}^T$; the analytical form of B_{d_M} is derived based on the next two equations

$$B_{d\_MF} \cdot \tilde{d}_{MF} = \begin{bmatrix} \frac{X_4+X_6}{L_1} & \frac{X_5+X_6}{L_1} & \frac{2(X_{13}+X_{17})}{L_1} & \frac{2(X_{14}+X_{18})}{L_1} & \frac{2(X_{15}+X_{17})}{L_1} & \frac{2(X_{16}+X_{18})}{L_1} \\ \frac{X_4+X_6}{L_2} & \frac{X_5+X_6}{L_2} & \frac{2(X_{13}+X_{17})}{L_2} & \frac{2(X_{14}+X_{18})}{L_2} & \frac{2(X_{15}+X_{17})}{L_2} & \frac{2(X_{16}+X_{18})}{L_2} \\ \frac{X_4+X_6}{L} & \frac{X_5+X_6}{L} & \frac{2(X_{13}+X_{17})}{L} & \frac{2(X_{14}+X_{18})}{L} & \frac{2(X_{15}+X_{17})}{L} & \frac{2(X_{16}+X_{18})}{L} \\ \frac{-(X_1+X_2+X_3)}{C_1} & 0 & \frac{-2(X_7+X_9+X_{11})}{C_1} & \frac{-2(X_8+X_{10}+X_{12})}{C_1} & 0 & 0 \\ 0 & \frac{-(X_1+X_2+X_3)}{C_2} & 0 & 0 & \frac{-2(X_7+X_9+X_{11})}{C_2} & \frac{-2(X_8+X_{10}+X_{12})}{C_2} \\ \frac{-(X_1+X_2+X_3)}{C} & \frac{-(X_1+X_2+X_3)}{C} & \frac{-2(X_7+X_9+X_{11})}{C} & \frac{-2(X_8+X_{10}+X_{12})}{C} & \frac{-2(X_7+X_9+X_{11})}{C} & \frac{-2(X_8+X_{10}+X_{12})}{C} \\ \frac{X_{13}+X_{17}}{L_1} & \frac{X_{15}+X_{17}}{L_1} & \frac{X_4+X_6}{L_1} & 0 & \frac{X_5+X_6}{L_1} & 0 \\ \frac{X_{14}+X_{18}}{L_1} & \frac{X_{16}+X_{18}}{L_1} & 0 & \frac{X_4+X_6}{L_1} & 0 & \frac{X_5+X_6}{L_1} \\ \frac{X_{13}+X_{17}}{L_2} & \frac{X_{15}+X_{17}}{L_2} & \frac{X_4+X_6}{L_2} & 0 & \frac{X_5+X_6}{L_2} & 0 \\ \frac{X_{14}+X_{18}}{L_2} & \frac{X_{14}+X_{18}}{L_2} & 0 & \frac{X_4+X_6}{L_2} & 0 & \frac{X_5+X_6}{L_2} \\ \frac{X_{13}+X_{17}}{L} & \frac{X_{15}+X_{17}}{L} & \frac{X_4+X_6}{L} & 0 & \frac{X_5+X_6}{L} & 0 \\ \frac{X_{14}+X_{18}}{L} & \frac{X_{14}+X_{18}}{L} & 0 & \frac{X_4+X_6}{L} & 0 & \frac{X_5+X_6}{L} \\ \frac{-(X_7+X_9+X_{11})}{C_1} & 0 & \frac{-(X_1+X_2+X_3)}{C_1} & 0 & 0 & 0 \\ \frac{-(X_8+X_{10}+X_{12})}{C_1} & 0 & 0 & \frac{-(X_1+X_2+X_3)}{C_1} & 0 & 0 \\ 0 & \frac{-(X_7+X_9+X_{11})}{C_2} & 0 & 0 & \frac{-(X_1+X_2+X_3)}{C_2} & 0 \\ 0 & \frac{-(X_8+X_{10}+X_{12})}{C_2} & 0 & 0 & 0 & \frac{-(X_1+X_2+X_3)}{C_2} \\ \frac{-(X_7+X_9+X_{11})}{C} & \frac{-(X_7+X_9+X_{11})}{C} & \frac{-(X_1+X_2+X_3)}{C} & 0 & \frac{-(X_1+X_2+X_3)}{C} & 0 \\ \frac{-(X_8+X_{10}+X_{12})}{C} & \frac{-(X_8+X_{10}+X_{12})}{C} & 0 & \frac{-(X_1+X_2+X_3)}{C} & 0 & \frac{-(X_1+X_2+X_3)}{C} \end{bmatrix} \cdot \begin{bmatrix} \langle \tilde{q}_1 \rangle_0 \\ \langle \tilde{q}_{2,eff} \rangle_0 \\ \langle \tilde{q}_1 \rangle_1^R \\ \langle \tilde{q}_1 \rangle_1^I \\ \langle \tilde{q}_{2,eff} \rangle_1^R \\ \langle \tilde{q}_{2,eff} \rangle_1^I \end{bmatrix} \tag{3.25}$$

$$\tilde{d}_{MF}=\begin{bmatrix}\langle\tilde{q}_1\rangle_0\\ \langle\tilde{q}_{2,eff}\rangle_0\\ \langle\tilde{q}_1\rangle_1^R\\ \langle\tilde{q}_1\rangle_1^I\\ \langle\tilde{q}_{2,eff}\rangle_1^R\\ \langle\tilde{q}_{2,eff}\rangle_1^I\end{bmatrix}=\begin{bmatrix}1 & 0\\ 0 & 1\\ \cos(2\pi D_1) & 0\\ 0 & -\sin(2\pi D_1)\\ -\frac{1}{2}\cos[2\pi(\frac{D_1}{2}+\frac{D_{2,eff}}{2})]+\frac{1}{2}\cos[2\pi(\frac{D_1}{2}+\frac{3D_{2,eff}}{2})] & -\frac{1}{2}\cos[2\pi(\frac{D_1}{2}+\frac{D_{2,eff}}{2})]+\frac{3}{2}\cos[2\pi(\frac{D_1}{2}+\frac{3D_{2,eff}}{2})]\\ -\frac{1}{2}\sin[2\pi(\frac{D_1}{2}+\frac{3D_{2,eff}}{2})]+\frac{1}{2}\cos[2\pi(\frac{D_1}{2}+\frac{D_{2,eff}}{2})] & -\frac{3}{2}\sin[2\pi(\frac{D_1}{2}+\frac{3D_{2,eff}}{2})]+\frac{1}{2}\cos[2\pi(\frac{D_1}{2}+\frac{D_{2,eff}}{2})]\end{bmatrix}\cdot\begin{bmatrix}\tilde{d}_1\\ \tilde{d}_2\end{bmatrix}=M_d\begin{bmatrix}\tilde{d}_1\\ \tilde{d}_2\end{bmatrix}$$

(3.26)

Matrix C in (3.24) can be selected based on the desired plant outputs.

MODELS COMPARISON

Power Budgeting

Consider the MI-SEPIC in Fig. 1.9 with nominal effective duty cycles of both input legs given by D_1=0.30 and $D_{2,eff}$=0.30, E_1=27.9 V, E_2=13.0 V, L_1=L_2=L=150 μH, C_1=C_2=34 μF, C=1500 μF, and R=10 Ω. The switching frequencies in simulations and experiments ensure CCM operation of the MI-SEPIC. Note that (3.14) and (3.18) are known as the MF and RMF model, respectively. The calculated and simulated steady-state current values are listed in Table 3. The absolute values of the current offsets $\|O_1\|$, $\|O_2\|$, and $\|O_3\|$ are also indicated in Table 3. It is demonstrated that the current offsets of the proposed model with respect to the theoretical values are significantly lower than those of the SSA model, thus verifying the accuracy of the modified model. The differences between the experimental results and theoretical calculations are caused by the non-ideal components and internal losses. In addition, a parameter ε can be defined to quantify the error of different models as

$$\varepsilon=\frac{\|I_m-I\|}{\|I\|} \tag{3.27}$$

where I_m = [I_{L1}, I_{L2}, I_L], which represents an EP of the currents. The values of ε under various switching frequencies are also indicated in Table 3. With a switching frequency of 40 kHz the error ε of the SSA model, the MF model and the RMF model are 14.7%,

1.69%, and 1.80%, respectively. Therefore, both the MF and RMF models achieve improved accuracy compared to the SSA model.

	Inductor Currents	I_{L1} [A]	$\|O_1\|$ [A]	I_{L2} [A]	$\|O_2\|$ [A]	I_L [A]	$\|O_3\|$ [A]	ε
20 kHz	Theoretical Value from (3.3)	1.716	NA	3.556	NA	3.068	NA	NA
	SSA	2.301	0.585	2.301	1.255	3.068	0	28.6%
	RMF	1.666	0.05	3.734	0.178	3.099	0.03	3.9%
	MF	1.643	0.073	3.695	0.139	3.064	0.004	3.2%
	Experimental Results (Fig. 3.5 (a))	2.02	NA	3.29	NA	2.90	NA	NA
40 kHz	Theoretical Value from (3.3)	2.008	NA	2.928	NA	3.068	NA	NA
	SSA	2.301	0.293	2.301	0.627	3.068	0	14.8%
	RMF	1.979	0.029	3.007	0.079	3.075	0.007	1.80%
	MF	1.973	0.035	2.999	0.069	3.067	0.001	1.69%
	Experimental Results (Fig. 3.5 (b))	2.05	NA	2.89	NA	2.89	NA	NA
80 kHz	Theoretical Value from (3.3)	2.154	NA	2.615	NA	3.068	NA	NA
	SSA	2.301	0.147	2.301	0.314	3.068	0	7.6%
	RMF	2.139	0.015	2.652	0.037	3.069	0.001	0.87%
	MF	2.137	0.017	2.650	0.035	3.067	0.001	0.85%
	Experimental Results (Fig. 3.5 (c))	2.27	NA	2.75	NA	2.90	NA	NA

Table 3: Steady-State Inductor Currents of an MI-SEPIC with Different Switching Frequencies.

Simulation Verifications

Time domain waveforms were also examined through simulations. Figure 3.4 depicts steady-state behaviors of $i_{L1}(t)$ and $i_{L2}(t)$ for the different models discussed in this dissertation, considering a switching frequency of 20 kHz. For the MF model, the fundamental harmonics of both input currents can be constructed from the simulated results of (3.3). If the fundamental harmonics of the six state variables are superimposed

on their index-0 averages, improved waveforms can be obtained from the MF model, as presented in Fig. 3.4 (a) and (b). By inspecting Table 3 and Fig. 3.4, the steady-state currents of the MF and RMF models verify their respective calculated value. The steady-state input currents predicted by the SSA model significantly deviate from the expected values, as illustrated in Fig. 3.4 (a) and (b). Also, the input current waveforms obtained with the MF model follow adequately, in both magnitude and phase, the switched input current waveforms. Hence, it is demonstrated that the TM switching functions are correctly represented by the MF model. Ripple can be conveniently estimated with the MF model, too. Although the harmonics with orders are higher than one are truncated, the simulation result shows a satisfactory approximation when only fundamental harmonics are considered.

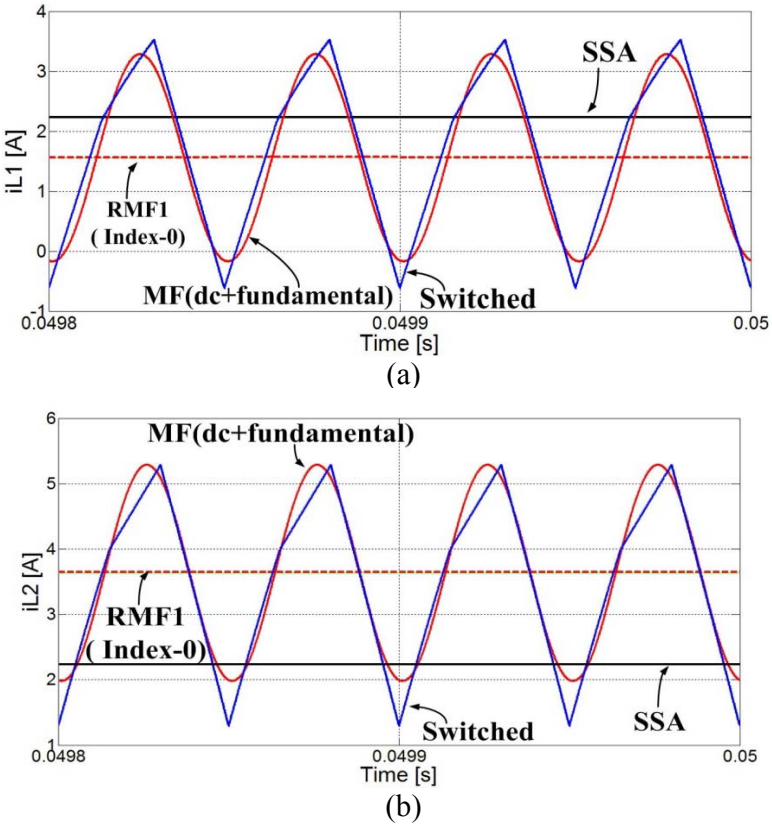

Figure 3.4: Simulations of Input Currents (i_{L1}, i_{L2}) through Different Models.

Experiment Verifications

In order to validate the proposed models, a hardware prototype was built according to Fig. 1.9. The second input leg starts to conduct current only when q_1 switches to zero. Thus, in the experimental results shown in Fig. 3.5, $q_{2,eff} = q_2 - q_1$. The experimental dc values shown in Fig. 3.5 clearly demonstrates that the input currents vary with frequency, although the converter was operating with fixed duty cycles (D_1=0.30 and $D_{2,eff}$=0.30). In addition, I_{L1} and I_{L2} are not equal to each other, which show that the limitation of SSA results in (3.1). For example, with $D_1 = D_{2,eff}$=0.30, I_{L1} and I_{L2} were 2.05 A and 2.89 A, respectively, with a 40 kHz switching frequency. Even with an 80 kHz switching frequency, there was a 0.47 A difference between input currents. Experimental results are also summarized in Table 3, and serve to validate the models and to adequately verify theoretical calculations and simulations.

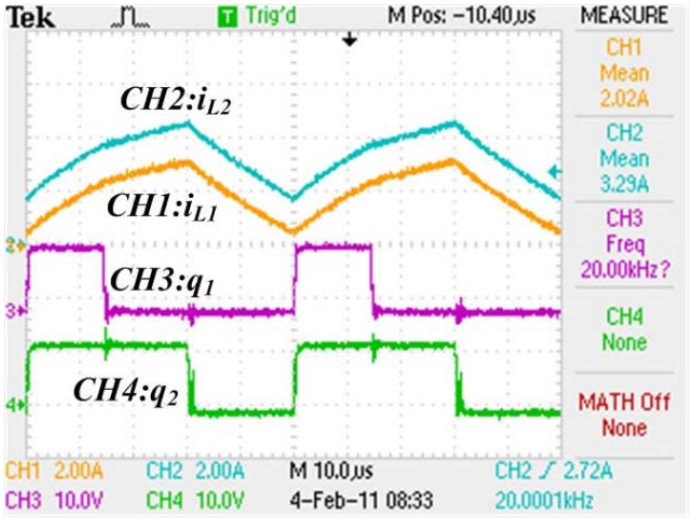

(a)

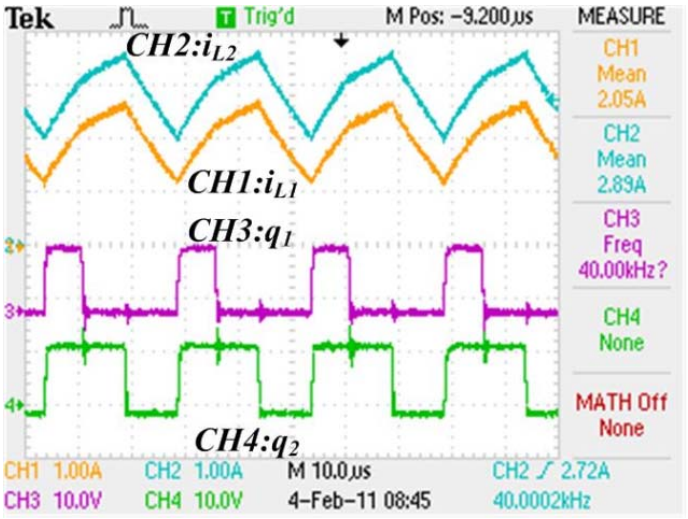

(b)

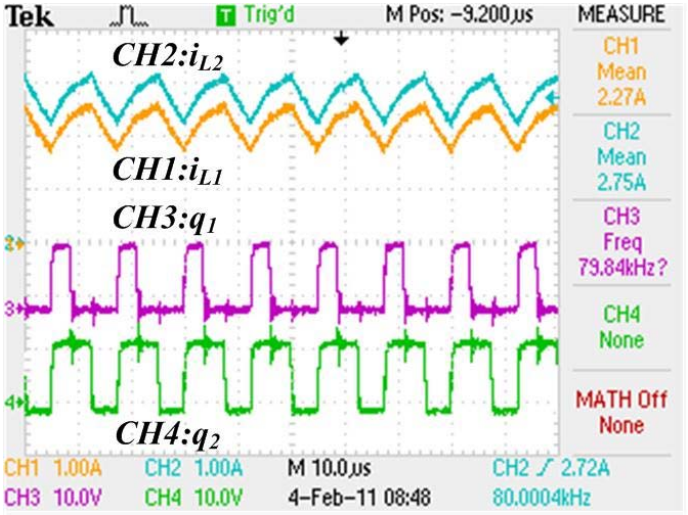

(c)

Figure 3.5: Input Currents Snapshot with Identical Effective Duty Cycles but Different Frequencies.

Chapter 4: Analysis of the Decentralized Control Applied to Multiple-Input Converters

This chapter attempts to apply one of the simplest control scheme—a decentralized controller—to regulate the output (the output voltage and one of the input currents) of an MIC. This chapter proceeds with the focus of whether stability and performance can be achieved by using conventional and modern control design theories. I firstly show the use of the conventional (the Bode plot) to study the stability. Then, through the modern multivariable analysis, this chapter assesses nominal stability, nominal performance, robust stability, and robust performance of the closed-loop system. Due to its many desired characteristics in distributed generation applications, an MI-SEPIC is selected here to motivate the discussion. The analysis is verified with both simulations and prototype-based experiments.

CONTROL OF MULTIPLE-INPUT CONVERTERS

Practically, when used in PV applications, an MI dc-dc converter can often be used to perform both solar panel MPP tracking [84] and output voltage regulation, which calls for a controller to manage both tasks simultaneously. For example, the MI-SEPIC (see Fig. 1.9) could be regulating the current at its input leg #2—it could correspond to the case in which E_2 is the output voltage of a PV module which is controlled to achieve its MPP—while regulating the output voltage with the input leg #1—e.g. E_1 corresponds to the output voltage of another PV module and V_C needs to be regulated to allow the direct connection of a battery string. Most past works on MI converter control consider these converters as an extension of their respective single-input counterpart [18, 39, 85]. However, MI converters are essentially multivariable control systems. Consequently, in this chapter, the power stage of an MI-SEPIC is firstly represented through an MIMO model according to the generalized averaging method [86], which is illustrated in Chapter 3 of this dissertation, and then linearized into an MIMO linear system, whose transfer

function matrix is written as $G_d(s)$ in Fig. 4.1 As a plant with cross-couplings, $G_d(s)$ is not strictly a combination of two SISO systems as it is often considered in MI converters study [35]. A typical representation of the block diagram of the closed-loop system is depicted in Fig. 4.1. $G_w(s)$ is the transfer function matrix from disturbance $\tilde{w}$ to output $\tilde{y}$.

In a multivariable control system, input and output are both vectors and, therefore, both present complicated directionalities. Thus, in contrast to the straightforward representation of the gain of a SISO system, singular values are usually used to quantify the gain and the directionality of a multivariable system [56]. Although many fundamental concepts and techniques involved in the analysis of SISO systems can be extended to the MIMO systems, the latter becomes more complicated caused by the directionality.

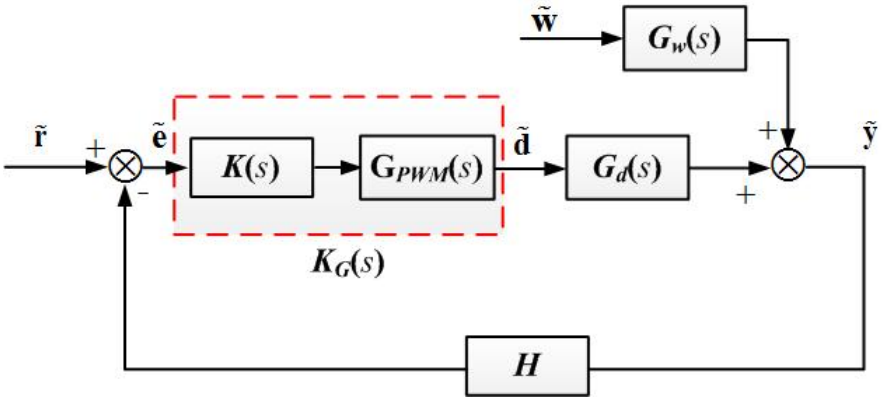

Figure 4.1: Closed-loop System Block Diagram of an MI-SEPIC.

SMALL-SIGNAL MODEL

The state-space form of the small-signal model [74, 87-88] of the MI-SEPIC can be written as

$$\begin{cases} \dot{\tilde{x}} = A\tilde{x} + B\tilde{d} + B_w\tilde{w} \\ \tilde{y} = C\tilde{x} \end{cases} \tag{4.1}$$

where the perturbed state variable deviates from the nominal value is written as $\tilde{x} = [\tilde{i}_{L1} \quad \tilde{i}_{L2} \quad \tilde{i}_L \quad \tilde{v}_{C1} \quad \tilde{v}_{C2} \quad \tilde{v}_C]^T$; $\tilde{d}$, the variations of duty cycles, is the controlled input vector and the vector $\tilde{w}$ represents the low-frequency disturbances. The input $\tilde{d}$ and output variables $\tilde{y}$ in (4.1) are scaled variables as illustrated in [56]. In terms of the scaled variables, the output vector can be written as

$$\tilde{Y}(s) = G_d(s)\tilde{D}(s) + G_w(s)\tilde{W}(s) \tag{4.2}$$

where $G_d(s)$ denotes the transfer function matrix of the plant model and $G_w(s)$ represents the disturbance to output transfer function matrix.

Frequency Domain Analysis

Due to the absence of the D matrix in (4.1), the open-loop control-to-output transfer function matrix is obtained through

$$G_d(s) = C(sI - A)^{-1}B \tag{4.3}$$

from which each particular control-to-output transfer function can be easily obtained as a component of G_d(s). The transfer function matrix given by (4.3) can be written in (4.4):

$$G_d(s) = \begin{bmatrix} G_{11}(s) & G_{12}(s) \\ G_{21}(s) & G_{22}(s) \end{bmatrix} = \frac{1}{J(s)} \begin{bmatrix} N_{11}(s) & N_{12}(s) \\ N_{21}(s) & N_{22}(s) \end{bmatrix}. \tag{4.4}$$

The complete analytical form of G_d(s) can be found in [50]. Equation (4.4) reveals that, due to the off-diagonal terms $G_{12}(s)$ and $G_{21}(s)$, MI converters are essentially multivariable systems. However, before exploring the complicated multivariable analysis, it may be desired to apply conventional SISO techniques first for simplicity. Some of these suitable approaches use a de-coupler or pre-compensator to eliminate loop couplings [56]. This approach requires an exact model of the converter and thus cannot be robust to uncertainties or modeling errors. Another approach, the decentralized control, such as the one schematized in Fig. 4.2, uses a diagonal controller and the controller virtually consists of n SISO controllers. Note that the (static) feedback gain H

is unity in the case of Fig. 4.1 and it can be determined according to implementation convenience in general. Decentralized controllers are widely accepted due to their flexibility, failure tolerance, and simplicity. In light of those merits, this work regulates the MI-SEPIC's output through decentralized control configuration. The implicit assumption in the analysis of decentralized control is that interactions inside multivariable systems are considered as disturbances. Although loop interactions are not removed with a decentralized scheme, performance loss is usually minor [89]. An important step before designing a decentralized controller is to select adequate loop paring that achieves minimum loop interaction. Let's explore this concept with the MI-SEPIC in Fig. 1.9. In this converter, the control objective is to regulate the output voltage (v_{out}) and the input current yielded by the second source (i_{L2}). If the control inputs in the small-signal model are the duty cycles deviations for both input switches, then it is possible to choose two out of the following four input-output pairs: ($\tilde{d}_1$, $\tilde{v}_{out}$) and ($\tilde{d}_2$, $\tilde{i}_{L2}$) or ($\tilde{d}_1$, $\tilde{i}_{L2}$) and ($\tilde{d}_2$, $\tilde{v}_{out}$). The determination of a good loop pairing of the MI-SEPIC is discussed in the next subsection.

The poles and transmission zeros of $G_d(s)$ in (4.4) are presented in Table 4. All the poles have negative real parts, indicating a nominally stable open-loop system. Two of the zeros locate on the right half plane (RHP), which may cause control limitations. Moreover, the steady-state gain matrix $G_d(0)$ is calculated, from which its singular values, condition number and relative gain array (RGA) in steady state are calculated [56, 90-91]. A relative large condition number $\gamma(G_d(0))$ may indicate a problem in control. However, the high value of the condition number is caused by a large singular value $\bar{\sigma}(G_d(0))$ instead of a small $\underline{\sigma}(G_d(0))$. In fact, the minimum singular value $\underline{\sigma}(G_d(0))$ =1.8146, which is larger than 1, indicates an effective control in low frequencies [56]. Moreover, the minimum singular value $\underline{\sigma}(G_d(j\omega))$ is plotted in Fig. 4.3 with respect to frequency. It shows that $\underline{\sigma}(G_d(j\omega))$ stays above 1 up to about 700 rad/s, which is acceptable for steady-state tracking and high-frequency disturbance

rejection. Table 4 shows that $G_w(0)$ contains elements which is larger than 1, so control is necessary to attenuate disturbances.

Poles	Steady state RGA
$-6.2583\times10^{1} \pm j9.5863\times10^{3}$ $-4.6679\times10^{1} \pm j5.5915\times10^{3}$ $-2.6992\times10^{2} \pm j1.0801\times10^{3}$	$\mathrm{RGA}(G_d(0)) = \Lambda(0) = \begin{bmatrix} 2.2016 & -1.2016 \\ -1.2016 & 2.2016 \end{bmatrix}$
Transmission Zeros	**Steady-state gain of disturbance**
$2.5391\times10^{3} \pm j1.9709\times10^{4}$ $-8.6561\times10^{1} \pm j5.7593\times10^{3}$	$G_w(0) = \begin{bmatrix} 3.7093 & 2.2264 & -0.2045 \\ 7.0287 & 3.3359 & 2.2172 \end{bmatrix}$
dc Gain	**Performance RGA (PRGA)**
$G_d(0) = \begin{bmatrix} 14.258 & 10.537 \\ 3.7210 & 5.0381 \end{bmatrix}$	$\Gamma(0) = \begin{bmatrix} 2.2016 & -4.6065 \\ -0.5745 & 2.2016 \end{bmatrix}$
Singular value and condition number	**Closed-loop disturbance gain**
$\bar{\sigma}(G_d(0)) = 35.961$ $\underline{\sigma}(G_d(0)) = 1.8146$ $\gamma(G_d(0)) = 19.818$	$\tilde{G}_w(0) = \begin{bmatrix} 4.9302 & 3.3656 & -10.6591 \\ -0.5838 & -0.5447 & 4.9989 \end{bmatrix}$

Table 4: Frequency Domain Analysis of an Open-loop MI-SEPIC's Small-signal Model.

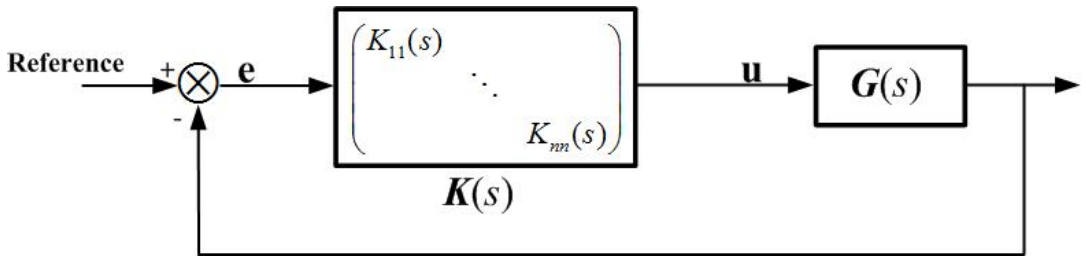

Figure 4.2: A Typical Decentralized Control Scheme for an $n\times n$ System.

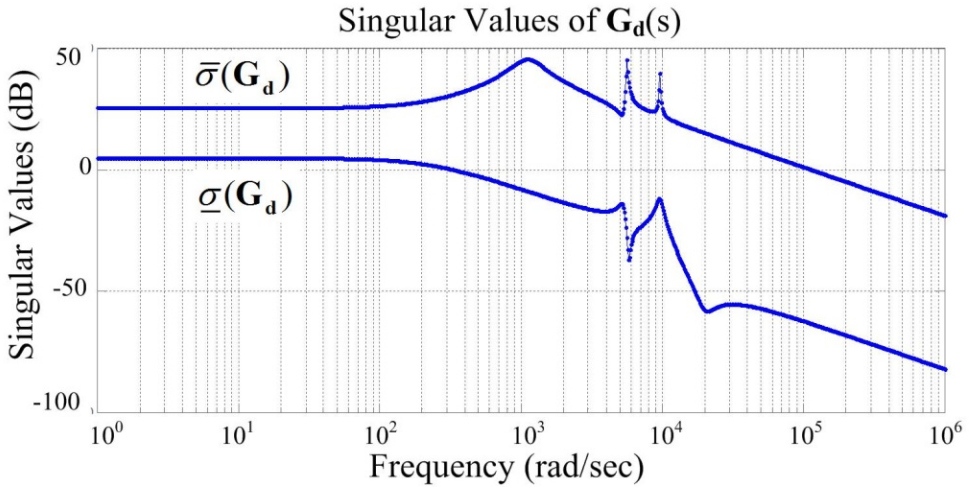

Figure 4.3: Singular Values of the Open-loop Plant $G_d(s)$.

RGA gives important insight into the control properties of a square multivariable system. The steady state RGA matrix indicated in Table 4 demonstrates that a diagonal loop pairing (instead of an off-diagonal one) should be adopted when designing a decentralized controller, according to the paring rule 2 in [56] and [91]. The elements of the RGA matrix are plotted in Fig. 4.4. It reveals a control issue of the MI-SEPIC: at some frequencies, the RGA matrix elements take large magnitudes. Since large RGA implies sensitivity to uncertainty or neglected dynamics, de-couplers or inverse-based controllers are not recommended and a diagonal controller may achieve a conservative performance [56]. Therefore, an open-loop RGA analysis shows the decentralized controller may not be a most ideal choice for the MI-SEPIC. In fact, large RGA is usually observed in time-multiplexing MICs due to strong couplings between inputs [56]. For some other MICs whose RGA stay small over a wide frequency, decent performance may be expected by decentralized controllers.

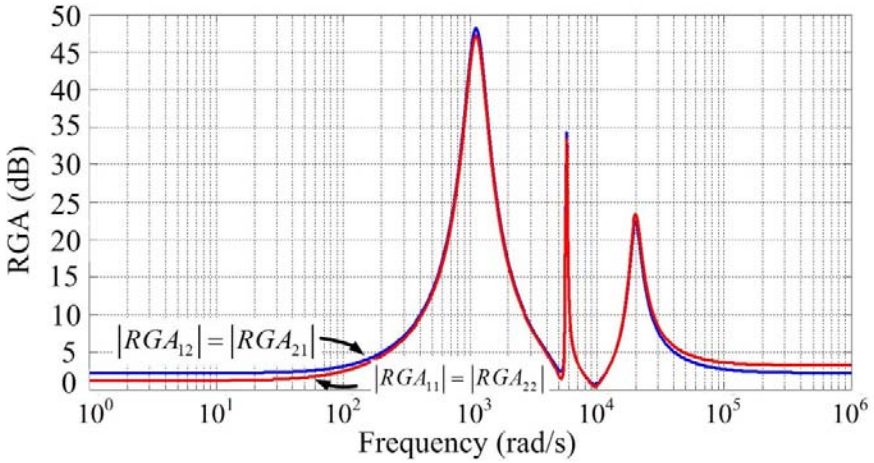

Figure 4.4: Magnitude of RGA of $G_d(s)$.

ANALYSIS OF STABILITY AND PERFORMANCE

PI Gains

In the past, practical MIMO PI controllers with decentralized structure have been proposed in applications different from dc-dc MI converters [86]. As indicated in [92-93], with a decentralized PI control, regulation of all outputs can be achieved if and only if $G_d(s)$ is open-loop stable and $G_d(0)$ is non-singular. In the first section of this chapter, it can be shown that for an MI-SEPIC the origin of $\tilde{x}$ is open-loop stable and $G_d(0)$ is non-singular. Hence, these observations imply that the MI-SEPIC regulation objectives can be achieved through a decentralized PI controller. There are several methods involving decentralized PI controller design for linear multivariable systems, such as the biggest Log-modulus tuning (BLT) method [94], the sequential closing method [95], and the independent design [56]. However, these methods may not be adequate when applied to this case study. Before considering the influences of off-diagonal terms, the detuning method (BLT method) or the independent design method assigns proportional and integral gains of each controller based on corresponding diagonal elements of open-loop transfer function matrix $G_d(s)$. Hence, both methods require that the diagonal terms of $G_d(s)$ lead to a stable PI controller. The simple BLT method is an ideal tool to design the

gains for a decentralized PID controller. Yet, this method failed in the case of the MI-SEPIC due to the failure of the Ziegler-Nichols method. Moreover, additional limitations exist for the independent design method because it is desired to have a diagonal dominant matrix $G_d(s)$ [56]. However, in this case of MI-SEPIC, the system presented by (4.4) would not satisfy the requirements demanded by the BLT method and independent design. Furthermore, in order to achieve time-decoupled outputs the sequential closing method requires the response of one output considerably faster than the other. However, significant difference between output responses is not ensured in the proposed MI-SEPIC either.

One alternative for the analysis is to follow an Individual Channel Design (ICD) approach [96]. ICD is an analysis framework related to decentralized controllers. Since the decentralized can only be applied to square plants, the ICD requires the same number of inputs and outputs [94]. Unlike the decoupling techniques such as the sequential closing method, in the ICD framework, some classical linear SISO system analysis tools, such as Bode or Nyquist criterion, can be applied directly in a multivariable control system. In ICD, a channel Ch*i* is defined by a paring between an input and an output [94, 97-98]. Therefore, according to the ICD, a MIMO system can be equivalently decomposed several SISO systems [94, 97-98]. Consider the transmission from the first input (or the first reference signal) $\tilde{V}_{out\_ref}(s)$ to output $\tilde{V}_{out}(s)$ shown in Fig. 4.5. As described in Fig. 4.5, the duty ratio deviation associated with Q_1, $\tilde{D}_1(s)$, forks to two paths. The first path flows via $G_{11}(s)$; the other one flows through $G_{21}(s)$, $-G_b(s)$, and eventually $G_{12}(s)$. Additionally, a "disturbance" generated by the current reference signal $\tilde{I}_{L2\_ref}(s)$ acts on the output $\tilde{V}_{out}(s)$. With the feedback $H_1(s)$ removed, Fig. 4.5 illustrates Ch1 between $\tilde{V}_{out\_ref}(s)$ and $\tilde{V}_{out}(s)$ with a cross-reference disturbance on $\tilde{V}_{out}(s)$.

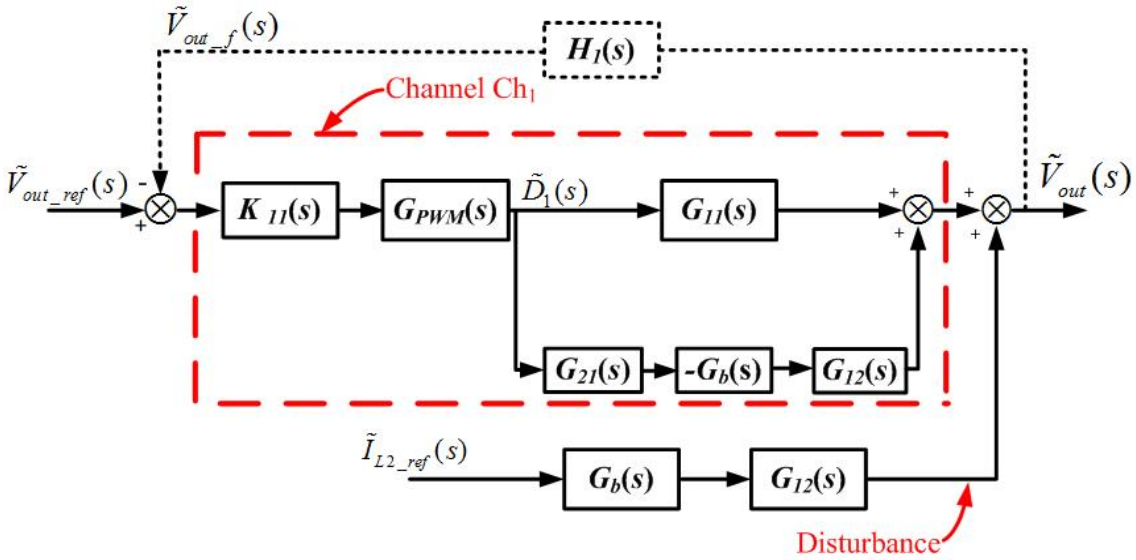

Figure 4.5: Individual Channel Ch1 with Disturbance [99].

Figure 4.1 shows the scheme of the decentralized PI control for an MI-SEPIC. The scaling coefficient of the PWM modulator $G_{PWM}(s)$ is 1/3.3 because the peak of its saw-tooth carrier wave is 3.3 V. The gains of the voltage sensor and current sensor are $H_1(s) = 1/21$ and $H_2(s) = 0.4$, respectively. Based on the individual channel analysis, the open-loop transfer function of the voltage channel is written as [99]:

$$GH_{v_{out}}(s) = K_{11}(s) \cdot G_{PWM}(s) \cdot [G_{11}(s) - G_{21}(s) \cdot G_b(s) \cdot G_{12}(s)] \cdot H_1(s) \qquad (4.5)$$

where

$$G_b(s) = \frac{K_{22}(s) \cdot G_{PWM}(s) \cdot H_2(s)}{1 + K_{22}(s) \cdot G_{PWM}(s) \cdot H_2(s) \cdot G_{22}(s)}. \qquad (4.6)$$

Similarly, the transfer function of the other loop is given by

$$GH_{i_{L2}}(s) = K_{22}(s) \cdot G_{PWM}(s) \cdot [G_{22}(s) - G_{21}(s) \cdot G_a(s) \cdot G_{12}(s)] \cdot H_2(s) \qquad (4.7)$$

where

$$G_a(s) = \frac{K_{11}(s) \cdot G_{PWM}(s) \cdot H_1(s)}{1 + K_{11}(s) \cdot G_{PWM}(s) \cdot H_1(s) \cdot G_{11}(s)}. \qquad (4.8)$$

Equations (4.5) and (4.7) show that either loop gain depends on the other loop regulator gain.

Since this work does not focus on the tuning of the controller, I avoided to use the complicated approaches in but attempted to achieve satisfactory behavior with some iterative process to have both PI controllers operable. I refer the readers to use methods in [94, 97-98] if a rigorous design is needed when the BLT method is unsuccessful. The first step leads to a initial tetrad of controller gains $(K_{p1}, K_{i1}, K_{p2}, K_{i2})^T$ by ignoring the off-diagonal terms of $G_d(s)$ and performing the conventional PI controller tuning twice (in this case the internal model control approach indicated in [100] is used). However, the $G_d(s)$ with interactions may not be stabilized by the initial PI controller. Therefore, the next step in design is the evaluation of the nominal stability of the closed-loop system through transfer functions (of its channels) in (4.5) and (4.7). The next step is to select new gains tetrad within the neighborhood of the initial gain and verify the nominal stability. Since the open-loop stability of the MI-SEPIC and the non-singularity of $G_d(0)$ have been verified, at least one successful tetrad is guaranteed. Our observation is that most of the tetrads are found to be able to achieve closed-loop stability. Finally, I choose the tetrad of PI controller gains with the largest phase margins from all the successful tetrads. The final result is that, k_{p1}=1 and k_{i1}=300 for the voltage regulation, and k_{p2}=5 and k_{i2}=300 for the current regulation.

Stability Analysis Using a SISO Tool

The bode diagrams of (4.5) and (4.7) are plotted by Matlab. Through Figs. 4.6 and 2.12, good matches are observed between the theoretical analysis and the circuit-oriented simulation. Hence, from an ICD perspective, loop couplings are well considered and true behavior of the MIMO system is reflected. Figures 4.6 and 4.7 demonstrate that the crossover frequency is 19 Hz with a phase margin of 60° for the voltage loop and that the crossover frequency is 11.1 kHz with a phase margin of 88° for the current loop.

According to classical Bode stability criteria [101], the phase margins show that, despite the presences of considerable interactions between loops, both input-output channels of closed-loop MI-SEPIC are stable. Thus, the EP of the MI-SEPIC is nominally stable under the proposed decentralized PI control. Furthermore, the large values of the phase margin indicate the robustness and good performance of the decentralized PI controller.

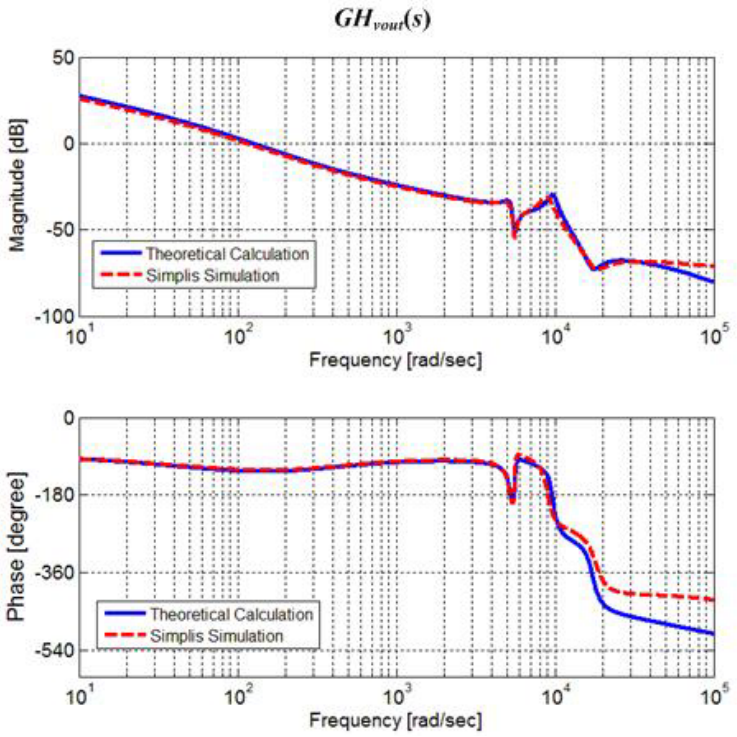

Figure 4.6: Bode Diagram of $GH_{v_{out}}(s)$.

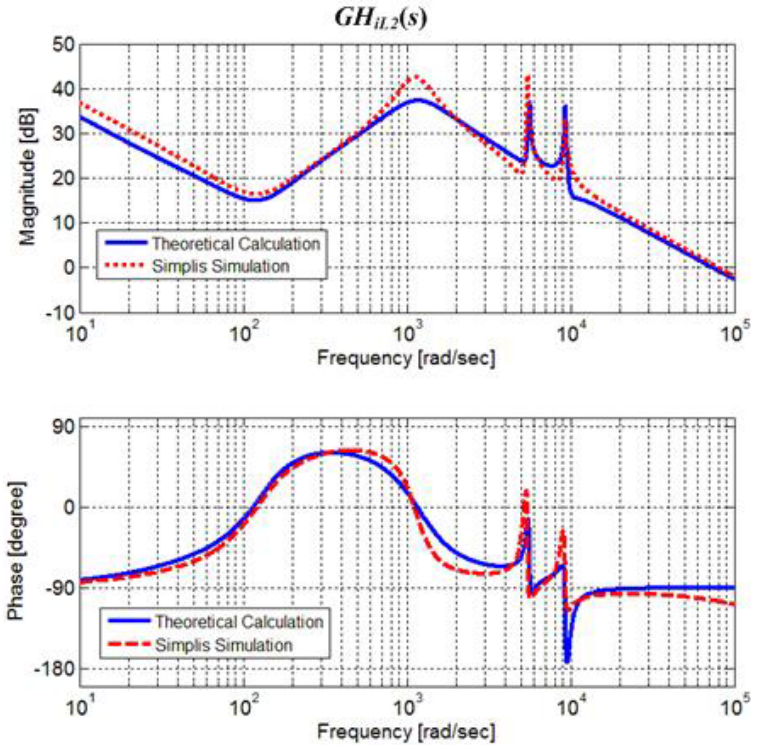

Figure 4.7: Bode Diagram of $GH_{i_{L2}}(s)$.

Nominal Stability and Nominal Performance

Throughout this subsection, the loop is closed as indicated in Fig. 4.1. The gains of the PI controller were configured as k_{p1}=1 and k_{i1}=300 for the voltage loop, and k_{p2}=5 and k_{i2}=300 for the current loop. As part of the analysis and in order to interconnect the matrices and systems in Fig. 4.1, the MATLAB was used (command "sysic"). It is found that the poles have negative real parts. Thus, the nominal stability is achieved by the decentralized PI control. Figure 4.8 shows the sensitivity function singular values. This figure indicates that the bandwidth of the closed-loop system is about 60 rad/s. Note that Fig. 4.8 shows that a desired low gain of $\underline{\sigma}(S)$ was obtained. In addition, the undesirable direction corresponding to the largest singular value of sensitivity plays a dominant role, which indicates that the H_∞ norm is an adequate performance index of the closed-loop MI-SEPIC with decentralized PI controller.

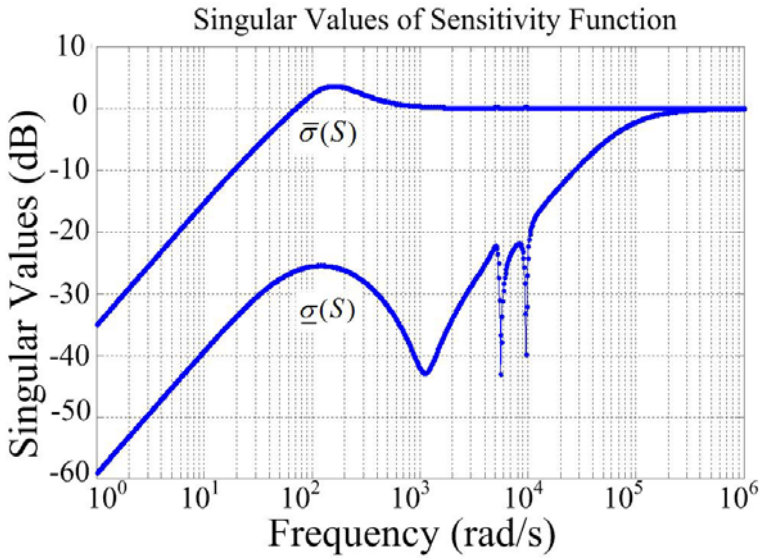

Figure 4.8: Singular Values of Sensitivity Function.

Let $L_i = g_{ii}k_i$ denote the loop transfer function of loop i (i=1, 2), and $\tilde{g}_{d\_ik}$ denote the closed-loop disturbance gains. The condition of acceptable disturbance ($|\tilde{y}_i - \tilde{r}_i| < 1$ for each loop) rejection is given by

$$|1 + L_i| > \max_{k,j} \left\{ \left| \tilde{g}_{d\_ik} \right|, \left| \gamma_{ij} \right| \right\} \tag{4.9}$$

Figure 4.9 shows that the condition in (4.9) is satisfied for the frequencies up to the closed-loop bandwidth, which for a MIMO system is the frequency where $\bar{\sigma}(S)$ cross a gain magnitude of 0.707 from below [56]. Thus, although large RGA values are present, the nominal performance ($|e_i(jw)| < 1$, where $e_i = \tilde{y}_i - \tilde{r}_i$, is the error of the i-th loop) of the closed-loop MI-SEPIC is achieved by a decentralized PI controller.

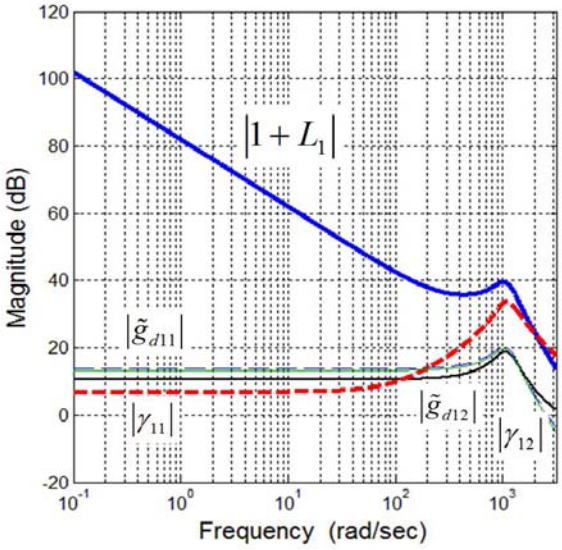

(a)

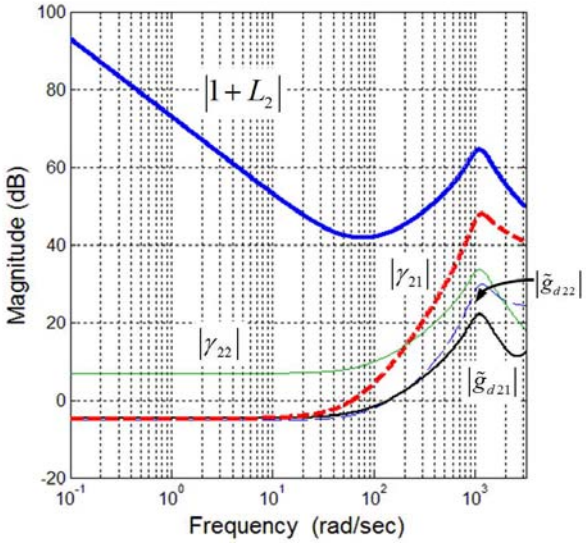

(b)

Figure 4.9: Nominal Performance Analysis.

Robust Stability and Robust Performance

Practically, the duty ratios of an MIC always vary, due to disturbances, changes in references or parameters. Thus, unlike in a linear time-invariant systems, duty cycle variations introduce uncertainties to the *A* matrix. In particular, in the case of the MI-

SEPIC, large variations of effective duty ratios are usually needed to regulate one or all the input currents. In this section, the $M\Delta$-structure (Fig. 4.9) is derived considering uncertainties caused by the varying duty cycles. All the other component parameters are considered constant. Assume that both effective duties can vary between 0.2 and 0.4. According to the analytical form of the *A*, *B*, *C* matrices in (4.4), *A* matrix is affected by the variations of duty ratios in a direct way. Since the unregulated input current is the only state variable that varies with the duty ratios, I assume the perturbations of duty ratios do not give rise to variation of *B* matrix. *C* matrix stays constant regardless of the duty ratio perturbations. Now, the objective in this subsection is to analyze the robust stability and robust performance of the closed-loop system with perturbations of duty ratios by using the structured singular value μ. μ is defined in (4.10):

$$\mu(M) = \frac{1}{\min \Delta \left\{ \bar{\sigma} \middle| \det(I - M\Delta) = 0 \right\}}. \tag{4.10}$$

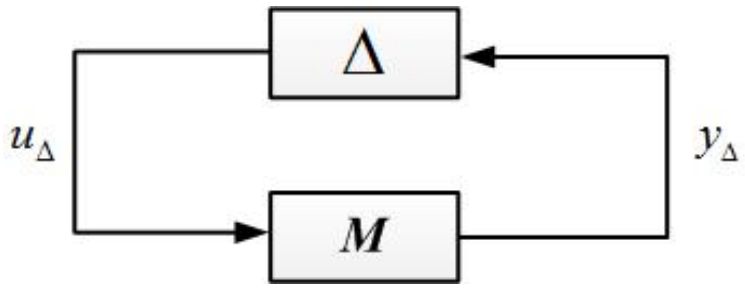

Figure 4.10: The $M\Delta$ Structure.

To calculate μ, the $M\Delta$ formulation procedure presented in [56] was followed. It worth noting on the uncertainty representation that I found the perturbations of duty ratios have to be repeated, that is I need to select the Δ in the following form to apply the uncertain analysis presented in [102]:

$$\Delta = diag\left\{ \Delta_{D_1} \quad \Delta_{D_{2,eff}} \quad \Delta_{D_1} \quad \Delta_{D_{2,eff}} \right\}. \tag{4.11}$$

The block diagram in Fig. 4.11 shows the small-signal model of the MI-SEPIC with uncertainty from the duty cycle perturbations, where W_w, W_r are scaling matrices for disturbance and reference; Some relevant matrices in Fig. 4.11 are written as follows

$$A_{\Delta}^{T} = \begin{bmatrix} 1 & 1 & 1 & 0 & 0 & 0 \\ 1 & 1 & 1 & 0 & 0 & 0 \\ 0 & 0 & 0 & 1 & 0 & 1 \\ 0 & 0 & 0 & 0 & 1 & 1 \end{bmatrix}$$

$$C_{\Delta} = \begin{bmatrix} 0 & 0 & 0 & 0.1 & 0 & 0.1 \\ 0 & 0 & 0 & 0 & 0.1 & 0.1 \\ -0.1 & -0.1 & -0.1 & 0 & 0 & 0 \\ -0.1 & -0.1 & -0.1 & 0 & 0 & 0 \end{bmatrix}$$

$$F^{-1} = diag\left\{ \frac{1}{L_1} \quad \frac{1}{L_2} \quad \frac{1}{L} \quad \frac{1}{C_1} \quad \frac{1}{C_2} \quad \frac{1}{C} \right\}.$$

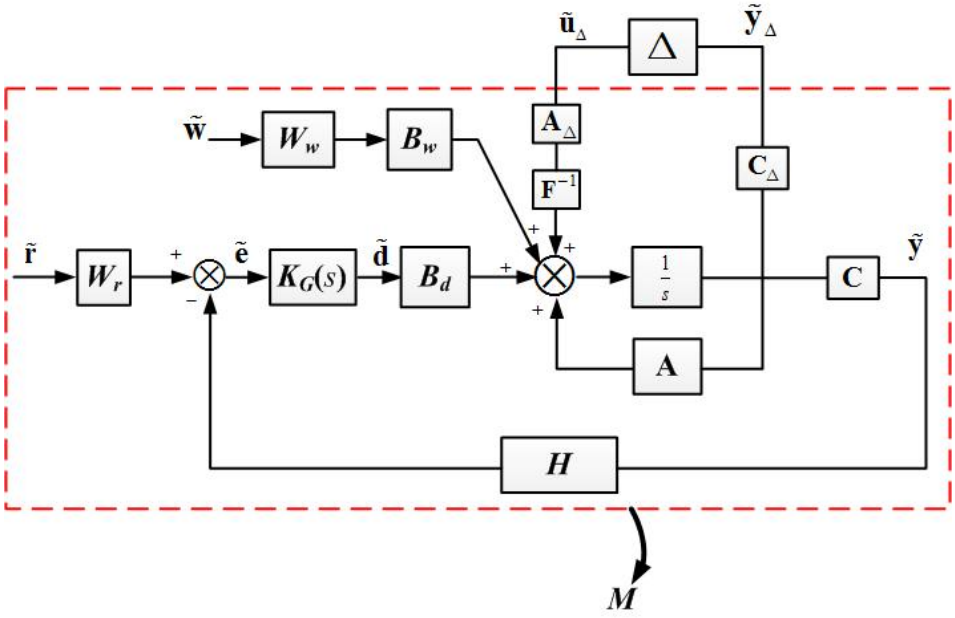

Figure 4.11: Block Diagram of MI-SEPIC with Uncertainty from Perturbed Duty Ratios.

Robust Stability

Condition for the robust stability can be written in (4.12):

$$\text{Robust Stability} \Leftrightarrow \mu_{\Delta}(M) < 1,\ \forall \omega,\ \forall \left\|\Delta\right\|_{\infty} \leq 1. \tag{4.12}$$

Condition in (4.12) is satisfied because $\mu_{\Delta}(M) = 0.6779$. Hence, for all disturbances that satisfy $\left\|\Delta\right\|_{\infty} \leq 1$, the closed-loop system is stable.

Robust Performance

Condition for the robust performance can be written in (4.13):

$$\text{Robust Performance} \Leftrightarrow \left\|F_u(N,\Delta)\right\|_{\infty} < 1,\ \forall \left\|\Delta\right\|_{\infty} \leq 1. \tag{4.13}$$

The robust performance criterion $\left\|F_u(N,\Delta)\right\|_{\infty} < 1$ is not satisfied since $\left\|F_u(N,\Delta)\right\|_{\infty} = 1.8274$ at the frequency 8,577 rad/s. The performance specifications of are not met for all plants in the uncertainty set. Therefore, it shows that the small error $\left|e_i(j\omega)\right| < 1$ cannot be guaranteed for all possible uncertainties. However, the largest gain of $F_u(N,\Delta)$ occurs at the frequency of 8,577 rad/s, which is much higher than the bandwidth. If only low-frequency disturbances are considered, it is still possible to achieve robust performance, which is actually verified through experimental results (with a dc disturbance). Still, this outcome of the robust performance criterion is not a critical issue and it is even expected for most PID controllers because the H_{∞} norm considers a "worst" condition based on frequency and input direction.

SIMULATIONS AND EXPERIMENTAL VERIFICATIONS

System response of an MI-SEPIC shown in Fig. 1.9 was explored while regulating the current at the input leg #2 with its respective switch and the output voltage with switch at the input leg #1 with decentralized PI regulators through simulations and prototype tests. The nominal parameters used are E_1=27.9 V, E_2=13.0 V, L_1=L_2=L=320 μH, C_1=C_2=34 μF, and C=1500 μF. The selected switching frequencies in simulations and experiments ensure CCM operation of the MI-SEPIC. The control configuration implemented in simulation in described in Fig. 4.12.

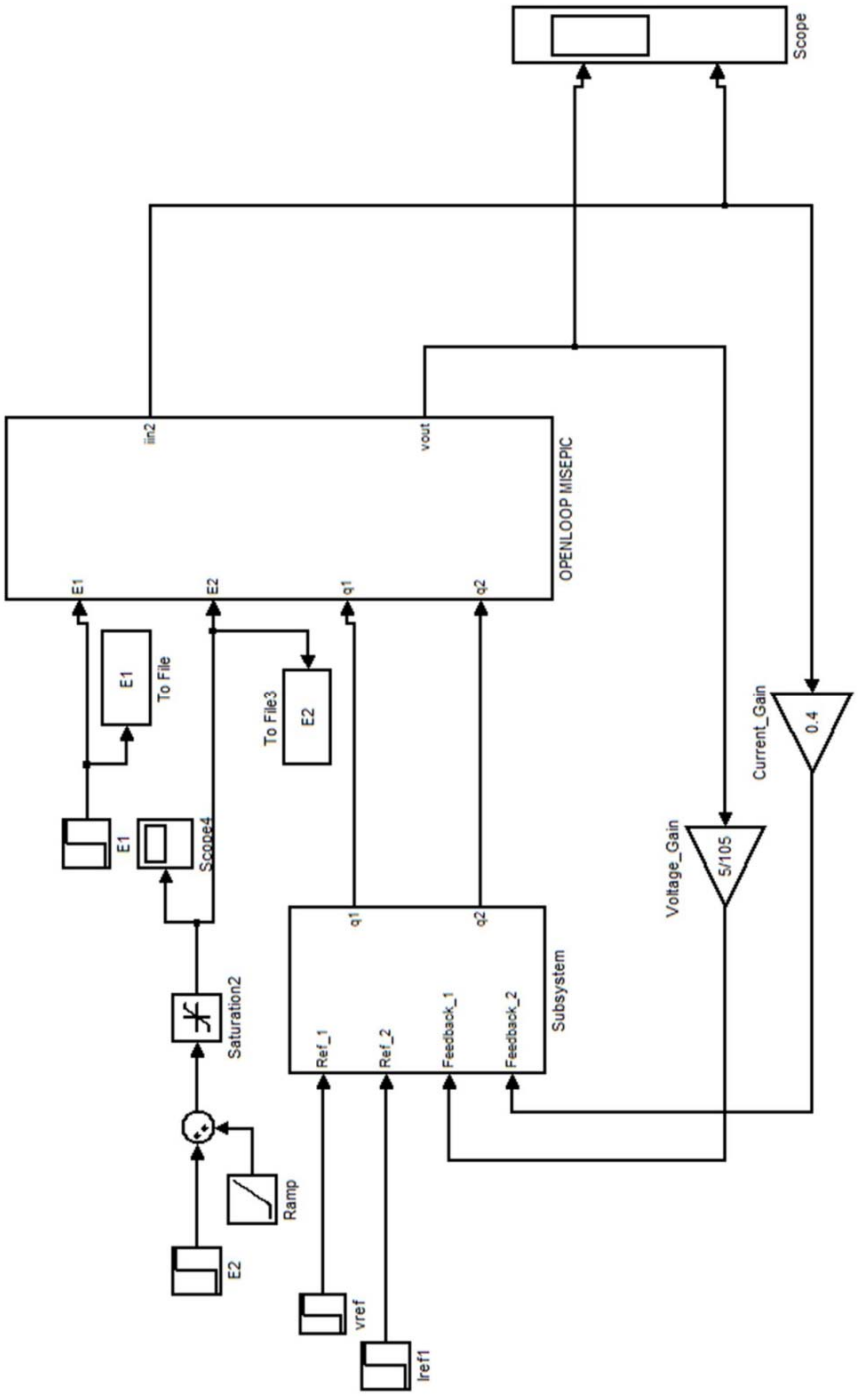

Figure 4.12: The Closed-loop Simulation Scheme for Fig. 4.13.

The gains of both PI controllers were configured based on the previous stability analysis. As simulation results presented by Fig. 4.13 suggest, through a simple

decentralized PI control scheme, the proposed MI-SEPIC is able to successfully perform line and load regulation for both targets (voltage and current) simultaneously, despite of the described potential duty cycle control limitations and loop interactions.

Experimental test on load and line regulation used the same PI controllers and parameters as in the simulations. Reference values for V_{out} and I_{L2} are 30.0 V and 1.0 A, respectively. Figure 4.14 (a)-(d) show the experimental verification of line regulation corresponding to Fig. 4.13 (a)-(d). Figure 4.14 (e) shows the regulation when the load decreases from 25 Ω to 35 Ω, verifying Fig. 4.13 (e). As it is shown, v_{out} and i_{L2} are regulated precisely. The current in the output inductor i_L was measured and, as expected, it stays constant at 1.2 A because it only depends on v_{out} and R in the MI-SEPIC. Despite the described potential duty cycle control limitations and loop interactions, these simulated and experimental results for closed-loop MI-SEPIC—depicted in Fig. 4.13 and Fig. 4.14—suggest that with a simple decentralized PI control scheme, the proposed MI-SEPIC is able to successfully perform line and load regulation for both targets (voltage and current) simultaneously. Both simulation and experimental results show that the disturbances related with output current variations are difficult to be rejected (long transient), which can be confirmed by the large components corresponding to $\tilde{i}_{out}$ in steady-state closed-loop disturbance gain in Table 4. This difficulty can also be explained by the relatively small bandwidth of the closed-loop system. In addition, both simulation and experimental results demonstrate that, under the given dc disturbance and corresponding uncertainty, robust stability and performance is achieved by the closed-loop MI-SEPIC.

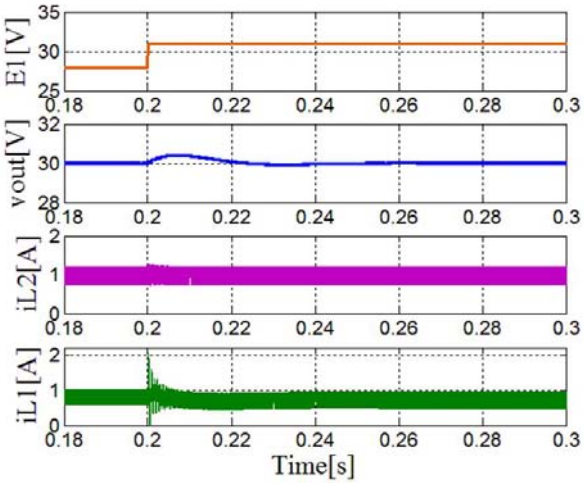
E1[V]
vout[V]
iL2[A]
iL1[A]
Time[s]

(a)

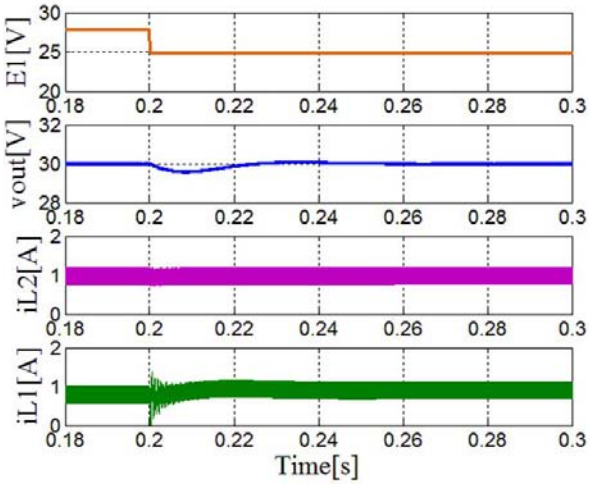
E1[V]
vout[V]
iL2[A]
iL1[A]
Time[s]

(b)

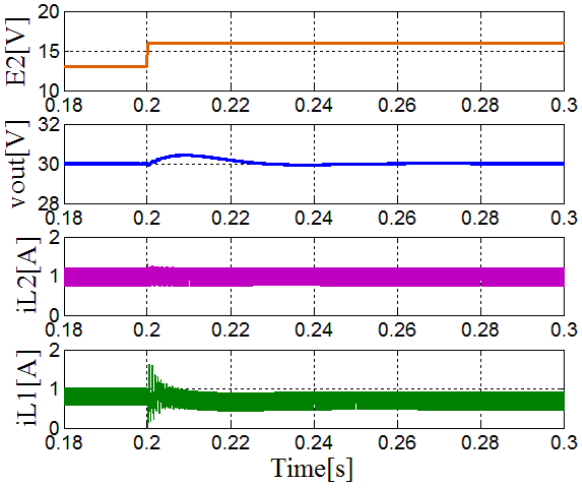
E2[V]
vout[V]
iL2[A]
iL1[A]
Time[s]

(c)

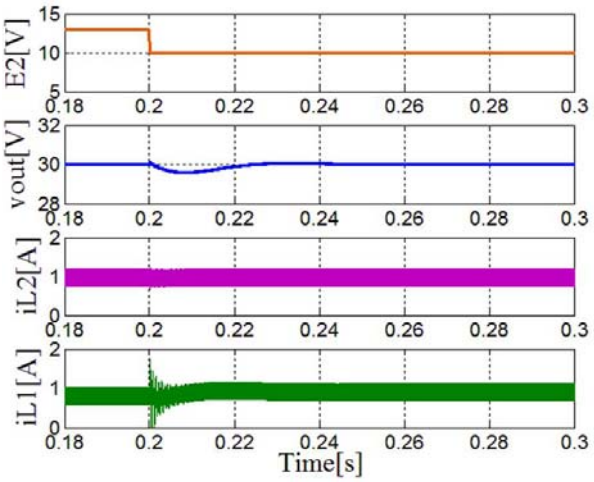

(d)

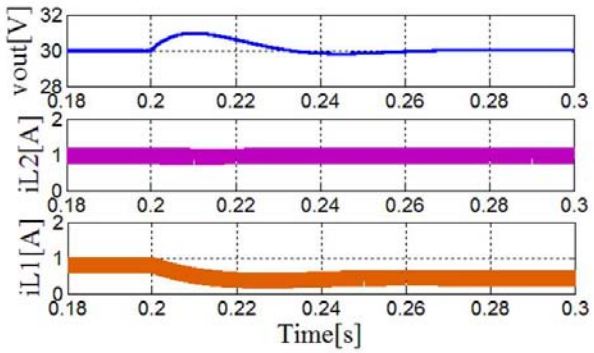

(e)

Figure 4.13: Simulated Closed-loop Response under Step Disturbances. (a) Simulated Responses of v_{out} and i_{L2} when E_1 Increases Suddenly. (b) Simulated Responses of v_{out} and i_{L2} when E_1 Decreases Suddenly. (c) Simulated Responses of v_{out} and i_{L2} when E_2 Increases Suddenly. (d) Simulated Responses of v_{out} when E_2 Decreases Suddenly. (e) Simulated Response of i_{L1}, i_{L2}, and v_{out} when the Load Changes Suddenly.

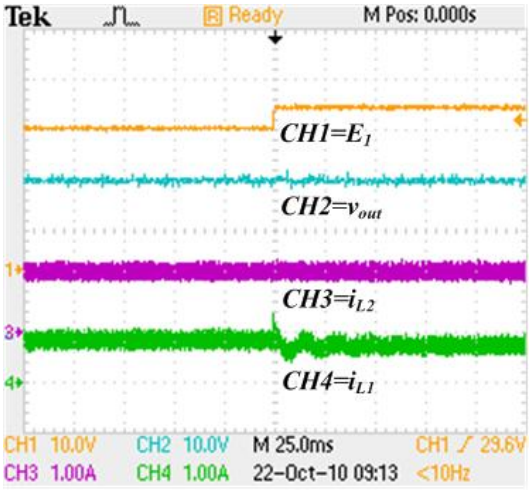
Tek
Ready
M Pos: 0.000s
CH1=E1
CH2=vout
CH3=iL2
CH4=iL1
CH1 10.0V
CH2 10.0V
M 25.0ms
CH1 29.6V
CH3 1.00A
CH4 1.00A
22-Oct-10 09:13
<10Hz

(a)

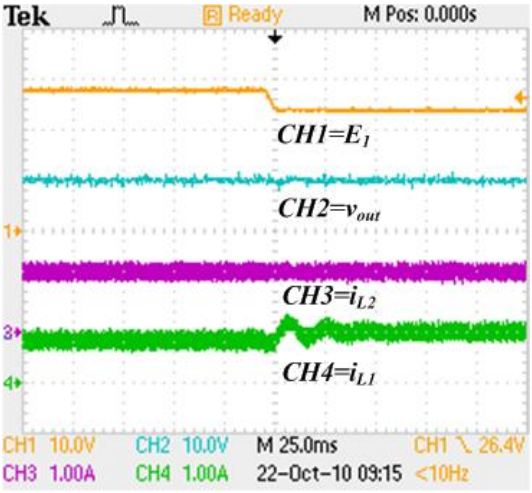
Tek
Ready
M Pos: 0.000s
CH1=E1
CH2=vout
CH3=iL2
CH4=iL1
CH1 10.0V
CH2 10.0V
M 25.0ms
CH1 26.4V
CH3 1.00A
CH4 1.00A
22-Oct-10 09:15
<10Hz

(b)

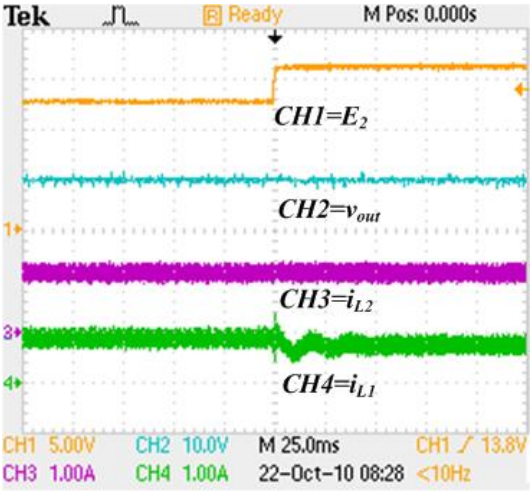
Tek
Ready
M Pos: 0.000s
CH1=E2
CH2=vout
CH3=iL2
CH4=iL1
CH1 5.00V
CH2 10.0V
M 25.0ms
CH1 13.8V
CH3 1.00A
CH4 1.00A
22-Oct-10 08:28
<10Hz

(c)

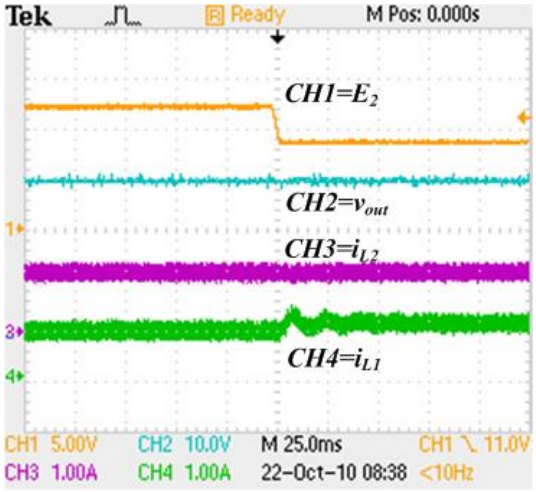

(d)

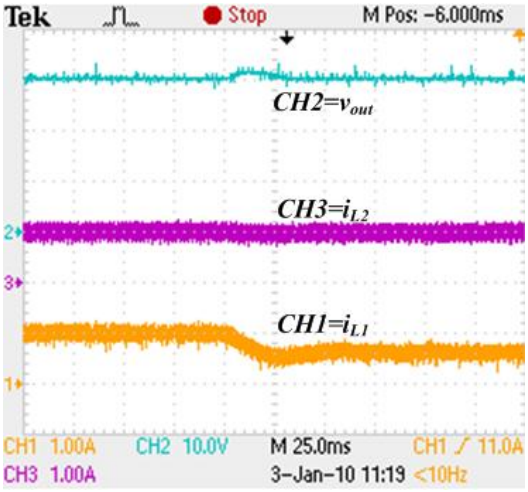

(e)

Figure 4.14: Experimental Closed-loop Response under Step Disturbances. (a) Experimental Result of v_{out} and i_{L2} when E_1 Increases Suddenly. (b) Experimental Result of v_{out} and i_{L2} when E_1 Decreases Suddenly. (c) Experimental Result of v_{out} and i_{L2} when E_2 Increases Suddenly. (d) Experimental Result of v_{out} when E_2 Decreases Suddenly. (e) Experimental Result of i_{L1}, i_{L2}, and v_{out} when the Load Changes Suddenly.

Chapter 5: Multivariable Control Design and Synthesis of Multiple-input-multiple-output Converters

Overview of Control on MIMO Power Converters Applied to Renewable Energy Applications

Autonomous Control

The power flow in a dc micro-grid can be achieved either through a central control [103] or an autonomous control [104]. One of the main disadvantages of the central control architecture is its poor reliability due to communication delay or even failure [105]. In an autonomously controlled micro-grid system, each part takes control actions according to local voltage or current detection. Due to the absence of a common communication link (which may become a single point of failure) among all parts, the autonomous control may achieve a highly-available system [13]. In this chapter, I study the autonomous control for a MIMO converter in a dc distribution system. Therefore, every current or voltage becomes local information that can be measured for control implementation.

Control of Multivariable Plants

Controllers for multivariable plants can be separated into two categories: decentralized controllers and multivariable controllers [56]. A decentralized controller, which consists of several SISO controllers, can be applied to regulate an MIC's output [23, 35]. A multivariable control approach differs from a decentralized control method in the following four ways. First, a decentralized controller can only be applied to a square plant while a multivariable controller can be applied to both square and non-square systems. Second, in a decentralized control, multivariable interactions are treated as disturbances [57]. Consequently, the decentralized control approximates a MIMO system with multiple independent SISO systems. Still, interactions in a MIMO system are not neglected or approximated in a multivariable control approach. Third, a decentralized

controller usually causes performance loss and even unstable behaviors because multivariable interactions are not compensated [56]. For example, in [99], I implemented a decentralized controller on a multiple-input SEPIC and through an uncertainty analysis found its potential performance limitations. Therefore, a decentralized control is usually implemented for an acceptable closed-loop behavior. On the other hand, since interactions are not neglected, improved robust stability and performance can be achieved through a multivariable controller, for example, an H_∞ controller [106]. Fourth, although a decentralized controller can be designed by exploiting SISO design tools [57], to the best of our knowledge there is no general framework for a decentralized controller design that allows for disturbance-attenuation and robustness. Yet, disturbance-attenuation and robustness can be achieved in the design process of a multivariable controller. Therefore, in spite of its simplicity, decentralized controllers are ruled out in this work due to these essential limitations when compared with multivariable controllers. Our aim is to find a general framework which accomplishes the multivariable controller design and synthesis for a MIMO converter.

H_∞ Control on Power Electronics

Many researchers implement H_∞ controllers on SISO power converters [107-109] to minimize output impedance. However, these studies [107-109] assume a linear time-invariant (LTI) model. Consequently, the controllers therein require perfect knowledge of components' value and do not guarantee the stability except at the nominal operating points. Recently, robust H_∞ controllers that achieve quadratic stability and H_∞ performance based on the linear matrix inequality (LMI) [110] has been applied to a buck converter [111] and a boost converter [112]. However, the effort involved in H_∞ controller design and implementation may not be justifiable in SISO systems as it is in MIMO systems because parameter uncertainty in SISO systems is generally less complicated than that in MIMO systems [56]. In addition, the gain of the H_∞ controller

in second order SISO systems (buck [111], boost [107-108, 112], and buck-boost converter [109]) may be limited because PID controllers usually provide acceptable performance for first or second order systems [113].

In the past, controller design and synthesis of MIMO converters (or MICs) has not been systematically studied other than using conventional approaches suitable for SISO systems. To address this gap, this work studies the control design and synthesis of a MIMO converter, in which the effect of disturbances and uncertainties are essential issues to address [56]. H_∞ control provides a direct framework to optimize the infinity norm between exogenous disturbances and outputs [56, 106] and suppresses the response of disturbances. It is well-known that H_∞ control also guarantees performance requirement under dynamic uncertainties [114-115]. Thus, in contrast to SISO systems, the H_∞ approach becomes a prevalent method for multivariable controller design, as exemplified in [116]. However, the standard H_∞ control [115] does not ensure closed-loop stability or H_∞ performance in the presence of parametric uncertainties [117]. A number of works delve into robust H_∞ controller design which robustly stabilize uncertain systems while satisfies the H_∞ norm constraint for all allowable parametric uncertainties [117-119]. Results in [120] show that such a controller design problem can be converted to an LMI problem. One of the advantages of the LMI-based approach is that it allows avoiding weighting functions in the conventional H_∞ method [115]. Moreover, the LMI-based approach presents more flexibility with less assumptions and restrictions associated with the conventional approach. Also, LMI problems can be efficiently solved using software packages such as MATLAB [121] and YALMIP [8]. Therefore, given the well-developed theory and solving tools, I will implement the robust H_∞ controller on a MIMO converter. To complete the controller design, the nominal stability (NS), nominal performance (NP), robust stability (RS), and robust performance (RP) are evaluated through the structured singular value synthesis [122].

A Design Approach: the Linear Matrix Inequality

In this subsection, I introduce the LMI control. The basic structure of the linear matrix inequality takes the following form

$$F(x) = F_0 + x_1 F_1 + x_2 F_2 + ... + x_m F_m > 0 \tag{5.1}$$

where $F_i = F_i^T$ is a given symmetric real matrix, for $i = 0, 1, \ldots, m$; x is a vector variable. Although the form in (5.1) seems restrictive, control constraints can be turned into the basic structure.

In many control problems, the variable is a matrix instead of a vector. In this case, the matrix inequality needs to be converted to the basic form in (5.1). Two standard LMI problems include the feasibility problems and the optimization problems [123]. Efficient numerical solving tools for LMI problems has been developed based on the ellipsoid method of the interior point method. Readers are referred to read [110] for more details for how LMIs are involved in control engineering.

UNIFIED MODEL OF A MIMO BOOST-AND-BUCK CONVERTER

Operational Modes of a MIMO Boost-and-Buck Converter

In this section, I will discuss the operation and modeling of a MIMO boost-and-buck converter. As shown in Fig. 5.1, a MIMO converter consists of four input/output (I/O) modules (one of them is shown in the shaded area in Fig. 5.1) and a common buffering stage consisting of a capacitor C_M and a battery. The MIMO boost-and-buck converter is a power router because bidirectional power flow can be achieved in every module. Due to the parallel combination of the capacitor C_M and the battery, the voltage of C_M is determined by the battery's internal voltage E_M, current i_{EM}, and internal resistance R_M. The battery allows balancing input and output power and it serves as a short time local power source for emergency circumstances.

According to whether the current or the voltage (of an I/O module) is controlled, I refer to current mode or voltage mode of an I/O module, respectively. Modules

independent operation leads to MIMO converters multiple operating modes. When an I/O module is in current mode, its inductor current is controlled. On the other hand, an I/O module can operate in voltage mode and regulate its capacitor C_i voltage. In either current mode or voltage mode, an I/O module can achieve bidirectional power flow and, thus, its inductor current direction could take either one of the two directions. When an I/O module is connected to a resistive load, its current must be negative according to the positive direction described in Fig. 5.1. Whether a module is voltage or current regulated is determined according to practical considerations. For instance, current control is desirable if a module is interfacing a fuel cell or an energy storage device, while voltage control could be applied to modules interfacing an ultra-capacitor with maximum current protection or a photovoltaic module for maximum power point tracking [59, 124]. Define an index set $O = \{0,1,2,3,4\}$ in which $\sigma \in O$ indicates the number of the I/O modules working in current mode and when v_{CM} is unregulated. Accordingly, five basic operational modes can be defined as described in Table 5. For instance, $\sigma = 2$ indicates that a MIMO converter is operating in Mode 2 and there are two I/O modules in current mode (modules #1 and #2). In reality, when one of the modules is used to regulate the dc link voltage v_{CM} there are also 4 possible additional operational modes that can be identified. One of those modes identified as Mode 5 in Table 5 involves module #1 regulating v_{CM}, for example to keep the battery at its floating voltage and the rest of the modules operating in voltage mode. Another example is Mode 8 in which Module #1 is regulating v_{CM} and all other modules are regulating their inductor currents. This is the case exemplified in [5]. Since the regulation target (i.e. the number of the voltage-mode and current-mode I/O modules) could vary, the controller design cannot be unique for all operational modes in Table 5. Whenever an operating mode is determined, a corresponding controller will be selected so that the regulation objectives are met. Consequently, the overall system becomes a switched control system [125]. Thus, selection among all 9 operational modes in Table 5 is done with such a switched

controller that commutates among operating modes depending on the power router conditions and operational needs. Although all 9 modes can be implemented in such switched controller, the focus of the analysis presented here is on the 5 basic modes 0 to 4 because the study of the other 4 modes (modes # 5 to 8) is trivial and well documented in the past as a cascade connection of dc-dc converters. However, it is relevant to mention that an issue may occur in modes #5 to 8 because modules #2 to 4 could behave as constant-power loads. Still, such issue is not discussed in here as suitable control approaches have already been presented in the past, such as in [126]. In order to determine the stability behavior of the switched control system for the basic operational modes, it is assumed that each subsystem is linear and the dwell time of each operating mode is sufficiently long. According to [125] the equilibrium point (EP) of the switched system is stable if each subsystem has a stable EP. Since the controller design procedure for all five basic operating modes is the same, the rest of the chapter focuses on the controller design and synthesis for the subsystem corresponding to $\sigma = 2$. Reference [127] illustrates a unified model of a bidirectional boost converter. As indicated in reference [127], a model is said to be unified if a single controller allows achieving the control goals regardless of the current-flow directions of the I/O modules. That is to say, a single unified controller is sufficient for a fixed σ.

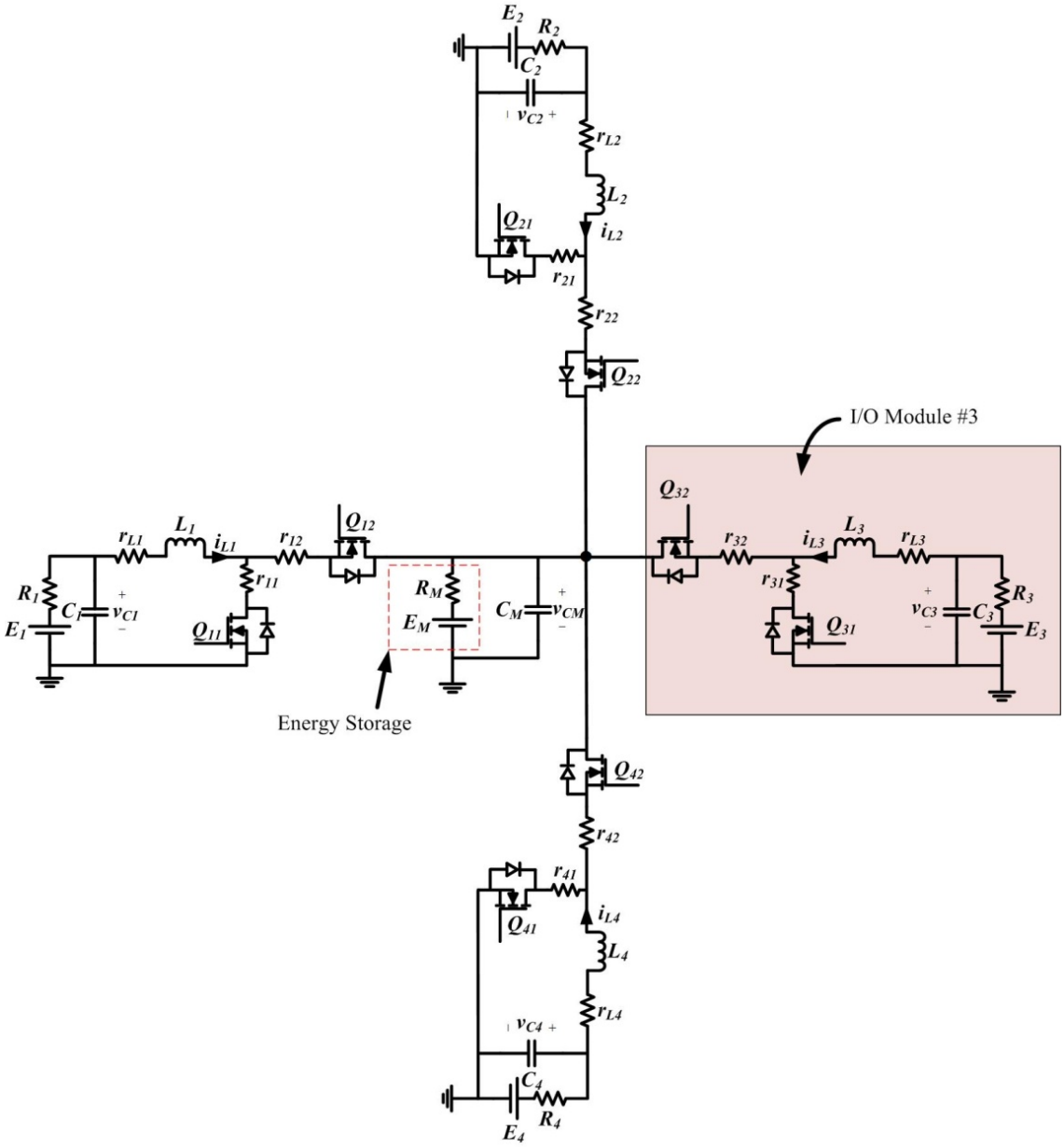

Figure 5.1: A Four-port MIMO Converter (a Power Router).

Power Management

Battery Operation

A typical charging process of a fully-discharged battery can be divided into 3 stages: constant current, constant voltage, and float stage. In the constant current stage

(also called bulk stage), the charging current is regulated to be at a battery's maximum safe value. For a 12-volt lead acid battery, its voltage at the constant current stage typically increases from 10.5 V to 15.0 V. The constant voltage stage, which is called the absorption charge, takes place after the constant current stage. In this stage, the voltage of the battery is regulated to let the battery to take whatever current. The current drops gradually from the maximum allowed current during the constant current stage. Voltage of a 12 V battery in this mode may vary between 14.4 to 14.7 volts [73]. When a battery is fully charged, the float stage occurs. In this stage, the charging voltage decreases (e.g., to 13.5 V to 13.8 V as indicated in [73]) and the current flowing through the battery is zero. This stage is intended to prevent a fully-charged battery from discharging. For batteries those that are not frequently used, e.g., a back-up battery in uninterruptible power system (UPS), the float charging can be important because the life of a battery may be significantly shortened if it is not used and discharges by itself for a few month.

Basic	Current-Controlled	Voltage-Controlled
Mode 0	None	#1, #2, #3, #4
Mode 1	#1	#2, #3, #4
Mode 2	#1, #2	#3, #4
Mode 3	#1, #2, #3	#4
Mode 4	#1, #2, #3, #4	None
Additional	Current-Controlled	Voltage-Controlled
Mode 5	None	#2, #3, #4
Mode 6	#2	#3, #4
Mode 7	#2, #3	#4
Mode 8	#2, #3, #4	None

(*) Module #1 is used to regulate v_{CM}.

Table 5: Operational Modes of the Power Router in Fig. 5.1

Power Management of a Four-port Power Router

Depending on the absence or presence of the buffering stage, the power router in Fig. 5.1 is said to be operating in either a balanced or an unbalanced condition. In the balanced condition, the battery current is zero. This condition could correspond to the

case that the battery is at its float voltage and the converter is in a steady state regime—hence, input and output power is balanced. Power management in such a condition has been studied in detail in, [23, 26, 103], and, hence, will not be further commented here. Instead, the focus is on unbalanced conditions. Nevertheless, the controller design and synthesis applied to an unbalanced condition discussed in this chapter, it can also be applied to a balanced condition.

A power router may operate in the unbalanced condition due to dynamic performance mismatches between power generation and consumption, for example, when a fuel cell is unable to follow varying loads due to its slow dynamic response. Operation of power routers can, then, be interpreted as analogous to data buffers used to compensate data rate unbalances in data routers. In the case of power routers, the battery connected to the dc link is used to compensate for differences between power generation and demand during unbalanced operation. For example, for a power router feeding critical loads in an electric ship, excess power may be drawn by loads and hence, power would be extracted from the buffering stage—battery. An extreme case could be that the batteries are used to feed the loads due to power source failure or an interruption in a power path between generators and a power router. If instead the loads fail to consume all the input power, surplus power is used to charge the battery. Exceptions may occur when the battery reaches its upper and lower charge limits. When the battery is fully charged, reference signals are generated to switch the controller into one of the additional modes 5 to 8 detailed in Table 5 or by switching to a basic mode (Modes 0 to 4 in Table 5) in which power input is controlled so it is less than the power output. When the battery reaches a given discharge level close to its lowest acceptable state of charge, proper references are generated in order to charge the battery if possible by switching the controller to one of the additional modes 5 to 8 detailed in Table 5 or by switching to a basic mode (Modes 0 to 4 in Table 5) in which power input is controlled so it is higher than the power output.

Unified Model Derivation

A conventional control configuration for a bidirectional boost converter could be achieved with two separate controllers: a boost controller and a buck controller. The boost controller is designed based on the boost model of the bidirectional converter; the control variable is the duty ratio of the main switch of a boost converter. Similarly, the buck converter is prescribed based on the buck model of the bidirectional converter; the control variable in buck mode is the duty ratio of the main switch of a buck converter. However, recent work shows two separate controllers can be replaced by a single unified controller by considering a unified model of the bidirectional converter [127]. The control variable can be the duty ratio of either one of the switches. The same idea can be extended to MIMO converters with multiple bidirectional ports and a unified model of the MIMO boost-and-buck converter is derived in a similar fashion. The unified averaged state-space model for the open-loop plant in Fig. 5.1 can be written as

$$\dot{x}(t) = A_P x(t) + B_u u(t) \tag{5.2}$$

where

$x(t) = \begin{bmatrix} x_1 & x_2 & x_3 & x_4 & x_5 & x_6 & x_7 & x_8 & x_9 \end{bmatrix}^T = \begin{bmatrix} v_{C1} & i_{L1} & v_{C2} & i_{L2} & v_{C3} & i_{L3} & v_{C4} & i_{L4} & v_{CM} \end{bmatrix}^T$ is the vector of state variables; $u(t) = \begin{bmatrix} E_1 & E_2 & E_3 & E_4 & E_M \end{bmatrix}^T$ is the vector of exogenous inputs and the entry of $u(t)$ could be zero (e.g., when it is associate with a pure resistive load); A_P, B_u are given by

$$A_P = \begin{bmatrix} \frac{-1}{R_1 C_1} & \frac{-1}{C_1} & 0 & 0 & 0 & 0 & 0 & 0 & 0 \\ \frac{1}{L_1} & \frac{-r_{eff,1}}{L_1} & 0 & 0 & 0 & 0 & 0 & 0 & -\frac{1-d_1}{L_1} \\ 0 & 0 & \frac{-1}{R_2 C_2} & \frac{-1}{C_2} & 0 & 0 & 0 & 0 & 0 \\ 0 & 0 & \frac{1}{L_2} & \frac{-r_{eff,2}}{L_2} & 0 & 0 & 0 & 0 & -\frac{1-d_2}{L_2} \\ 0 & 0 & 0 & 0 & \frac{-1}{R_3 C_3} & \frac{-1}{C_3} & 0 & 0 & 0 \\ 0 & 0 & 0 & 0 & \frac{1}{L_3} & \frac{-r_{eff,3}}{L_3} & 0 & 0 & -\frac{1-d_3}{L_3} \\ 0 & 0 & 0 & 0 & 0 & 0 & \frac{-1}{R_4 C_4} & \frac{-1}{C_4} & 0 \\ 0 & 0 & 0 & 0 & 0 & 0 & \frac{1}{L_4} & \frac{-r_{eff,4}}{L_4} & -\frac{1-d_4}{L_4} \\ 0 & \frac{1-d_1}{C_M} & 0 & \frac{1-d_2}{C_M} & 0 & \frac{1-d_3}{C_M} & 0 & \frac{1-d_4}{C_M} & \frac{-1}{R_M C_M} \end{bmatrix},$$

$$B_u = \begin{bmatrix} \frac{1}{R_1 C_1} & 0 & 0 & 0 & 0 \\ 0 & 0 & 0 & 0 & 0 \\ 0 & \frac{1}{R_2 C_2} & 0 & 0 & 0 \\ 0 & 0 & 0 & 0 & 0 \\ 0 & 0 & \frac{1}{R_3 C_3} & 0 & 0 \\ 0 & 0 & 0 & 0 & 0 \\ 0 & 0 & 0 & \frac{1}{R_4 C_4} & 0 \\ 0 & 0 & 0 & 0 & 0 \\ 0 & 0 & 0 & 0 & \frac{1}{R_M C_M} \end{bmatrix}, \tag{5.3}$$

$r_{eff,i} = r_{Li} + d_i \cdot r_{i1} + (1-d_i) r_{i2} = r_{Li} + r_i$ with $r_{i1} = r_{i2} = r_i$ and $i \in P$, $P = \{1, 2, 3, 4\}$.

Consider the EP of the system represented in (5.2) is given by $X(t) = \begin{bmatrix} V_{C1} & I_{L1} & V_{C2} & I_{L2} & V_{C3} & I_{L3} & V_{C4} & I_{L4} & V_{CM} \end{bmatrix}^T$. Note that d_i is the duty ratio of MOSFET Q_{i1} and $r_{eff,i}$ is independent of the duty ratios. Analysis shows the inductor current can be determined by

$$I_{Li} = \frac{-(1-d_i)E_M + E_i}{R_M(1-d_i)^2 + R_i + r_{Li} + r_{DS\_ON_i}}, \; i \in P \tag{5.4}$$

where $r_{DS\_ON_i}$ represents the on resistance of MOSFET Q_{i1}. Conversely, by realizing that the duty cycle takes values between zero and one, d_i can be solved as

$$d_i = 1 - \frac{-E_M + \sqrt{{E_M}^2 - 4I_{Li}R_M(I_{Li}R_{Ci} - E_i)}}{2I_{Li}R_M}, \; i \in P \tag{5.5}$$

where $R_{Ci} = R_i + r_{Li} + r_{DS\_ON_i}$ and $I_{Li} \neq 0$. In addition, it is observed from (3) that when $I_{Li} = 0$

$$d_i = 1 - E_i / E_M, \; i \in P. \tag{5.6}$$

Moreover, the denominator of (3) takes small values. Therefore, little variation of the duty cycle d_i, from the value given in (5.6), gives rise to large changes in the inductor current, I_{Li}. The large gain from duty ratio variation to inductor current variation is a good characteristic when comparing to time-multiplexing MICs in terms of current regulation range [20, 68].

UNCERTAIN MODEL OF THE MIMO BOOST-AND-BUCK CONVERTER

Small-signal Model

The control variables of the converter are the duty cycles d_i of shunt MOSFETs Q_{i1}. In order to derive the small-signal model, A matrix is written in the duty-dependent form:

$$A = A_0 + A_1 d_1 + A_2 d_2 + A_3 d_3 + A_4 d_4 \tag{5.7}$$

where, A_0, A_1, A_2, A_3, and A_4 can be written as

$$A_0 = \begin{bmatrix} \frac{-1}{R_1 C_1} & \frac{-1}{C_1} & 0 & 0 & 0 & 0 & 0 & 0 & 0 \\ \frac{1}{L_1} & \frac{-r_{eff,1}}{L_1} & 0 & 0 & 0 & 0 & 0 & 0 & -\frac{1}{L_1} \\ 0 & 0 & \frac{-1}{R_2 C_2} & \frac{-1}{C_2} & 0 & 0 & 0 & 0 & 0 \\ 0 & 0 & \frac{1}{L_2} & \frac{-r_{eff,1}}{L_2} & 0 & 0 & 0 & 0 & -\frac{1}{L_2} \\ 0 & 0 & 0 & 0 & 0 & \frac{-1}{C_3} & 0 & 0 & 0 \\ 0 & 0 & 0 & 0 & \frac{1}{L_3} & \frac{-r_{eff,3}}{L_3} & 0 & 0 & -\frac{1}{L_3} \\ 0 & 0 & 0 & 0 & 0 & 0 & 0 & \frac{-1}{C_4} & 0 \\ 0 & 0 & 0 & 0 & 0 & 0 & \frac{1}{L_4} & \frac{-r_{eff,4}}{L_4} & -\frac{1}{L_4} \\ 0 & \frac{1}{C_M} & 0 & \frac{1}{C_M} & 0 & \frac{1}{C_M} & 0 & \frac{1}{C_M} & \frac{-1}{R_M C_M} \end{bmatrix}$$

$$A_1 = \begin{bmatrix} 0 & 0 & 0 & 0 & 0 & 0 & 0 & 0 & 0 \\ 0 & 0 & 0 & 0 & 0 & 0 & 0 & 0 & \frac{1}{L_1} \\ 0 & 0 & 0 & 0 & 0 & 0 & 0 & 0 & 0 \\ 0 & 0 & 0 & 0 & 0 & 0 & 0 & 0 & 0 \\ 0 & 0 & 0 & 0 & 0 & 0 & 0 & 0 & 0 \\ 0 & 0 & 0 & 0 & 0 & 0 & 0 & 0 & 0 \\ 0 & 0 & 0 & 0 & 0 & 0 & 0 & 0 & 0 \\ 0 & 0 & 0 & 0 & 0 & 0 & 0 & 0 & 0 \\ 0 & -\frac{1}{C_M} & 0 & 0 & 0 & 0 & 0 & 0 & 0 \end{bmatrix} \quad A_2 = \begin{bmatrix} 0 & 0 & 0 & 0 & 0 & 0 & 0 & 0 & 0 \\ 0 & 0 & 0 & 0 & 0 & 0 & 0 & 0 & 0 \\ 0 & 0 & 0 & 0 & 0 & 0 & 0 & 0 & 0 \\ 0 & 0 & 0 & 0 & 0 & 0 & 0 & 0 & \frac{1}{L_2} \\ 0 & 0 & 0 & 0 & 0 & 0 & 0 & 0 & 0 \\ 0 & 0 & 0 & 0 & 0 & 0 & 0 & 0 & 0 \\ 0 & 0 & 0 & 0 & 0 & 0 & 0 & 0 & 0 \\ 0 & 0 & 0 & 0 & 0 & 0 & 0 & 0 & 0 \\ 0 & 0 & 0 & -\frac{1}{C_M} & 0 & 0 & 0 & 0 & 0 \end{bmatrix}$$

$$A_3=\begin{bmatrix} 0 & 0 & 0 & 0 & 0 & 0 & 0 & 0 & 0 \\ 0 & 0 & 0 & 0 & 0 & 0 & 0 & 0 & 0 \\ 0 & 0 & 0 & 0 & 0 & 0 & 0 & 0 & 0 \\ 0 & 0 & 0 & 0 & 0 & 0 & 0 & 0 & 0 \\ 0 & 0 & 0 & 0 & 0 & 0 & 0 & 0 & 0 \\ 0 & 0 & 0 & 0 & 0 & 0 & 0 & 0 & \frac{1}{L_3} \\ 0 & 0 & 0 & 0 & 0 & 0 & 0 & 0 & 0 \\ 0 & 0 & 0 & 0 & 0 & 0 & 0 & 0 & 0 \\ 0 & 0 & 0 & 0 & 0 & -\frac{1}{C_M} & 0 & 0 & 0 \end{bmatrix} \quad A_4=\begin{bmatrix} 0 & 0 & 0 & 0 & 0 & 0 & 0 & 0 & 0 \\ 0 & 0 & 0 & 0 & 0 & 0 & 0 & 0 & 0 \\ 0 & 0 & 0 & 0 & 0 & 0 & 0 & 0 & 0 \\ 0 & 0 & 0 & 0 & 0 & 0 & 0 & 0 & 0 \\ 0 & 0 & 0 & 0 & 0 & 0 & 0 & 0 & 0 \\ 0 & 0 & 0 & 0 & 0 & 0 & 0 & 0 & 0 \\ 0 & 0 & 0 & 0 & 0 & 0 & 0 & 0 & 0 \\ 0 & 0 & 0 & 0 & 0 & 0 & 0 & 0 & \frac{1}{L_4} \\ 0 & 0 & 0 & 0 & 0 & 0 & 0 & -\frac{1}{C_M} & 0 \end{bmatrix}.$$

Note that, in the derivation of matrix A in (5.7), the load admittances are considered as disturbance. Therefore, matrix A in (5.7) should be distinguished from A_P in (5.2). Then, the small-signal model can be written as

$$\begin{cases} \dot{\tilde{x}}(t) = A\tilde{x}(t) + B_w\tilde{w}(t) + B_d\tilde{d} \\ \tilde{z}(t) = C_z\tilde{x}(t) + D_{zw}\tilde{w}(t) + D_{zd}\tilde{d} \end{cases} \tag{5.8}$$

where $\tilde{d} = \begin{bmatrix} \tilde{d}_1 & \tilde{d}_2 & \tilde{d}_3 & \tilde{d}_4 \end{bmatrix}^T$ is the variation of the duty ratios; $\tilde{z}(t)$ is the variation of the output, and $\tilde{w}(t) = \begin{bmatrix} \tilde{E}_1(t) & \tilde{E}_2(t) & \tilde{G}_3(t) & \tilde{G}_4(t) & \tilde{E}_M(t) \end{bmatrix}$ incorporates disturbance originated in line voltages, load resistances, and the battery voltage; $\tilde{x} = \begin{bmatrix} \tilde{x}_1 & \tilde{x}_2 & \tilde{x}_3 & \tilde{x}_4 & \tilde{x}_5 & \tilde{x}_6 & \tilde{x}_7 & \tilde{x}_8 & \tilde{x}_9 \end{bmatrix}^T = \begin{bmatrix} \tilde{v}_{C1} & \tilde{i}_{L1} & \tilde{v}_{C2} & \tilde{i}_{L2} & \tilde{v}_{C3} & \tilde{i}_{L3} & \tilde{v}_{C4} & \tilde{i}_{L4} & \tilde{v}_{CM} \end{bmatrix}^T$ is the variation of the state variables. D_{zw} and D_{zd} are zero matrices. B_d, B_w, and C_z are given by

$$B_d = \begin{bmatrix} A_1 X & A_2 X & A_3 X & A_4 X \end{bmatrix} = \begin{bmatrix} 0 & 0 & 0 & 0 \\ V_{CM}/L_1 & 0 & 0 & 0 \\ 0 & 0 & 0 & 0 \\ 0 & V_{CM}/L_2 & 0 & 0 \\ 0 & 0 & 0 & 0 \\ 0 & 0 & V_{CM}/L_3 & 0 \\ 0 & 0 & 0 & 0 \\ 0 & 0 & 0 & V_{CM}/L_4 \\ -I_{L1}/C_M & -I_{L2}/C_M & -I_{L3}/C_M & -I_{L4}/C_M \end{bmatrix}$$

$$B_w = \begin{bmatrix} 1/(R_1C_1) & 0 & 0 & 0 & 0 \\ 0 & 0 & 0 & 0 & 0 \\ 0 & 1/(R_2C_2) & 0 & 0 & 0 \\ 0 & 0 & 0 & 0 & 0 \\ 0 & 0 & V_{C3}/C_3 & 0 & 0 \\ 0 & 0 & 0 & 0 & 0 \\ 0 & 0 & 0 & V_{C4}/C_4 & 0 \\ 0 & 0 & 0 & 0 & 0 \\ 0 & 0 & 0 & 0 & 1/(R_MC_M) \end{bmatrix}$$

$$C_z = \begin{bmatrix} 0 & 1 & 0 & 0 & 0 & 0 & 0 & 0 & 0 \\ 0 & 0 & 0 & 1 & 0 & 0 & 0 & 0 & 0 \\ 0 & 0 & 0 & 0 & 1 & 0 & 0 & 0 & 0 \\ 0 & 0 & 0 & 0 & 0 & 0 & 1 & 0 & 0 \end{bmatrix}. \tag{5.9}$$

Open-loop Analysis

Although a decentralized controller is not implemented in this design, it is of interest to evaluate if the performance loss is caused by a decentralized control scheme through an open-loop analysis. Since a decentralized control does not attempt to counteract the multivariable interactions, in plants with strong interactions its performance may be poor [128]. The relative gain array (RGA) provides a numerical measurement of multivariable interactions [56-57, 128]. For a plant presenting large RGA elements (typically larger than 5), a decentralized controller may yield a poor performance [128]. Let $G_d(s)$ be the control to output transfer function matrix of the open-loop plant described in (5.8). The RGA of $G_d(s)$ can be computed with respect to frequency. The largest RGA element of

$G_d(s)$ is plotted as a function of frequency in Fig. 5.2 with $R_M = 0.3\ \Omega$. The vertical axis of Fig. 5.2 represents the RGA value whose unit is one. Showing a RGA element higher than 5 (in low frequencies), Fig. 5.2 reveals that the multivariable interaction of the open-loop plant $G_d(s)$ is so strong that a decentralized should not be chosen in order to guarantee nominal and robust performance when $R_M = 0.30\ \Omega$. Thus, a multivariable controller becomes preferable when $R_M \geq 0.30\ \Omega$ because a larger R_M corresponds to stronger interactions. Another important consideration discussed in Section I is that the decentralized control is always subject to essential limitations, e.g., it cannot guarantee disturbance-attenuation or robustness to uncertainties for a MIMO control system. In this design, a multivariable controller is chosen because R_M is found to be 0.33 Ω in our experimental setup and disturbance-attenuation and robustness are required design goals.

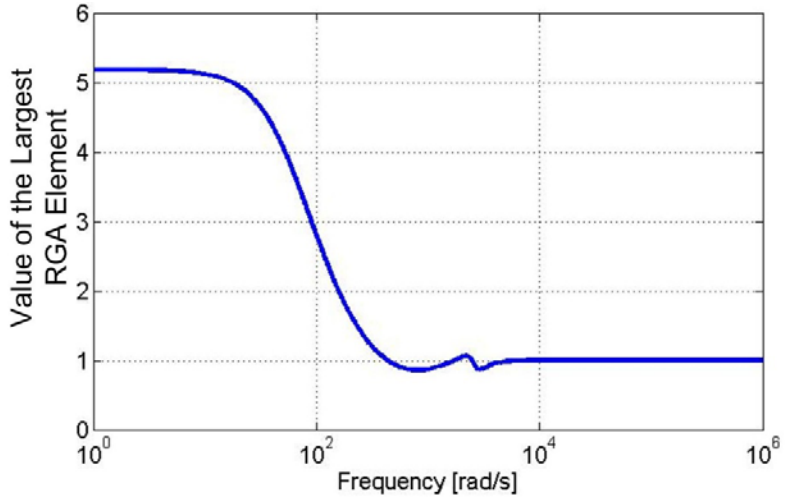

Figure 5.2: The Largest RGA Element of the Open-loop Plant with Respect to Frequency with $R_M = 0.3\ \Omega$.

Uncertain Model of the Proposed Four-Port Converter

Uncertainties Caused by Neighboring MIMO Converters

The interactions between MIMO converters are taken into account through uncertainties. Consider that two MIMO converters are connected through Module *a* of MIMO converter #1 and Module *b* of MIMO converter #2, as shown in Fig. 5.3. Also,

consider that power flows from Module *a* to Module *b*. In the control design of MIMO converter #2, I consider that port *b* is connected to a voltage source E_b with a resistance R_b. The effect of the MIMO converter #1 on the MIMO converter #2 is represented by uncertain time-varying E_b and R_b. On the other hand, in the control design for MIMO converter #1, I consider that module *a* is connected to a load which consists of an source with uncertain time-varying E_a and R_a. The effect of the MIMO converter #2 on the MIMO converter #1 is represented by the time-varying voltage E_a and R_a. Therefore, the interactions from neighbor MIMO converters can be treated as uncertainties in the controller design. It is worth to note that the controller design and synthesis both allow for arbitrary change in uncertain time-varying parameters in the chapter. Hence, all possible variations, e.g., a sudden voltage drop due to faults or a slow voltage variation due to converter dynamics, are within the consideration of the design and synthesis.

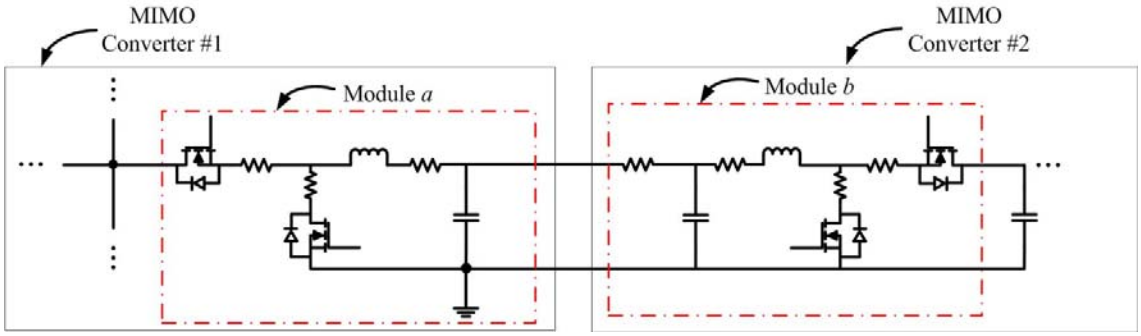

Figure 5.3: Neighbor MIMO Converters.

Uncertainties Caused by Renewable Energy Sources

Renewable energy sources present nonlinear behavior and are subject to time-varying factors. For example, the current-voltage (*i*-*v*) relationship of a PV module is nonlinear [1]. Moreover, the *i*-*v* curve of a PV module changes significantly with the temperature and solar radiation. Under given temperature and solar radiation, the dynamic characteristic of a PV module is dependent on the operating point (*i*-*v* pair). Reference [124] shows that a PV module can be linearized at a nominal operating point

and approximated by the circuit in Fig. 5.4. Parameters V_{eq} and R_{eq} can be derived according to the discussion in [61, 129]. Typically, the operation of a PV module can be divided into three regions: the constant current region, the constant voltage region, and the power region.

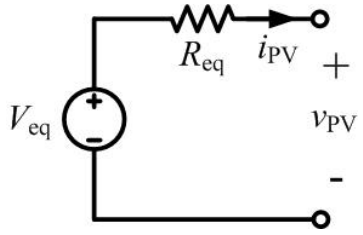

Figure 5.4: Linearized Model of a PV Module.

A control design can be performed and optimized based on the MPP. Then, a subsequent problem is that the controller may not behave well when the operating point moves away from the MPP. Therefore, a validation of the stability and performance of the closed-loop system should be performed which considers all three regions of PV modules. Special attention should be paid to the operation in the constant current mode, because a PV module behaves as a lightly damped system and becomes difficult to control [59]. The synthesis of a designed controller becomes more complicated for an MIC because the system consists of multiple independent PV modules. In this case, it would be necessary to evaluate the stability under the worst operating condition—all the PV modules are in constant current region.

However, this design approach by focusing on MPP and verifying for all three operation modes may be problematic from a control perspective. The reason is that, when a PV module is modeled as a time-varying linear system with uncertain parameters (V_{eq} and R_{eq}), the exponential stability of LTI models in different modes cannot guarantee the stability of the time-varying model. One alternative is to consider V_{eq} and R_{eq} as uncertainties. Once the uncertainties are considered, the problem left is to design a controller which guarantees the stability of the uncertain model.

Uncertain Model

Next, consider I/O module 1 and 2 are connected to neighboring converters, respectively; consider I/O module 3 and 4 are connected to pure resistive loads. Therefore, the uncertainties involved may be the line voltages E_1, E_2, line resistances R_{1b}, R_{2b}, and load resistance R_3, R_4. For simplicity and due to a practical consideration of small variation of R_{1b}, R_{2b}, the line resistances are considered as constant and well-known in this design. Two additional uncertainties originated from the varying duty ratios of Q_{31} and Q_{41} are considered, too. In summary, I consider parametric uncertainties in the system matrices in (5.10) and rewrite the small-signal model as an uncertain time-varying state-space model in the following equation

$$\begin{cases} \dot{\tilde{x}}(t) = A(\delta)\tilde{x}(t) + B_w(\delta)\tilde{w}(t) + B_d(\delta)\tilde{d}(t) \\ \tilde{z}(t) = C_z(\delta)\tilde{x}(t) + D_{zw}(\delta)\tilde{w}(t) + D_{zd}(\delta)\tilde{d}(t) \end{cases} \quad \text{with } \delta = \begin{bmatrix} E_1 & E_2 & G_3 & G_4 & d_3 & d_4 \end{bmatrix}^T \tag{5.10}$$

where $\tilde{x}(t) \in \Re^n$, $A(\delta) \in \Re^{n\times n}$, $B_w(\delta) \in \Re^{n\times s}$, $B_d(\delta) \in \Re^{n\times m}$, $C_z(\delta) \in \Re^{p\times n}$, $D_{zw}(\delta) \in \Re^{p\times m}$, and $D_{zd}(\delta) \in \Re^{p\times m}$; δ is the vector of the uncertain parameters (E_1, E_2, G_3, and G_4) and variables (d_3 and d_4), $G_3 = 1/R_3$, $G_4 = 1/R_4$, and d_3, d_4 represents the duty ratios of Q_{31}, Q_{41}, respectively. $B_w(\delta)$ is given in (5.11). With the assumptions $E_M = V_{CM}$, $I_{L3} = -G_3 d_3 E_M$ and $I_{L4} = -G_4 d_4 E_M$, $B_d(\delta)$ can be given by

$$B_d(\delta) = \begin{bmatrix} 0 & 0 & 0 & 0 \\ E_M / L_1 & 0 & 0 & 0 \\ 0 & 0 & 0 & 0 \\ 0 & E_M / L_2 & 0 & 0 \\ 0 & 0 & 0 & 0 \\ 0 & 0 & E_M / L_3 & 0 \\ 0 & 0 & 0 & 0 \\ 0 & 0 & 0 & E_M / L_4 \\ -I_{L1} / C_M & -I_{L2} / C_M & G_3 d_3 E_M / C_M & G_4 d_4 E_M / C_M \end{bmatrix}. \tag{5.11}$$

Generally, each element of δ, p_j (j=1, 2, …, k, k=6) is bounded by an upper limit and a lower limit [121]. Therefore the value of the vector $\delta = [p_1, \ ..., \ p_k]^T$ is located inside the hyper-rectangle with $N_\delta = 2^k$ vertices in the space $\Re^k$. The uncertain parameters (E_1, E_2, G_3, and G_4) and variables (d_3 and d_4) are considered as parametric uncertainties as indicated in (5.10). Note that it may be that the duty ratios must vary so d_1 or d_2 is also an uncertain variable. The reason why d_1 or d_2 is not included in the uncertainty vector δ in (5.11) is that d_1 or d_2 varies within a small neighborhood of $1-E_1/E_M$ or $1-E_2/E_M$, respectively (recall the analysis in the previous section). Hence, d_1 or d_2 is considered as a dependent variable on E_1 or E_2, respectively. Values of the parameters/variables are given in Table 6. I consider that, except the parametric uncertainties (E_1, E_2, G_3, G_4, d_3, and d_4) and the dependent variables (d_1, d_2, I_{L3}, and I_{L4}), all the other parameters/variables are well-known and time-invariant.

Consider the system matrix $S(\delta) = \begin{bmatrix} A(\delta) & B_w(\delta) & B_d(\delta) \\ C_z(\delta) & D_{zw}(\delta) & D_{zd}(\delta) \end{bmatrix}$, which ranges in a polytope. Then the uncertain time-varying system can be represented via the polytopic model [121] (or polytopic linear differential inclusions in [110]) in the following equation

$$S(\delta) \in Co\{S_1, ..., S_{N_\delta}\} := \{\sum_{i=1}^{N_\delta} \alpha_i S_i : \ \alpha_i \geq 0, \ \sum_{i=1}^{N_\delta} \alpha_i = 1\}.. \tag{5.12}$$

Each vertex of the hyper-rectangle (δ_i, i=1, 2, …, N_δ, N_δ =2^k) corresponds to a vertex of the polytope ($S_i = S(\delta_i)$, i = 1, 2, …, N_δ). The $S(\delta)$ takes its value within the convex polytope with vertices S_i, i = 1, 2, …, N_δ. Note that the polytopic model consists of N_δ=64 vertices in this design because k = 6.

Parameter or Variable	Value	Unit
E_1 , E_2	[12, 18]	V
G_3 , G_4	[0.02, 0.1]	Siemens
d_3 , d_4	[0, 1]	

I_{L1} , I_{L2}	1	A
E_3 , E_4	0	V
R_1 , R_2	0.15	Ω
R_M	0.33	Ω
E_M	26.6	V
L_1, L_2, L_3, L_4	320	μH
C_1, C_2, C_3, C_4, C_M	470	μF
r_{11}, r_{12}, r_{21}, r_{22}, r_{31}, r_{32}, r_{41}, r_{42}	0.05	Ω
Switching frequency	30	kHz

Table 6: Values of (Uncertain) Parameters and Variables of the Power Router in Fig. 5.1.

ROBUST CONTROLLER DESIGN

Stability Analysis of Uncertain Linear Systems

Now, consider the uncertain system

$$\dot{x}(t) = A(\delta)x(t) \tag{5.13}$$

where $x \in \Re^n$ is the vector of the state variables of the system in (5.13), $A(\delta)$ is the function of the real value vector $\delta = [p_1, \quad ..., \quad p_k]^T \in \Re^k$. I assume that the vector of the parametric uncertainties, δ , varies within a given hyper-rectangle $R = [\underline{p}_1, \quad \overline{p}_1] \times [\underline{p}_2, \quad \overline{p}_2] \times ... [\underline{p}_k, \quad \overline{p}_k]$.

For a system with time-varying uncertainties, if there exists a symmetric matrix $P \in \Re^{n \times n}$ such that

$$P > 0, \; A^T(\delta)P + PA(\delta) < 0 \;\; \forall \delta \in R \tag{5.14}$$

then the system in (5.13) is quadratically stable [110]. By applying the Lyapunov direct method, it is shown that the linear time-varying system in (5.13) is exponentially stable if it is quadratically stable.

Since R is an infinite set, (5.14) represents a feasibility problem consisting of infinite linear matrix inequalities. This feasibility problem is significantly simplified [130-132] if the system matrix $A(\delta)$ can be written as the ratio of a multi-affine matrix

function of δ and a multi-affine polynomial of δ, then the quadratic stability of (5.13) is equivalent to the feasibility of 2^k+1 LMIs in

$$P > 0,\ A^T(\delta_i)P + PA(\delta_i) < 0 \quad i = 1,\ 2,\ 3,\ ...,\ 2^k . \tag{5.15}$$

On the Time-invariance of P

The time-invariance of P is critical in dealing with arbitrary changes in parameters, as implied in (5.14). Then, a desirable characteristic brought by a constant P is that a time-invariant controller is sufficient for quadratic stabilization. Hence, due to the time-invariance of P, the control configuration can be significantly simplified. Second, (5.14) shows that the quadratic stability allows for arbitrary changes in parameters: the parameters could be constant but unknown; the parameters could also be time-varying with bounded variation rates; the parameters could even be time-varying with unknown behavior in time. The robustness implied by the quadratic stability might be beneficial for power electronics systems whose inputs and loads may be subject to unknown complicated variations.

Even though could be simplified by (5.15), (5.14) represents a fairly strict requirement, particularly for systems with a large number of parametric uncertainties. Furthermore, it is found that the existence of a matrix P cannot be guaranteed even a (linear time-varying) system is exponentially stable. One example is given in reference [125] for a switched linear system, which is essentially a special case of linear time-varying systems. Therefore, the quadratic stability defined in (5.14) may be conservative. In particular, in control applications where parameters are slowly-varying, it is usually desirable to find a P which is dependent on parameters δ instead of constant. Then, a parameter-dependent quadratic Lyapunov function $V(\delta, x) = x^T P(\delta) x$ could be used for stability analysis. Comparing to the quadratic stability, an key stage in the search of $P(\delta)$ is the choice the structure for $P(\delta)$ [131]. Exponential stability can be determined through the existence of a $P(\delta)$ which allows for quadratic stabilization

[131]. Further details of the control design with a parameter-dependent $P(\delta)$ are out of the scope of this dissertation. Readers are referred to [131] for additional details of $P(\delta)$ for systems in which parameters are varying but with a bounded rate of variation.

Control Structure

There are two options when selecting the control structure for the power router: state-feedback control and output-feedback control [131]. The disadvantage of the state-feedback control is that it may need more sensors than an output-feedback control. Moreover, in some cases, states that cannot be measured may make state-feedback control impossible to be implemented. However, the other option (output-feedback control) presents more important disadvantages for the proposed application. When the goal is to achieve quadratic stabilization of an uncertain plant, the output feedback becomes parameter-dependent [131]. Therefore, the output-feedback control also requires sensors for on-line measurements of parameters or variables. Another disadvantage of an output-feedback is that, it typically doubles the order of the open-loop plant, which increases the order of the system and makes it more difficult to treat. Therefore, an output-feedback control may be more complicated than a state-feedback one. In the MIMO boost-and-buck converter, each state variable is potentially a regulation target, so the potential problem of state feedback controllers of not being able to measure some state variables is not found in the proposed application discussed here of dc-dc MIMO converters. If all the states are available, it is natural to implement a state-feedback controller. Considering that the disadvantages of the output feedback control for the proposed application are more important that those observed for state feedback control, I select the state feedback control structure. In fact, the conclusion in [133] allows simplifying the feedback controller design because [133] shows that if an uncertain linear system is quadratically stabilizable through a dynamic state-feedback controller, then the system is also quadratically stabilizable via a static state feedback controller. Reference

[134] shows a necessary and sufficient condition of the quadratic stabilization through static state feedback control. Therefore, the control design problem is modeled as a convex optimization problem under the assumptions stated in [134].

In order to eliminate dc offsets of the output variables, integrals of the errors between the references and the outputs are added as new state variables, which are connected to the state-feedback controller *K*. The selected state feedback control structure is illustrated in Fig. 5.5.

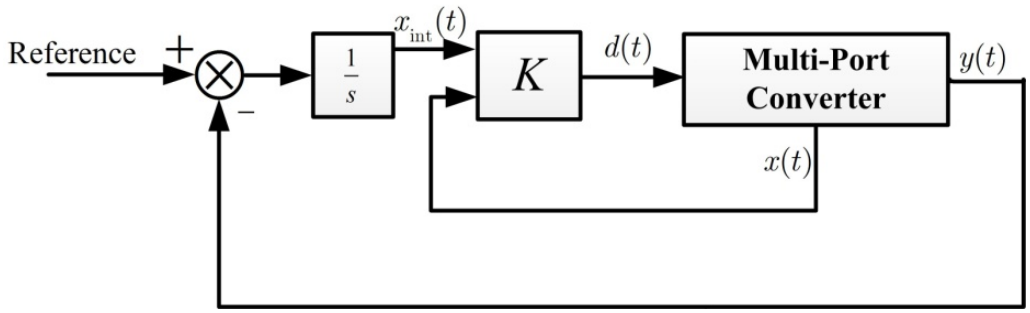

Figure 5.5: Block Diagram of the State-feedback Control Structure.

H_∞ *Control*

Consider in Fig. 5.6 a general control configuration without uncertainty. Let $F(s)$ be the closed-loop transfer function from disturbance $w(t)$ to output $z(t)$, then $Z(s) = F(s)W(s)$ by applying the Laplace transform.

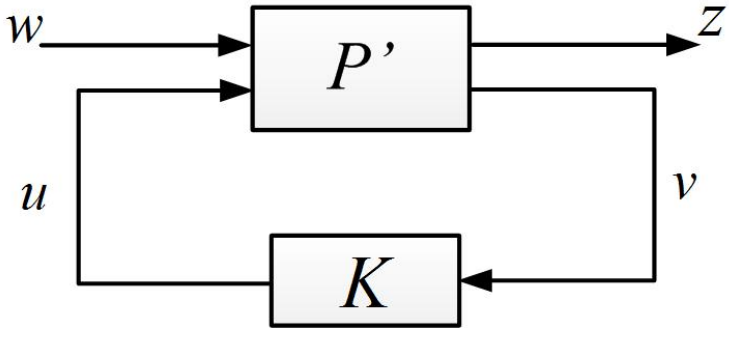

Figure 5.6: A General Control Configuration.

The target of the H_∞ control design is to find all stabilizing controllers which guarantees $\|F\|_\infty < \gamma$, where $\|F\|_\infty = \sup_\omega \bar{\sigma}(F(j\omega))$, $\sigma(\cdot)$ denotes the singular value, and $\bar{\sigma}(F(j\omega))$ represents the maximum singular value of $F(j\omega)$. For a multivariable control system, the ∞-norm of F can be further written as $\|F\|_\infty = \sup_{w \in C^m} \sup_\omega \bar{\sigma}(F(j\omega))$ to explicitly express the dependence on the direction of inputs. Disturbance *w* is in C^m because time delay should be considered when the input is a vector. On the other hand, the time-domain interpretation of the infinity norm of the transfer function matrix $F(s)$ can be expressed by

$$\|F\|_\infty = \sup_{\|w\| \neq 0} \frac{\|z(t)\|_2}{\|w(t)\|_2} \tag{5.16}$$

where $\|z(t)\|_2 = \sqrt{\int_0^\infty \sum |z_i(t)|^2 \, dt}$ is the 2-norm of a vector signal. According to the meaning of energy of the induced 2-norm, (5.16) shows that the H_∞ control suppress the response of when a disturbance $w(t)$ has bounded energy. The time-domain interpretation in (5.16) may be restrictive, because practically disturbances are not necessarily bounded in energy, for example, step disturbances. Therefore, in the controller design and synthesis, the frequency-domain interpretation of H_∞ control becomes more useful.

LMI Synthesis of State Feedback Controllers

We seek a state-feedback controller that quadratically stabilizes the uncertain model of the MIMO converter while satisfying the H_∞ norm (for disturbance-attenuation) and pole-placement (for time-domain response) constraints.

We will review some important results, which are necessary building blocks for the quadratic stabilization through state feedback control for MIMO converters derived in this work. Consider an uncertain system represented as

$$\begin{cases} \dot{x}(t) = A(\delta)x(t) + B_w(\delta)w(t) + B_d(\delta)d(t) \\ z(t) = C_z(\delta)x(t) + D_{zw}(\delta)w(t) + D_{zd}(\delta)d(t) \end{cases} \tag{5.17}$$

where $x(t) \in \Re^n$, $A(\delta) \in \Re^{n\times n}$, $B_w(\delta) \in \Re^{n\times s}$, $B_d(\delta) \in \Re^{n\times m}$, $C_z(\delta) \in \Re^{p\times n}$, $D_{zw}(\delta) \in \Re^{p\times s}$, and $D_{zd}(\delta) \in \Re^{p\times m}$. Hence, in the case of the four-port MIMO converter in Fig. 5.1, n=13, m=4, s=5, and p=4 represent the number of state variables, control variables, disturbances, and outputs, respectively.

***Theorem* 1** [135]

The system in (5.17) is quadratically stabilizable by state feedback $u = Kx$ if and only if there exist a symmetric matrix $W \in \Re^{n\times n}$ and a matrix $Y \in \Re^{m\times n}$ such that

$$\begin{cases} W > 0 \\ A(\delta)W + WA(\delta)^T + B_d(\delta)Y + Y^T B_d(\delta)^T < 0 \end{cases}. \tag{5.18}$$

A controller for such state feedback is given by $K = YW^{-1}$.

Assume that the system matrix $\begin{bmatrix} A(\delta) & B_d(\delta) \end{bmatrix}$ can be written as the ratio of a multi-affine matrix-value and a multi-affine polynomial function, the quadratic stabilization through state feedback is the necessary and sufficient condition of the feasibility of 2^k+1 LMIs

$$W > 0,\ A(\delta_i)W + WA(\delta_i)^T + B_d(\delta_i)Y + Y^T B_d(\delta_i)^T < 0,\ \ i = 1,\ 2,\ 3,\ ...,\ 2^k. \tag{5.19}$$

***Theorem* 2** [120]

The system in (5.17) is stabilizable by state-feedback $u = Kx$ and $\max_{\|w\|\neq 0} \dfrac{\|z(t)\|_2}{\|w(t)\|_2} < \gamma$ if and only if there exist a symmetric positive-definite matrix $W \in \Re^{n\times n}$ and a matrix $Y \in \Re^{m\times n}$ such that

$$\begin{bmatrix} A(\delta)W + WA(\delta)^T + B_d(\delta)Y + Y^T B_d(\delta)^T & B_w(\delta) & WC_z(\delta)^T + Y^T D_{zd}(\delta)^T \\ B_w(\delta)^T & -\gamma^2 I & D_{zw}(\delta)^T \\ C_z(\delta)W + D_{zd}(\delta)Y & D_{zw}(\delta) & -I \end{bmatrix} < 0. \tag{5.20}$$

A controller for such state feedback is given by $K = YW^{-1}$.

Again, if the system matrix $\begin{bmatrix} A(\delta) & B_w(\delta) & B_d(\delta) \\ C_z(\delta) & D_{zw}(\delta) & D_{zd}(\delta) \end{bmatrix}$ can be written as the ratio of a multi-affine matrix-value and a multi-affine polynomial function, the quadratic stabilization through state feedback is the necessary and sufficient condition of the feasibility of 2^k+1 LMIs

$$W > 0, \begin{bmatrix} A(\delta_i)W + WA(\delta_i)^T + B_u(\delta_i)Y + Y^T B_d(\delta_i)^T & B_w(\delta_i) & WC_z(\delta_i)^T + Y^T D_{zd}(\delta_i)^T \\ B_w(\delta_i)^T & -\gamma^2 I & D_{zw}(\delta_i)^T \\ C_z(\delta_i)W + D_{zd}(\delta_i)Y & D_{zw}(\delta_i) & -I \end{bmatrix} < 0 .$$
$$i = 1,\ 2,\ 3,\ ...,\ 2^k \tag{5.21}$$

In addition, it is not necessary to define $G_3 d_3$ and $G_4 d_4$ in B_d by new independent parametric uncertainties because this assumption is satisfied.

The H_∞ control is essentially a frequency-domain approach which guarantees closed-loop stability of the closed-loop system but does not ensure a given time domain response. In order to perform closed-loop pole placement within a specified region, I need to consider the H_∞ norm and pole-placement objectives simultaneously. Some additional properties such as the pole placement can be stated by the next theorem.

***Theorem* 3** [136]

Consider $S(\lambda, r, \theta)$ is a set of complex numbers $x + jy$ such that $x < -\lambda < 0,\ |x + jy| < r,$ and $x \cdot \tan\theta < -|y|$. The closed-loop poles of the system with state-feedback are inside the region $S(\lambda, r, \theta)$ if and only if there exist a symmetric positive definite positive matrix W and a matrix Y such that

$$A(\delta)W + WA(\delta)^T + B_d(\delta)Y + Y^T B_d(\delta)^T + 2\lambda W < 0 \tag{5.22}$$

$$\begin{bmatrix} -rW & WA(\delta)^T + Y^T B_d(\delta)^T \\ A(\delta)W + B_d(\delta)Y & -rW \end{bmatrix} < 0 \tag{5.23}$$

$$\begin{bmatrix} \cos\theta(A(\delta)W + WA(\delta)^T + B_d(\delta)Y + Y^T B_d(\delta)^T) & \sin\theta(A(\delta)W - WA(\delta)^T + B_d(\delta)Y - Y^T B_d(\delta)^T) \\ \sin\theta(-A(\delta)W + WA(\delta)^T - B_d(\delta)Y + Y^T B_d(\delta)^T) & \cos\theta(A(\delta)W + WA(\delta)^T + B_d(\delta)Y + Y^T B_d(\delta)^T) \end{bmatrix} < 0 \tag{5.24}$$

and $K = YW^{-1}$ is the state feedback gain. Again, the pole-placement constraints can be converted to feasibility LMI problems if the system matrix can be written as the ratio of a multi-affine matrix-value and a multi-affine polynomial function.

A robust H_∞ controller design problem can be formulated with theorems 2 and 3. The aim is to find the matrix W and Y that minimize the H_∞ performance bound γ, while satisfying the inequality constraints stated in theorem 2 and 3, for all the extrema of the polytopic model $\{S_1, ..., S_{N_\delta}\}$. Hence, the problem to be solved is

$$\begin{gathered} \min_{W,Y} \ \gamma \\ \text{such that} \\ W > 0, \\ \begin{bmatrix} A(\delta_i)W + WA(\delta_i)^T + B_d(\delta_i)Y + Y^T B_d(\delta_i)^T & B_w(\delta_i) & WC_z(\delta_i)^T + Y^T D_{zd}(\delta_i)^T \\ B_w(\delta_i)^T & -\gamma^2 I & D_{zw}(\delta_i)^T \\ C_z(\delta_i)W + D_{zd}(\delta_i)Y & D_{zw}(\delta_i) & -I \end{bmatrix} < 0, \\ A(\delta_i)W + WA(\delta_i)^T + B_d(\delta_i)Y + Y^T B_d(\delta_i)^T + 2\lambda W < 0, \\ \begin{bmatrix} -rW & WA(\delta_i)^T + Y^T B_d(\delta_i)^T \\ A(\delta_i)W + B_d(\delta_i)Y & -rW(\delta_i) \end{bmatrix} < 0, \\ \begin{bmatrix} \cos\theta(A(\delta_i)W + WA(\delta_i)^T + B_d(\delta_i)Y + Y^T B_d(\delta_i)^T) & \sin\theta(A(\delta_i)W - WA(\delta_i)^T + B_d(\delta_i)Y - Y^T B_d(\delta_i)^T) \\ \sin\theta(-A(\delta_i)W + WA(\delta_i)^T - B_d(\delta_i)Y + Y^T B_d(\delta_i)^T) & \cos\theta(A(\delta_i)W + WA(\delta_i)^T + B_d(\delta_i)Y + Y^T B_d(\delta_i)^T) \end{bmatrix} < 0. \end{gathered} \tag{5.25}$$

where δ_i is the i-*th* vertex of the hyper-rectangle R, i=1, 2, 3, …, 2^k.

Controller Design Result

Parameters for the pole placement constraint are selected from

$$\lambda = 1000,\ r = 15000,\ \theta = 25\pi/180 \tag{5.26}$$

The parameter λ is chosen to ensure the real parts of the closed-loop poles are sufficiently far from the imaginary axis so that the closed-loop system has a fast enough

response; r is selected to limit the distances between closed-loop poles and the imaginary axis so that the bandwidth of the closed-loop system is significantly smaller than the switching frequency; θ is chosen to be relatively small to suppressed the oscillatory behavior. When the problem in (5.25) is solved using the YALMIP toolbox [73], I found that the minimum γ to be 0.1109 and the controller gain K to be

$$K = \begin{bmatrix} -0.036752 & -0.14563 & -0.000050744 & 0.000054006 & 0.002504 & 0.000188 & 0.002302 & 0.000188 & 0.020775 & 211.56 & -0.14097 & -2.2587 & -2.3942 \\ -0.000056527 & 0.000029802 & -0.036753 & -0.14568 & 0.002435 & 0.000191 & 0.002333 & 0.000178 & 0.020775 & -0.1368 & 211.57 & -2.1159 & -2.4434 \\ 0.00065146 & 0.0076093 & 0.00070847 & 0.0071729 & 0.98531 & -0.18217 & 0.018935 & -0.0012 & 0.013831 & 0.27507 & 0.99931 & -1299.9 & -53.337 \\ 0.00058941 & 0.0066923 & 0.00054778 & 0.0072734 & 0.021069 & -0.00078 & 0.98276 & -0.17749 & 0.013871 & 0.37467 & -0.23516 & -46.057 & -1273.3 \end{bmatrix}. \quad (5.27)$$

CONTROLLER SYNTHESIS

Nominal Stability and Nominal Performance

Once the controller design is complete, it is of interest to test the nominal stability (NS), nominal performance (NP), robust stability (RS), and robust performance (RP) of the closed-loop system. The NS and NP are stability and performance specifications associate with a nominal plant. A system is NS if it is stable without model uncertainty while NP of a system means that performance objectives are satisfied without model uncertaiy.

Robust Stability and Robust Performance

RS and RP deal with perturbed plants. The definitions of RS and RP are quoted from [56]:

RS. The system is stable for all perturbed plants about the nominal model up to the worst-case model uncertainty.

RP. The system satisfies the performance specifications for all perturbed plants about the nominal model up to the worst-case model uncertainty.

In a formal robustness analysis, the set of all possible uncertain perturbations are represented by a normlized block-diagonal matrix Δ ($\|\Delta\|_\infty \le 1$). Then, Δ is pulled out

of a nominal system and a standard $M\Delta$ configuration can be derived, as shown in Fig. 5.7.

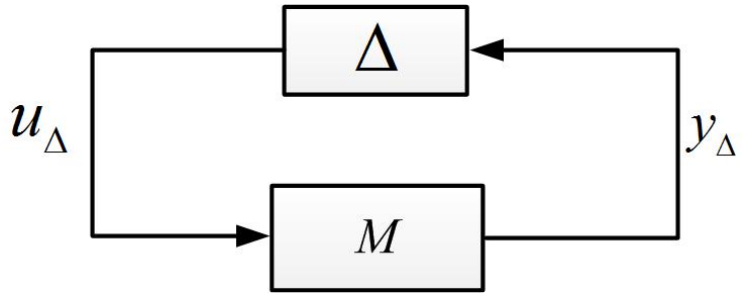

Figure 5.7: The $M\Delta$ structure.

Notice that the controller *K* is a portion of *M* in a $M\Delta$ representation in Fig. 5.7. *M* can be divided into the generalized plant *P'* and the controller *K*, which is described by Fig. 5.8. Furthermore, an $N\Delta$ representation (see Fig. 5.9) can be derived with a designed controller *K*. Transfer function matrix *P'* can be partitioned into P_{11}, P_{12}, P_{21}, and P_{22}, then it is not difficult to derive *N* according to *P'* and *K* according to the results of linear fractional transformation (LFT)

$$N = P_{11} + P_{12}K(I - P_{22}K)^{-1}P_{21} \tag{5.28}$$

Similiarlly, the closed-loop transfer function matrix *F* between the exogonous signal *w* and the error to be minimized *z*, can be written as

$$F = N_{22} + N_{21}\Delta(I - N_{11}\Delta)^{-1}N_{21} \tag{5.29}$$

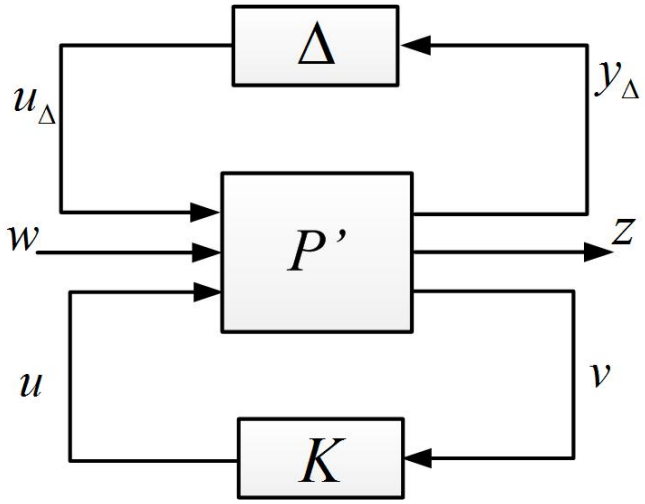

Figure 5.8: The General Control Structure.

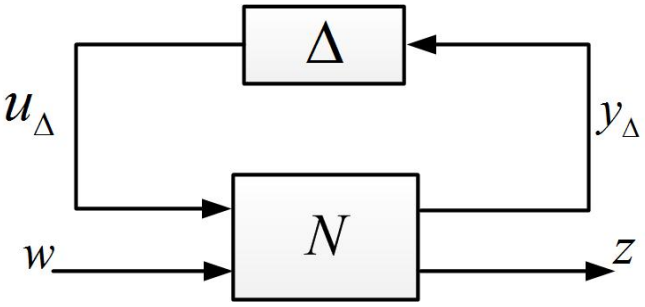

Figure 5.9: The $N\Delta$ Structure.

The necessary and sufficient conditions of NS, NP, RS, and RP can be stated based on the $N\Delta$ structure [56, 122]:

$$\begin{aligned} \text{NS} &\Leftrightarrow N \textit{ is internally stable} \\ \text{NP} &\Leftrightarrow \left\|N_{22}\right\|_\infty < 1; \ \textit{and} \ \text{NS} \\ \text{RS} &\Leftrightarrow F \textit{ is stable} \ \ \forall\Delta, \ \left\|\Delta\right\|_\infty \le 1; \textit{and} \ \text{NS} \\ \text{RP} &\Leftrightarrow \left\|F\right\|_\infty < 1, \ \ \forall\Delta, \ \left\|\Delta\right\|_\infty \le 1; \textit{and} \ \text{NS} \end{aligned} \tag{5.30}$$

Test Results of NS, NP, RS, and RP

The static controller K in (5.27) implies that a pole-zero cancellation is not possible. It is also found that all the poles of the nominal N are in the open left half of the complex plane. Therefore, the equilibrium point of the closed-loop system is nominally stable. The nominal performance test shows that $\bar{\sigma}(N_{22}) = 0.0328 < 1$. Therefore, the designed controller guarantees the nominal performance.

To test the stability of a system under perturbations, the perturbation results [83] or the small gain theorem [122] could be used. However, both of them would yield conservative results. The structured singular value, μ, provides necessary and sufficient conditions to test RS and RP [137]. The conservativeness could be eliminated through a structured singular value synthesis because the structure of Δ is considered. Recall the LFT result in (5.29), if N is internally stable, each part (N_{11}, N_{12}, N_{21}, and N_{22}) of N is stable. Therefore, unstable behavior would only be caused by $(I - N_{11}\Delta)^{-1}$ in (5.29). Then, the definition of μ can be introduced by

$$\mu(M) = \frac{1}{\min\left\{k_m \,\middle|\, \det(I - k_m M\Delta) = 0 \text{ for structured } \Delta,\ \bar{\sigma}(\Delta) \le 1\right\}}. \tag{5.31}$$

The μ-conditions for NP, RS, and RP are taken out from [56]:

$$\begin{aligned}
&\text{NS} \Leftrightarrow N \text{ is internally stable} \\
&\text{NP} \Leftrightarrow \bar{\sigma}(N_{22}) = \mu_{\Delta_P} < 1,\ \forall\omega, \text{ and NS} \\
&\text{RS} \Leftrightarrow \mu_{\Delta}(N_{11}) < 1,\ \forall\omega, \text{ and NS} \\
&\text{RP} \Leftrightarrow \mu_{\hat{\Delta}}(N) < 1,\ \forall\omega,\ \hat{\Delta} = \begin{bmatrix} \Delta & 0 \\ 0 & \Delta_P \end{bmatrix}, \text{ and NS}
\end{aligned} \tag{5.32}$$

where Δ_P is a full complex matrix does not have structure.

To calculate μ, the $M\Delta$ and $N\Delta$ structure [56] are derived. For instance, the $M\Delta$ structure can be derived according to the block diagram in Fig. 5.10. The $N\Delta$

structure can be conveniently generated by rearranging the $M\Delta$ structure. I consider more than six uncertainties to evaluate a closed-loop system subject to a more complicated uncertainty. In our analysis the diagonal uncertain matrix Δ is selected in the following form

$$\Delta = diag\left\{\Delta_{E_1} \quad \Delta_{E_1} \quad \Delta_{E_2} \quad \Delta_{E_2} \quad \Delta_{G_3} \quad \Delta_{G_4} \quad \Delta_{d_3} \quad \Delta_{d_3} \quad \Delta_{d_4} \quad \Delta_{d_4} \quad \Delta_{I_{L1}} \quad \Delta_{I_{L2}} \quad \Delta_{f_3} \quad \Delta_{f_4}\right\} \tag{5.33}$$

where $f_3 = G_3 d_3$ and $f_4 = G_4 d_4$. Note parametric uncertainties maybe repeated [56] as shown in (5.22). It shows that the RS can be satisfied for all admissible uncertainties because $\mu_{\Delta}(M) = 0.2104 < 1$. The RP test shows that $\mu_{\hat{\Delta}}(N) = 0.2346$. Therefore, the robust performance is also guaranteed. The test results of NP, RS, and RP are plotted with respect to frequency in Fig. 5.11.

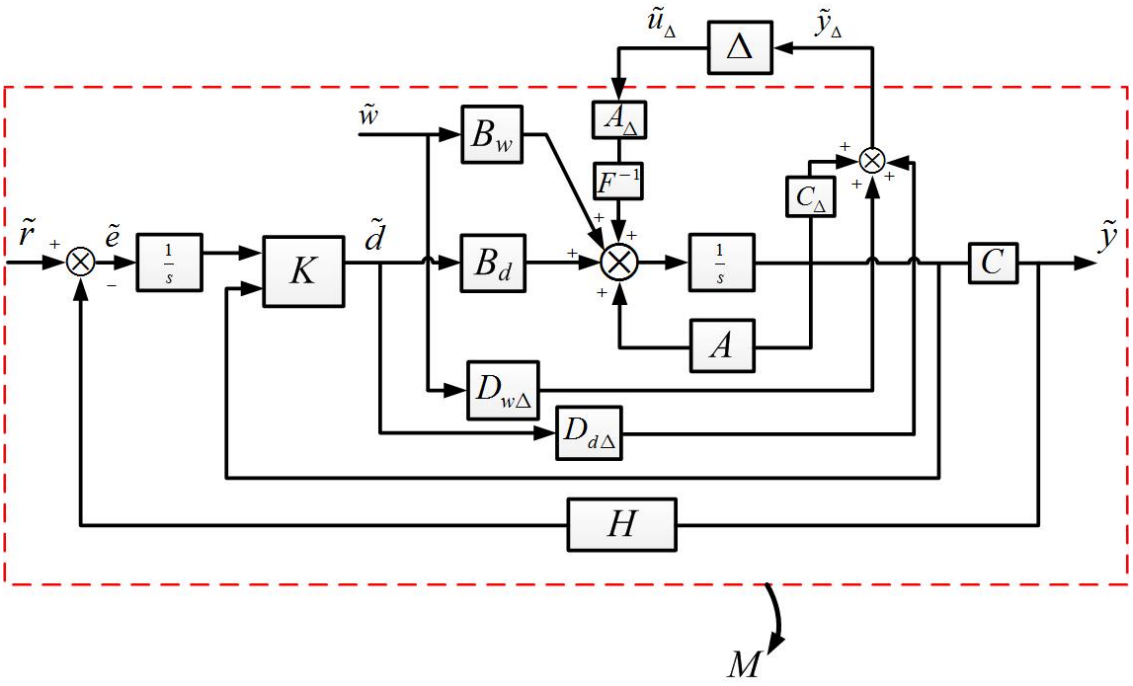

Figure 5.10: $M\Delta$-structure of the Controller Synthesis.

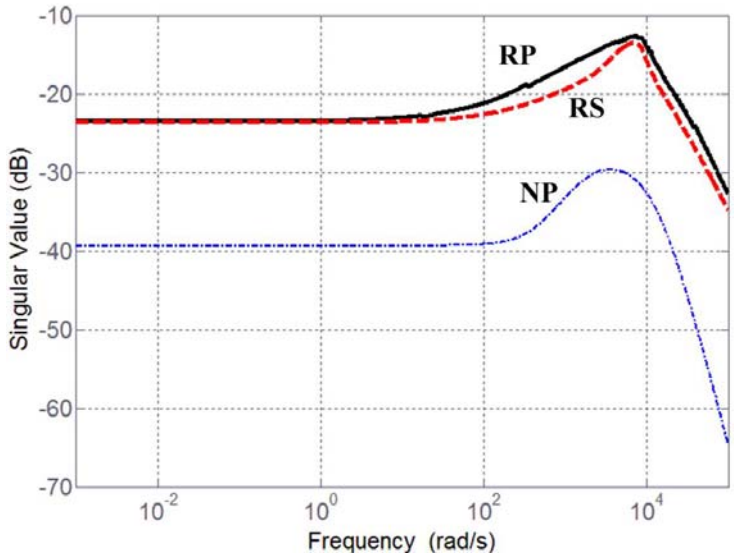

Figure 5.11: NP, RS, and RP Evaluation.

SIMULATED AND EXPERIMENTAL VERIFICATIONS OF THE ANALYSIS

Simulations

The designed controller K in (5.27) is implemented in both simulations to verify the stability and performance of the closed-loop system. Figures 5.13-5.15 show the simulation results of the closed-loop system through the Matlab/SIMULINK as described in Fig. 5.12.

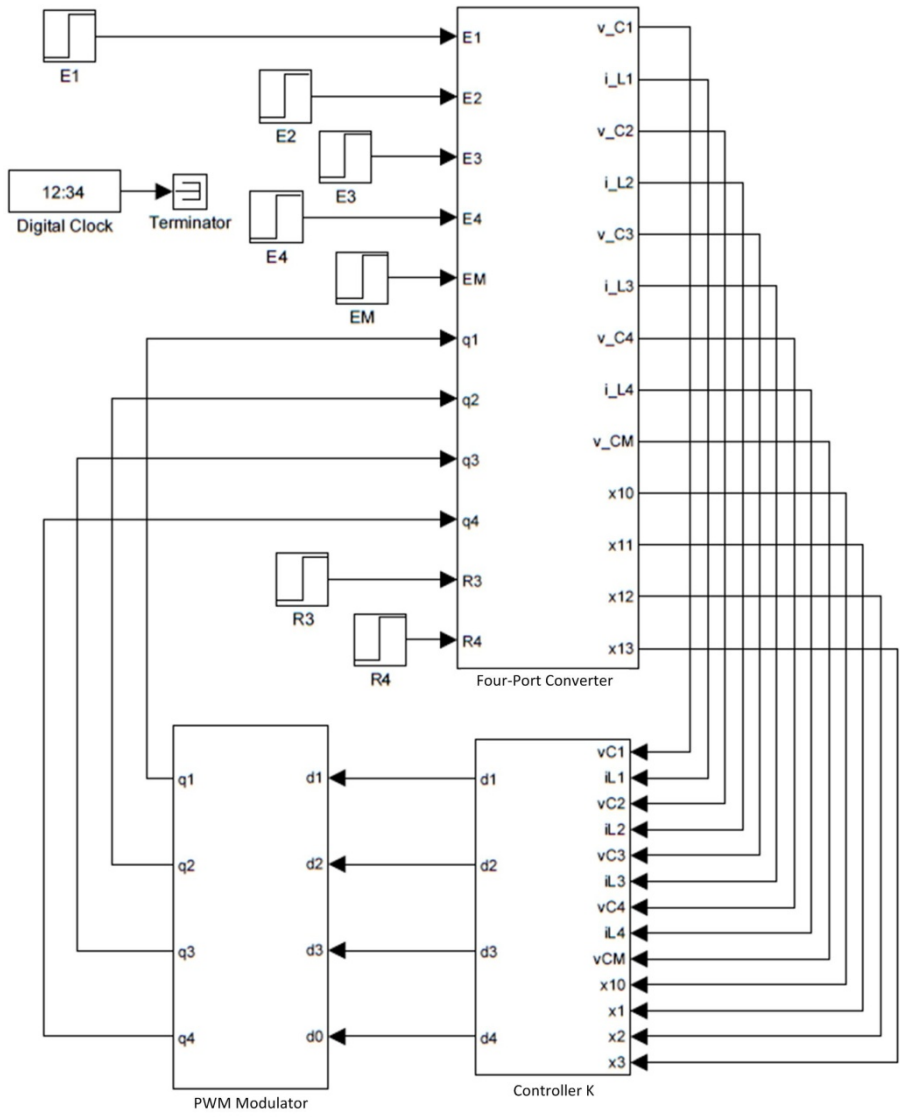

Figure 5.12: Closed-loop Simulation Scheme for Figs. 5.13-5.15.

All the parameters are kept the same as those in Table 6.. The input voltage E_1 , load resistance R_4 are kept to be 12.0 V, and 10.0 Ω, respectively. Figure 5.13 (a) shows that at $t = 0.06$ s, a disturbance in E_2 (from 15.0 V to 20.0 V) occurs in the I/O module #2. Due to the regulation action provided by the controller *K*, the outputs stay at the reference values. Moreover, good performance is observed in the outputs, therefore showing robust performance. Figure 5.13 (b), on the other hand, shows the successful

line regulation when E_2 decreases from 15.0 V to 10.0 V. Figures 5.7 (a) or (b) show that when load suddenly changes, the controller is still able to successfully regulate the outputs at the references. Again, the responses of the regulated outputs show good performance under load variations. Figures 5.14 (a) and (b) show the sucessful regulation when load changes. Therefore, the robust stability and performance of the closed-loop system is verified through simulation. The role of the battery is simulated. As shown in Fig. 5.15, the operation of the battery changes from charging to discharging, under a sudden load increase.

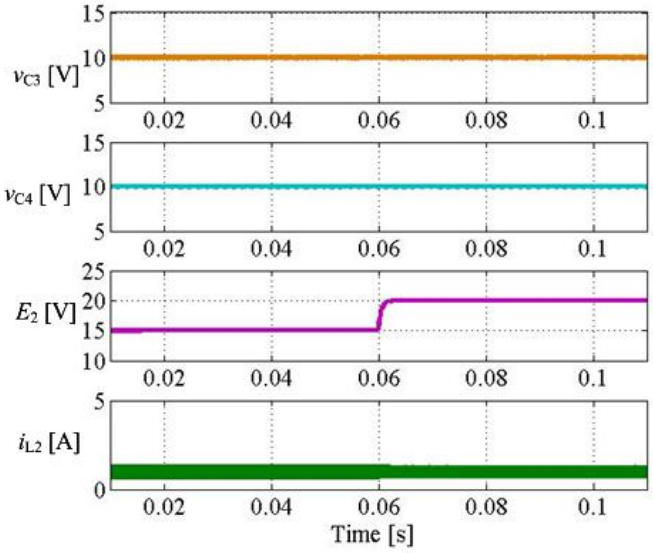

(a)

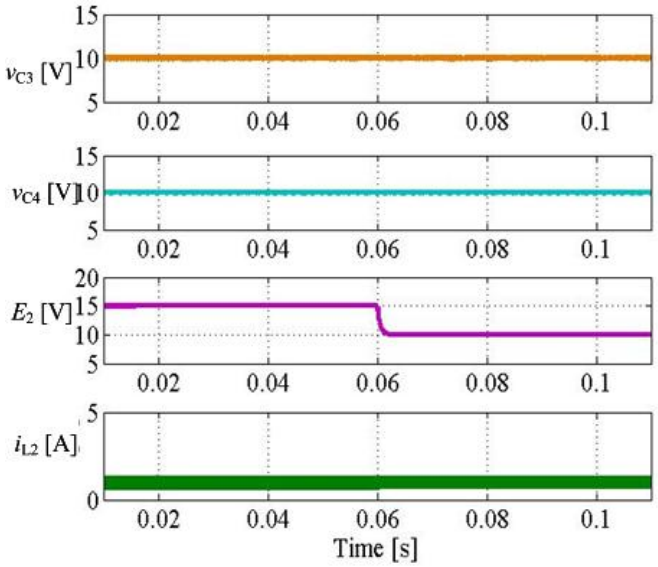

(b)

Figure 5.13: Simulated Results of Line Regulations. (a) E_2 Increases from 15.0 V to 20.0 V. (b) E_2 Decreases from 15.0 V to 10.0 V.

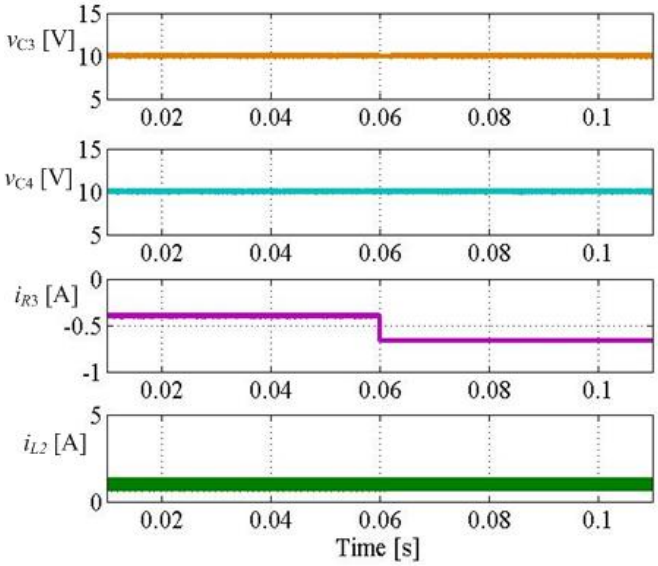

(a)

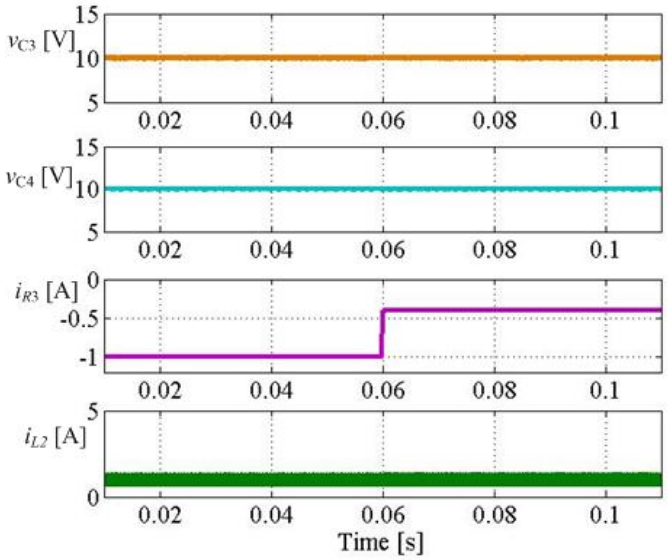

(b)

Figure 5.14: Simulated Results of Load Regulations. (a) R_3 Decreases from 25 Ω to 15 Ω. (b) R_3 Increases from 10 Ω to 25 Ω.

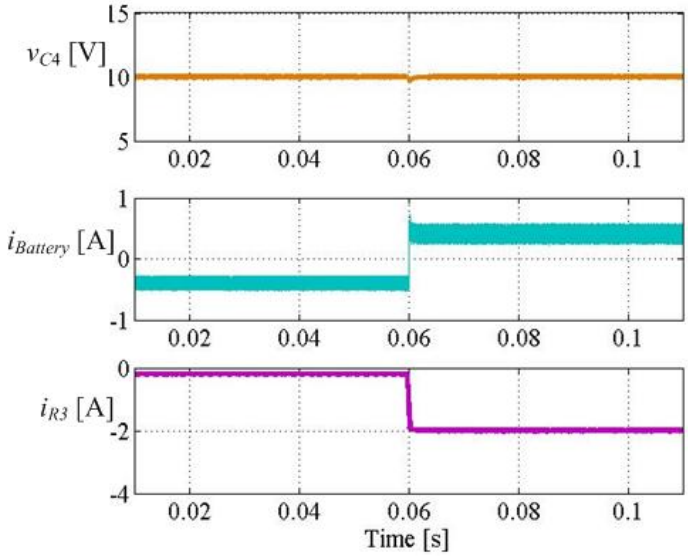

Figure 5.15: Battery Current Direction Change under Load Variation (Simulation Result).

Experiments

Following the simulated verification of the analysis, closed-loop operation was tested with experiments using a hardware prototype (Fig. 5.16). The parameters in the

experimental setup follow Table 6. The eight MOSFETs in four I/O modules are realized by FQA44N30, which are driven by four IR21844 H-bridge drivers. The battery is realized by a series connection of two PS-1250F1 12 V modules produced by Power-Sonic.

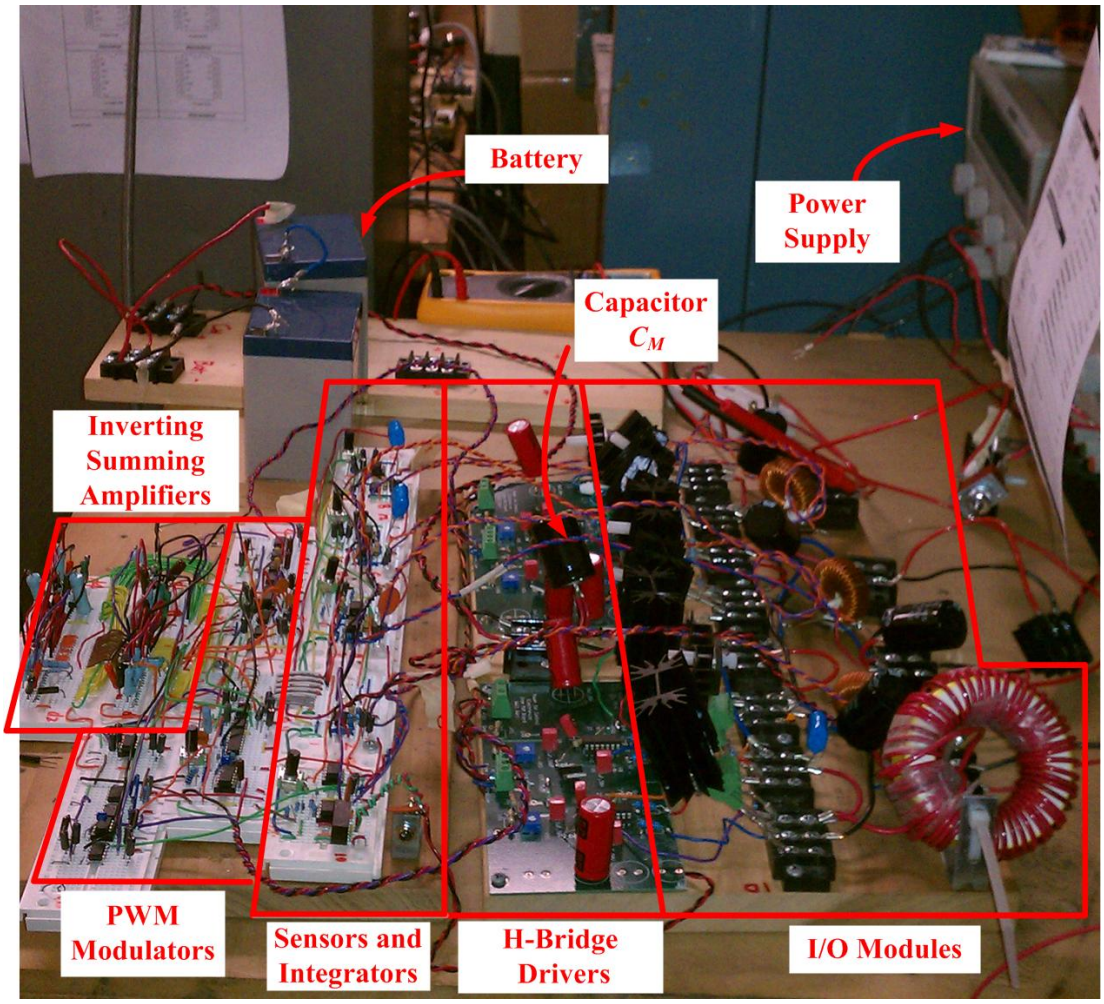

Figure 5.16: Prototype for the Verification of the Designed Controller K.

Resistor Design

Four inverting summing amplifiers are implemented to generator four control variables, d_1, d_2, d_3, and d_4, as shown in Fig. 5.17. In the prototype shown in Fig. 5.16, both state variables and their inverted version are generated for feedback. In Fig. 5.17, the +/- before each input indicates that the input of an inverting summing amplifier is

connected to a (scaled) state variable if it corresponds a positve gain; otherwise, the input is connected an inverted state variable. A small R_{i_out} should be avoided, because it may lead to small resistors drawing high currents from the previous stage. In this design, a $R_{i\_out} = 10\ \text{k}\Omega$ is selected.

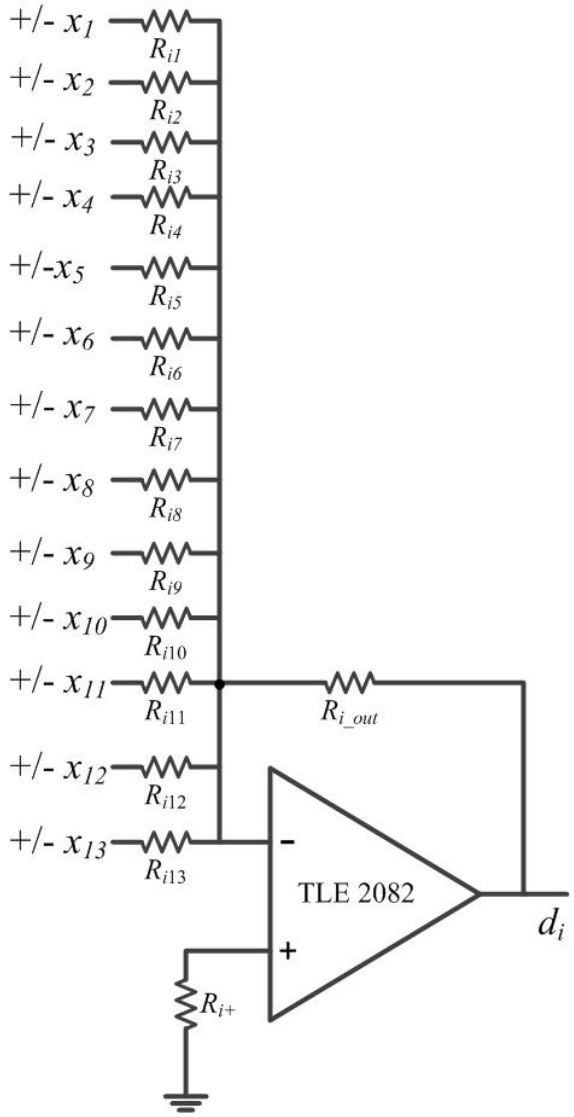

Figure 5.17: An Inverting Summing Amplifier.

The control implementation consists of multiple stages, including the sensors and integrators, the state-feedback controller, and the PWM modulators. The design of the

resistors in the state-feedback controller stage should consider of the gain introduced by all the stages. As shown in Table 7, to determine the resistors in Fig. 5.17, first, the gains of voltage sensors, current sensors, and error integrators are considered; second, the gain introduced by the PWM modulator stage is compensated by multiplying 3 (to match the peak voltage 3 V of the triangle carrier wave). The result after considering the PWM modulation stage (in the rows of "× gains of PWM modulators") is the gains need to be provided by the inverting summing amplifiers. Then, the values of the resistors can be calculated and the results can be found in Table 7. Again, the gains in Table 7 can be either positive or negative, which implies that a (scaled) state or its negative should be connected. The unit of the designed resistors is $\mathrm{k}\Omega$.

States	v_{C1}	i_{L1}	v_{C2}	i_{L2}	v_{C3}	i_{L3}	v_{C4}	i_{L4}	V_{CM}	$\int e_1 dt$	$\int e_2 dt$	$\int e_3 dt$	$\int e_4 dt$
Gains in (5.27) for d_1	-0.0367	-0.146	-0.0000507	0.0000540	0.0025036	0.0001883	0.0023016	0.0001884	0.0207750	211.56	-0.14097	-2.2587	-2.3942
÷ gains of sensors or integrators	-0.735	-0.146	-0.001	0.0000540	0.050	0.000	0.046	0.000	0.416	2.116	-0.001	-0.023	-0.024
× gains of PWM modulators	-2.205	-0.437	-0.003	0.000	0.150	0.001	0.138	0.001	1.247	6.347	-0.004	-0.068	-0.072
Designed resistors	-4.535	-22.889	-3284.461	61721.537	66.571	17705.069	72.413	17695.670	8.022	1.576	-2364.569	-147.578	-139.225
Gains of in (5.27) for d_2	0.00006	0.00003	-0.03675	-0.14568	0.00243	0.00019	0.00233	0.00018	0.02078	-0.13680	211.57	-2.11590	-2.44340
÷ gains of sensors or integrators	0.00113	0.00003	-0.73506	-0.14568	0.04869	0.00019	0.04665	0.00018	0.41550	-0.00137	2.11570	-0.02116	-0.02443
× gains of PWM modulators	0.00339	0.00009	-2.20518	-0.43704	0.14607	0.00057	0.13996	0.00053	1.24650	-0.00410	6.34710	-0.06348	-0.07330
Designed resistors	-2948.4	111849.317	-4.535	-22.881	68.460	17451.093	71.448	18712.925	8.022	-2436.647	1.576	-157.537	-136.422
Gains in (5.27) for d_3	0.001	0.008	0.001	0.007	0.985	-0.182	0.019	-0.001	0.014	0.275	0.999	-1299.9	-53.337
÷ gains of sensors or integrators	0.013	0.008	0.014	0.007	19.706	-0.182	0.379	-0.001	0.277	0.003	0.010	-12.999	-0.533
× gains of PWM modulators	0.039	0.023	0.043	0.022	59.119	-0.547	1.136	-0.004	0.830	0.008	0.030	-38.997	-1.600
Designed resistors	255.836	438.060	235.249	464.712	0.169	-18.298	8.802	-2788.934	12.050	1211.813	333.563	-0.256	-6.250
Gains in (5.27) for d_4	0.001	0.007	0.001	0.007	0.021	-0.001	0.983	-0.177	0.014	0.375	-0.235	-46.057	-1273.3
÷ gains of sensors or integrators	0.012	0.007	0.011	0.007	0.421	-0.001	19.655	-0.177	0.277	0.004	-0.002	-0.461	-12.733
× gains of PWM modulators	0.035	0.020	0.033	0.022	1.264	-0.002	58.966	-0.532	0.832	0.011	-0.007	-1.382	-38.199
Designed resistors	282.769	498.085	304.258	458.291	7.911	-4250.400	0.170	-18.780	12.015	889.672	-1417.475	-7.237	-0.262

Table 7: Design of Resistors in the Proposed State-feedback Controller (R_{i_out}=10 kΩ).

Experimental Results

The experimental results under the same conditions in the simulations shown in Figs. 5.13 to 5.15 are presented in Figs. 5.18 to 5.20.

With $E_1 = 12$ V, $R_3 = 25\ \Omega$, and $R_4 = 10\ \Omega$, Fig. 5.18 (a) and (b) show that when the input voltage E_2 suddenly increases (from 15 V to 20 V) or decreaes (from 15 V to 10 V), the equilibrium point of closed-loop system stays stable and all the outputs are regulated. With $E_1 = 12$ V, $E_2 = 15$ V, and $R_4 = 10\ \Omega$, Fig. 5.19 (a) and (b) present load regulation. Once again, the closed-loop system is stable and all the outputs are regulated. Finally, with $E_1 = 12$ V, $E_2 = 15$ V, and $R_4 = 10\ \Omega$. Thus, the RS and RP are both verified through experimental results. Fig. 5.20 shows the role of the power buffer E_M. Initially, R_3 is 50 Ω and all the outputs are regulated. Since the load is relatively small, it is not consuming the power that is comanded to be generated by the input sources. Thus, the remaining power is stored at the energy storage device E_M. When R_3 decreases to 5 Ω, the input power becomes insufficient to supply the loads, so they now draw power from the battery.

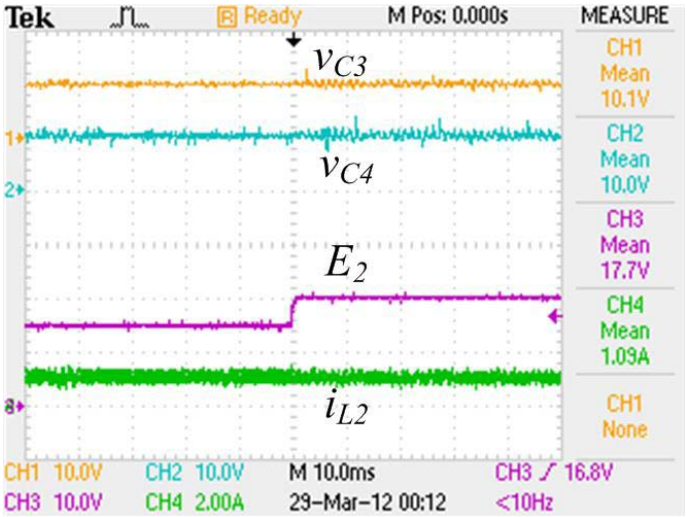

(a)

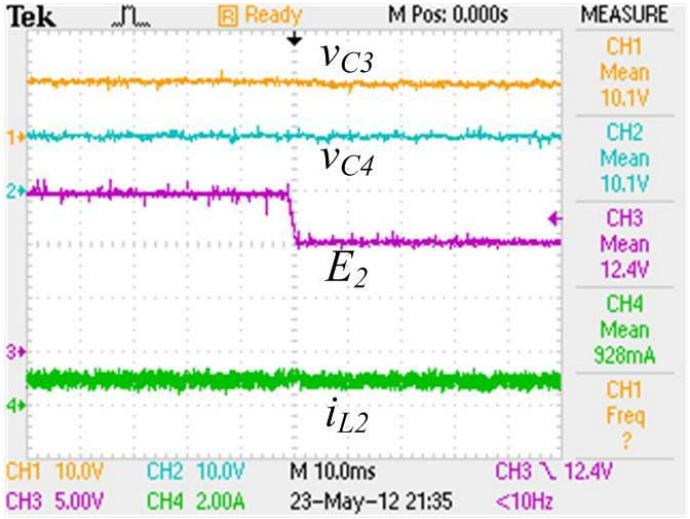

(b)

Figure 5.18: Line Regulation. (a) E_2 Increases from 15.0 V to 20.0 V. (b) E_2 Decreases from 15.0 V to 10.0 V.

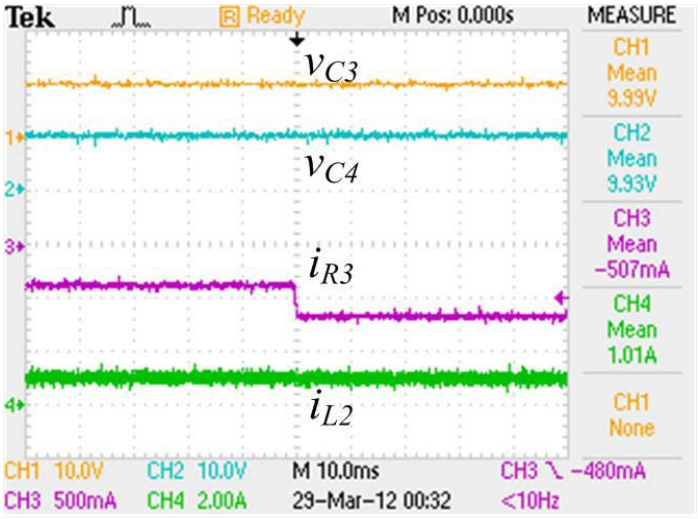

(a)

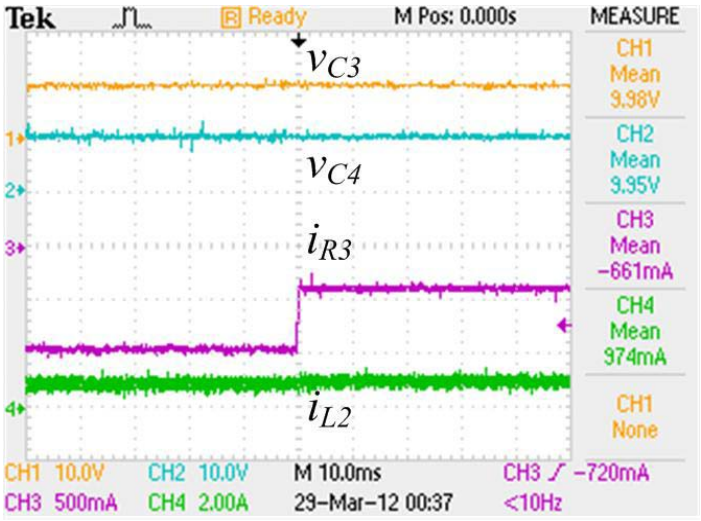

(b)

Figure 5.19: Load Regulation. (a) R_3 Decreases from 25 Ω to 15 Ω. (b) R_3 Increases from 10 Ω to 25 Ω.

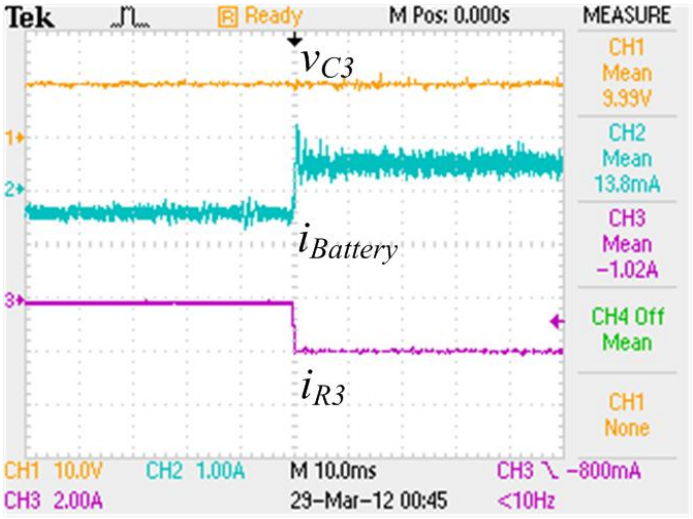

Figure 5.20: The Battery Current Direction Change under Load Variation (Experimental Result).

Reponses under More Complicated Disturbances

In the previous subsection, responses under single disturbance has been test in simulations and experiments. In this subsection, responses under more complicated

disturbances are analyzed and simulated. The robust H_∞ controller K minimizes the "worst" response of disturbance under all admissible uncertainties. Since it would be tedious to investigated systems responses with all allowable δ, a nominal plant is considered for analysis ease. The parameters of the nominal plant are configured as follows: $E_1 = E_2 = 15$ V, $R_3 = R_4 = 20$ Ω, $E_M = 25.0$ V, and $d_3 = d_4 = 0.6$.

1. The "Worst" Disturbance

The simulated result aims for giving insights into that if a good performance can be achieved in the presence of a worst-case disturbance. The first step is find the "worst" disturbances.

SISO Systems: In a conventional SISO control system, a disturbance is worst if the frequency of the disturbance yields the largest amplifying gain. Limitations may be caused when the magnitude of disturbance-to-output transfer function $G_w(s)$ is larger than 1. Control actions should be taken to address the limitations caused by a large $G_w(s)$.

Multivariable Control Systems: In a multivariable control system, both the direction and the frequency need to be considered when determine the worst case, that is, $G_w(s)$ is maximized in magnitude. The worst condition can be found by the singular value decomposition (SVD) with respect to frequency.

The scaled disturbance-to-output transfer function matrix $G_w(s)$ is used for analysis. Then, the Matlab function "sigma" is used and the result of SVD is plotted in Fig. 5.21. It is found in Fig. 5.21 that the worst frequency is zero because the largest singular value of $G_w(s)$ (with respect to frequency) occurs in low frequencies. This observation would justify the consideration of the H_∞ constraint in the controler design for the power router because power electronics circuits usually subject to low frequency

disturbances so a large gain in disturbances is relatively easy to happen. However, for plants those that the worst case rarely or never takes place, an H_∞ control may become conservative. Other controller design techniques which consider different operating regions—e.g., a gain scheduling controller—or that allow for online update law—e.g., an adaptive control may achieve better performance.

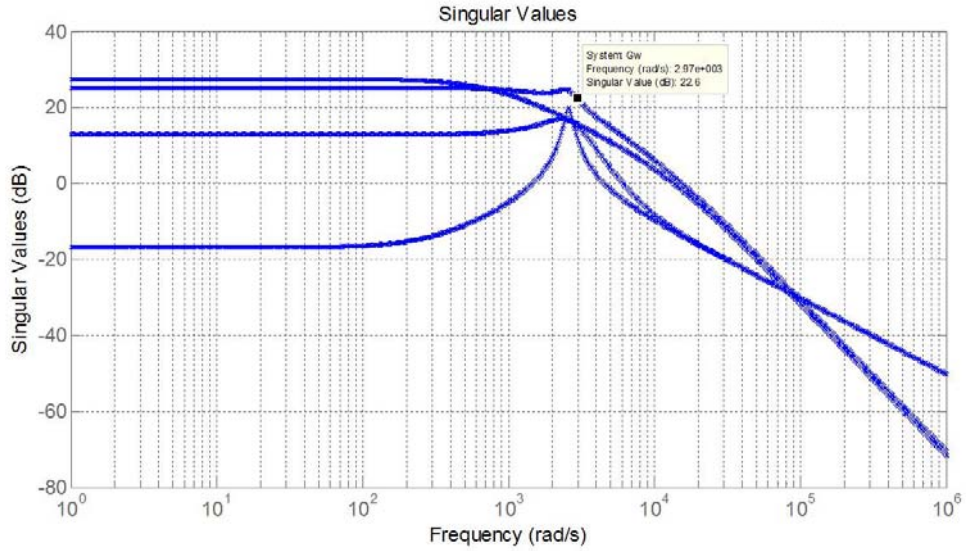

Figure 5.21: The Singular Values of $G_w(s)$ with Respect to Frequency

Then, the next question becomes that what is the worst input direction that leads to the largest singular value $\bar{\sigma}\left(G_w(s)\right)$. The dc gain of $G_w(0)$ is calculated in (5.30)

$$G_w(0) = \begin{bmatrix} 18.153 & -5.8474 & -0.3582 & -0.3582 & -9.8441 \\ -5.8474 & 18.153 & -0.3582 & -0.3582 & -9.8441 \\ 1.4619 & 1.4619 & 0.23654 & 0.089539 & 2.461 \\ 1.4619 & 1.4619 & 0.089539 & 0.23654 & 2.461 \end{bmatrix} \tag{5.34}$$

The dc gain of $G_w(0)$ in (5.30) shows that the entries associated with the voltages (E_1, E_2, and E_M) are large in magnitude and require control action. The SVD of $G_w(0)$ is calculated by

$$G_w(0) = U\Sigma V^T \tag{5.35}$$

where

$$U = \begin{bmatrix} 0.707 & -0.707 & -0.0276 & 0 \\ -0.707 & -0.707 & -0.0276 & 0 \\ 0 & 0.0276 & -0.707 & -0.707 \\ 0 & 0.0276 & -0.707 & 0.707 \end{bmatrix},$$

$$\Sigma = \begin{bmatrix} 24 & 0 & 0 & 0 & 0 \\ 0 & 18.608 & 0 & 0 & 0 \\ 0 & 0 & 4.5024 & 0 & 0 \\ 0 & 0 & 0 & 0.147 & 0 \end{bmatrix},$$

$$V^T = \begin{bmatrix} 0.707 & -0.463 & -0.534 & 0 & 0.0173 \\ -0.707 & -0.463 & -0.534 & 0 & 0.0173 \\ 0 & 0.0277 & -0.0468 & -0.707 & -0.705 \\ 0 & 0.0277 & -0.0468 & 0.707 & -0.705 \\ 0 & 0.755 & -0.652 & 0 & 0.0729 \end{bmatrix}^T.$$

The SVD result of $G_w(0)$ verifies the plot in Fig. 5.21. For example, the largest gain is $20\ln 24 = 27.6\,\text{dB}$, which is equal to the largest gain in the log-log plot in Fig. 5.21. The largest singular value $\bar{\sigma}(G_w(s)) = \bar{\sigma}(G_w(0)) = 24$ is caused by a disturbance in the direction represented by

$$\bar{v} = \begin{bmatrix} 0.707 \\ -0.707 \\ 0 \\ 0 \\ 0 \end{bmatrix},$$

which leads to an output in the direction

$$\bar{u} = \begin{bmatrix} 0.707 \\ -0.707 \\ 0 \\ 0 \end{bmatrix}.$$

Therefore, according to the direction of $\bar{v}$, the worst condition can be simulated by introducing $\tilde{E}_1 = 5$ V and $\tilde{E}_1 = -5$ V while $\tilde{G}_3 = \tilde{G}_4 = \tilde{E}_M = 0$ to construct a worst disturbance.

The simulation results in Fig. 5.22 show that the closed-loop system stays stable and control is effective to attenuate the responses of the worst disturbance. The variations in the output voltages v_{C3} and v_{C4} are negligible, which verifies the zero entries in $\bar{u}$ corresponding to the output voltages. It is also revealed by $\bar{u}$ that the worst disturbance leads to responses in both inductor currents I_{L1} and I_{L2}. According to simulated waveform shown in Fig. 5.22, the performance is good because the overshoot and undershoot of the inductor currents are small. Thanks to the satisfaction of the pole-placement constraints, the closed-loop poles are placed in a specified region to guarantee a fast response, hence, the durations of inductor current transients are short. The waveform of the battery current includes high order harmonics because the transients in all I/O modules are selected in the buffering stage.

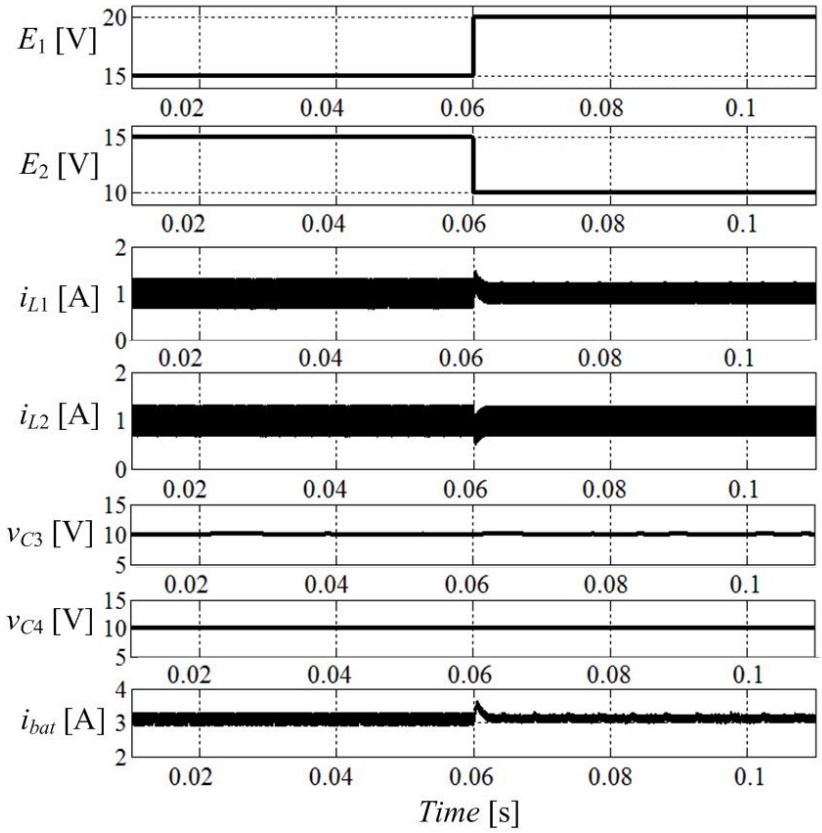

Figure 5.22: Simulated Response when the Worst Disturbance Occurs

2. A Large Disturbance

In the previous simulation of the worst disturbance, only two disturbances originated in line voltages occur simultaneously. It might be of interest to test the response of a large disturbance when every single disturbance occurs simultaneously with its largest magnitude. In here, the following condition is simulated:

E_1 suddenly increases from 10 V to 20 V, E_2 suddenly increases from 10 V to 20 V, R_3 suddenly decreases from 50 Ω to 5 Ω, R_4 suddenly increases from 5 Ω to 50 Ω, and E_M stays at 25.0 V. The battery voltage is kept unchanged because the variation in E_M is typically slower comparing to changes in line voltages and loads. The simulation result is presented by Fig. 5.23.

It is shown in Fig. 5.23 that when the large disturbance is introduced, the closed-loop system stays stable and all the outputs are regulated at their references. Although variations are found in all of the four outputs, the overshoots and undershoots are small. In addition, the transients damp out quickly due to the pole-placement. The closed-loop system still maintain good performance with such a large disturbance, which verifies the effectiveness in suppressing the disturbance provided by the H_∞ controller. Again, the battery current direction changes, due to the mismatches between input and output power.

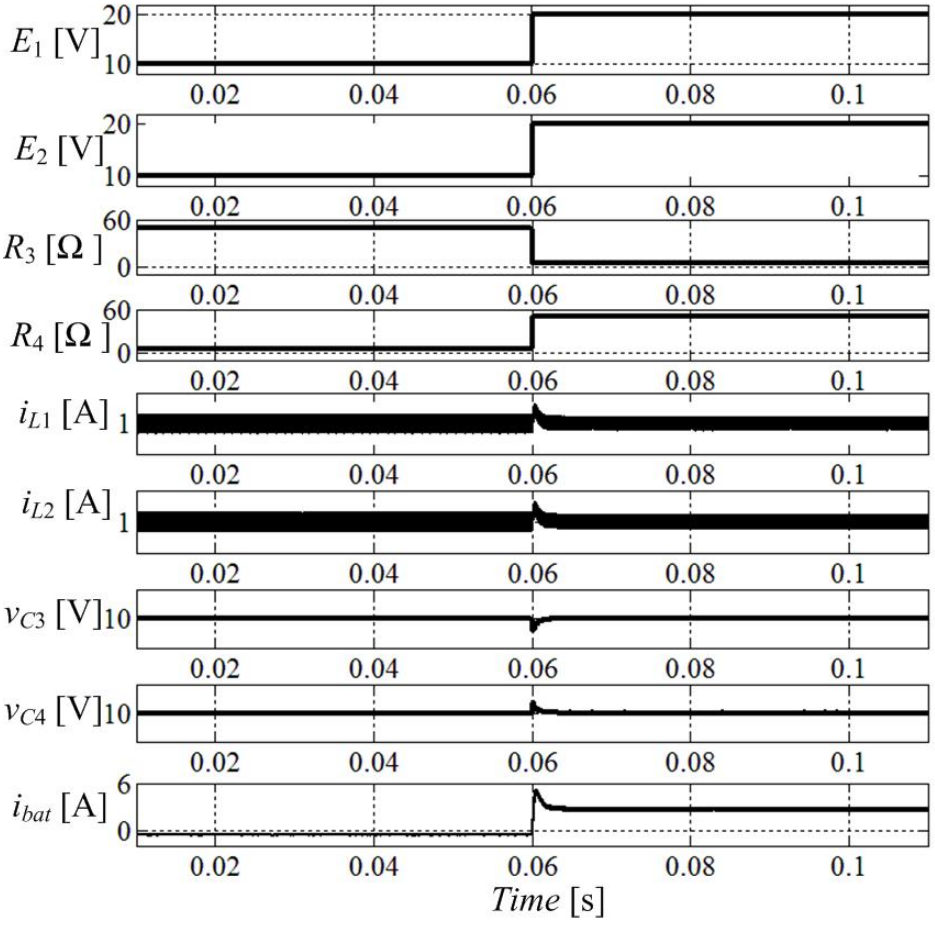

Figure 5.23: Simulated Response when a Large Disturbance Occurs

2. Repeated Disturbances

The response under repeated multiple disturbances with large magnitude is also simulated. Again, robust stability and good closed-loop performance are observed under large, repeated disturbances. The simulated responses are sown in Fig. 5.24.

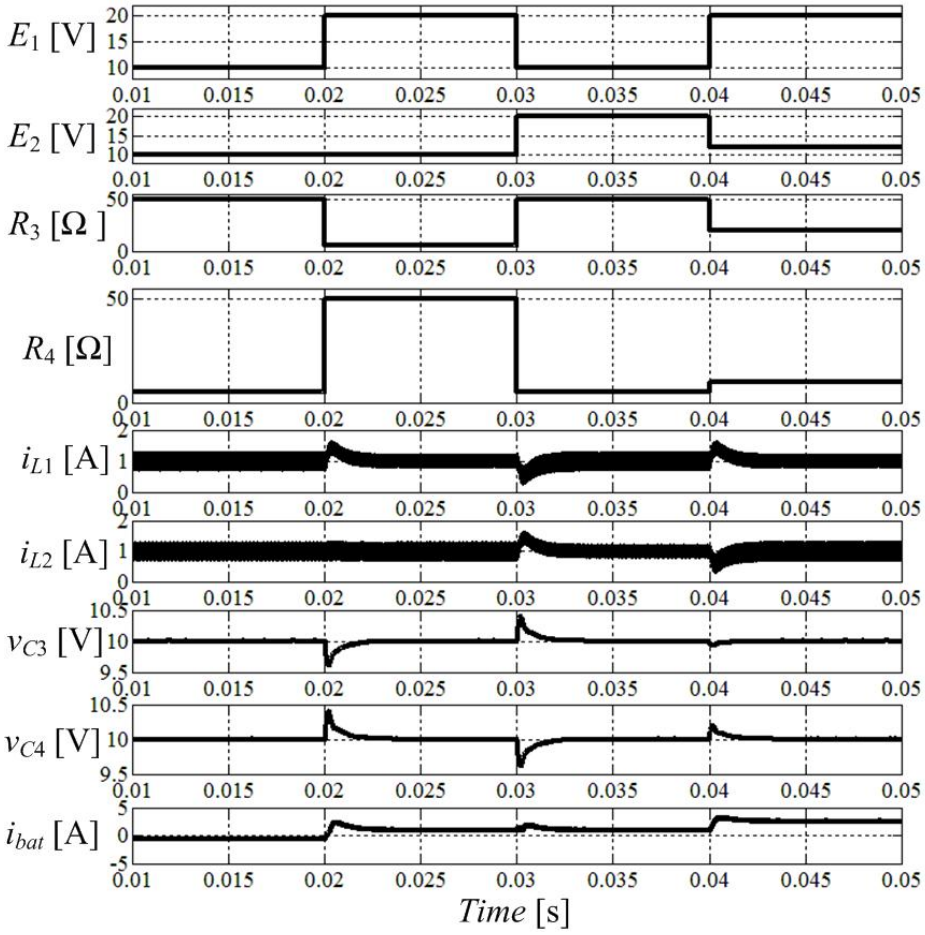

Figure 5.24: Simulated Response when a Repeated Disturbance Occurs

Chapter 6: Conclusions

This dissertation has discussed various aspects of multiport converters. The main focuses are key issues in multiple-input topologies: efficiency improvement, modeling, and control.

The advantages of MICs include the reduced cost and enhanced availability in, for example, dc distribution systems. One issue of MICs, especially those that contain forward-conducting-bidirectional-blocking (FCBB) switches, is that they typically have low power conversion efficiencies. This work starts from proposing a novel design to improve the efficiency of a non-isolated multiple-input (MI) SEPIC. Unlike previous work which takes advantage of an auxiliary circuit to improve efficiency, this work modifies the design from a brand-new perspective—to improve the switching transients through modifying the time-multiplexing switching functions. Despite the presence of FCBB switches, the MI-SEPIC can achieve efficiencies sufficiently high for dc micro-grid applications as experimental results have shown. With this modified design, the MI-SEPIC may become one of the most efficient MIC topologies. Additionally, since the modular design is not compromised and an auxiliary circuit is not required, this design maintains other important characteristic benefits of MICs—low cost/parts-count and high availability.

The second part of this work addresses the modeling issue of time-multiplexing multiple input converters (TM-MICs). Assuming dominant dc segments, classical modeling methods usually fail to yield a model with enough accuracy for TM-MICs. As presented by the switched dynamic equations of a TM-MIC, the time-multiplexing switching function and the coupling effect are identified to affect the behavior of this type of MICs. In this work, the generalized averaging method was applied successfully on the

modeling of an MI-SEPIC. Moreover, a modified reduced order model with the same order as the state-space averaging (SSA) model was achieved by a select modal analysis. The proposed models show improved accuracy comparing to the SSA model.

The final part of this dissertation studies the control of multiple-input converters. Chapter 4 studies the control of a multiple-input converter by a simple decentralized PI controller. The discussion is motivated through an MI-SEPIC, too. Without neglecting any cross interactions, several analysis techniques for multivariable control systems are used to assess the nominal stability, nominal performance, robust stability, and robust performance of the closed-loop system. The uncertainty analysis reveals a limitation in performance with the decentralized control. All the simulated and experimental results verify the theoretical analysis and also demonstrate that line and load regulation can be achieved in a satisfactory way with decentralized PI control. To address the limitation of the decentralized control, Chapter 5 presents a general framework for controller design and synthesis of multiple-input-multiple-output (MIMO) converters or MICs. First, a unified model independent of the inductor current directions of an MIMO boost-and-buck converter is derived. Second, since the MIMO converters are multivariable control systems, this work finds the necessity to perform a multivariable controller design to address the limitations of decentralized controllers typically used for these types of converters in previous work. This dissertation proposes to implement a robust state feedback controller that quadratically stabilizes the converter model while satisfying the H_∞ norm—for disturbance-attenuation—and pole-placement constraints—for time-domain response. The controller design problem is identified to be equivalent to an optimization problem, which can be converted to a finite number of linear matrix inequalities (LMIs). The numerical LMI-solver such as the YALMIP allows for solving the controller design problem efficiently. Third, the nominal stability (NS), nominal

performance (NP), robust stability (RS), and robust performance (RP) are evaluated. The analysis of RS and RP through the singular value synthesis shows that both specifications are met by the designed controller. Finally, the analysis of the stability and performance is verified by the simulations and experimental results.

Appendices

This appendices record the MATLAB code and supporting material used in this dissertation.

APPENDIX A. MULTI-FREQUENCY MODELING OF THE MI-SEPIC

Appendix A contains the MATLAB code for the multi-frequency modeling of the MI-SEPIC shown in Fig. 1.9.

MATLAB Code

```
clear all;
clc

D1=0.3; D2eff=0.3; D2=D1+D2eff; DD=1-D1-D2eff;
L1=320e-6; L2=320e-6;L3=320e-6;
C1=34e-6;C2=34e-6;C3=1200e-6;R=10;
rL1=0.009; rL2=0.007;rL=0.016; rC1=0.0776;
rC2=0.0782;rC=0.0467;rsw1=0.00;rsw2=0.00;rfd1=0.00;rfd2=0.00;rfd3=0.00;
vfd1=0;vfd2=0;vfd3=0;


E1=55.8/2;E2=26/2;

A1=[0         0          0        0           0          0;
    0         0          0        1/L2       -1/L2        0;
    0         0          0        1/L3         0          0;
    0        -1/C1      -1/C1     0           0            0;
    0         1/C2       0        0           0          0;
    0         0          0        0           0        -1/(R*C3)];
B1=[1/L1    0       0;
    0       1/L2     0;
    0        0       0;
    0        0       0;
    0        0       0;
    0        0         -1/C3];

A2=[0        0          0       -1/L1        1/L1      0;
   0         0         0         0          0         0;
   0         0         0         0         1/L3       0;
   1/C1      0          0        0          0         0;
  -1/C2      0        -1/C2       0          0           0;
   0         0          0        0          0         -1/(R*C3)];
B2=[1/L1    0     0;
```

```
   0    1/L2     0;
   0    0        0;
   0    0        0;
   0    0        0;
   0    0        -1/C3];

A3=[0         0          0       -1/L1         0         -1/L1;
   0          0          0         0          -1/L2      -1/L2;
   0          0          0         0           0         -1/L3;
   1/C1       0          0         0           0          0;
   0         1/C2        0         0           0          0;
   1/C3      1/C3       1/C3       0           0        -1/(R*C3)];
B3=[1/L1    0     0;
   0    1/L2     0;
   0    0        0;
   0    0        0;
   0    0        0;
   0    0      -1/C3];

f=40000; % switching frequency
fi1=D1/2*2*pi;
fi2=(D1+D2eff/2)*2*pi;
fi3=(D1+D2eff+DD/2)*2*pi;

q1_0=D1;
q1_1=(1/(2*pi*1*j))*(1-exp(-2*pi*1*j*D1));
q1_m1=conj(q1_1);
q1_2=(1/(2*pi*2*j))*(1-exp(-2*pi*2*j*D1));
q1_m2=conj(q1_2);
q1_1_r=real(q1_1);
q1_1_i=imag(q1_1);

q2_0=D2eff;
q2_1=(1/(2*pi*1*j))*(1-exp(-2*pi*1*j*D2eff))*exp(-j*(fi2-pi*D2eff));
q2_m1=conj(q2_1);
q2_2=(1/(2*pi*2*j))*(1-exp(-2*pi*2*j*D2eff))*exp(-j*(2*fi2-2*pi*D2eff));
q2_m2=conj(q2_2);
q2_1_r=real(q2_1);
q2_1_i=imag(q2_1);

qD_0=DD;
qD_1=(1/(2*pi*1*j))*(1-exp(-2*pi*1*j*DD))*exp(-j*(fi3-pi*DD));
qD_m1=conj(qD_1);
qD_2=(1/(2*pi*2*j))*(1-exp(-2*pi*2*j*DD))*exp(-j*(2*fi3-2*pi*DD));
qD_m2=conj(qD_2);
qD_1_r=real(qD_1);
qD_1_i=imag(qD_1);

w=2*pi*f;

%A11 matrix
A11=[-0.08/L1 -0.04/L1 -0.046/L1 -(1-D1)/L1 (D2-D1)/L1 -DD*(1-rC/R)/L1;
```

```
-0.04/L2  -0.08/L2  -0.046/L2  D1/L2  -(1+D1-D2)/L2    -DD*(1-rC/R)/L2;

-0.046/L3  -0.046/L3  -0.072/L3  D1/L3  (D2-D1)/L3     -DD*(1-rC/R)/L3;

(1-D1)/C1  -D1/C1  -D1/C1    0          0              0;

(D1-D2)/C2  (1+D1-D2)/C2  (D1-D2)/C2      0          0   0 ;

(1-D2)/C3   (1-D2)/C3    (1-D2)/C3       0    0        -1/(R*C3)];

%A12 matrix
A12=[-0.08/L1     -0.08/L1      -0.04/L1   -0.04/L1        -0.046/L1
-0.046/L1       (-2*q2_1_r-2*qD_1_r)/L1  (-2*q2_1_i-2*qD_1_i)/L1
(2*q2_1_r)/L1          2*q2_1_i/L1          -2*qD_1_r/L1    -2*qD_1_i/L1;

-0.04/L2    -0.04/L2      -0.08/L2    -0.08/L2       -0.046/L2 -0.046/L2
2*q1_1_r/L2  2*q1_1_i/L2 (-2*q1_1_r-2*qD_1_r)/L2 (-2*q1_1_i-2*qD_1_i)/L2
-2*qD_1_r/L2    -2*qD_1_i/L2;

-0.046/L3     -0.046/L3      -0.046/L3    -0.046/L3        -0.072/L3
-0.072/L3          2*q1_1_r/L3           2*q1_1_i/L3
2*q2_1_r/L3             2*q2_1_i/L3           -2*qD_1_r/L3    -2*qD_1_i/L3;

-2*q1_1_r/C1  -2*q1_1_i/C1  -2*q1_1_r/C1   -2*q1_1_i/C1    -2*q1_1_r/C1
-2*q1_1_i/C1    0     0    0     0    0     0;

-2*q2_1_r/C2  -2*q2_1_i/C2  -2*q2_1_r/C2   -2*q2_1_i/C2    -2*q2_1_r/C2
-2*q2_1_i/C2    0     0     0     0      0           0;

2*qD_1_r/C3   2*qD_1_i/C3   2*qD_1_r/C3    2*qD_1_i/C3     2*qD_1_r/C3
2*qD_1_i/C3     0       0       0      0      0      0;];

%A21 matrix
A21=[-0.08/L1    -0.04/L1     -0.046/L1          (-q2_1_r-qD_1_r)/L1
q2_1_r/L1        -qD_1_r/L1;

-0.08/L1    -0.04/L1     -0.046/L1         (-q2_1_i-qD_1_i)/L1
q2_1_i/L1        -qD_1_i/L1;

-0.04/L2     -0.08/L2     -0.046/L2  (q1_1_r)/L2   (-q1_1_r-qD_1_r)/L2
(-qD_1_r)/L2;

-0.04/L2 -0.08/L2 -0.046/L2 (q1_1_i)/L2 (-q1_1_i-qD_1_i)/L2
(-qD_1_i)/L2;

-0.046/L3   -0.046/L3   -0.072/L3   (q1_1_r)/L3    q2_1_r/L3    -qD_1_r/L3;

-0.046/L3     -0.046/L3   -0.072/L3  (q1_1_i)/L3   q2_1_i/L3    -qD_1_i/L3;
 -q1_1_r/C1     -q1_1_r/C1     -q1_1_r/C1    0           0           0;

 -q1_1_i/C1     -q1_1_i/C1     -q1_1_i/C1   0    0     0;

-q2_1_r/C2     -q2_1_r/C2     -q2_1_r/C2  0      0    0;
```

```
-q2_1_i/C2     -q2_1_i/C2     -q2_1_i/C2  0      0     0;

qD_1_r/C3       qD_1_r/C3     qD_1_r/C3   0      0     0;

qD_1_i/C3       qD_1_i/C3     qD_1_i/C3   0      0     0;];

%A22 matrix
A22=[ -0.08/L1    w-0.08/L1      -0.04/L1   -0.04/L1       -0.046/L1
-0.046/L1       (-q2_0-qD_0)/L1            0               q2_0/L1
0                 -qD_0/L1       0;

-w-0.08/L1     -0.08/L1      -0.04/L1   -0.04/L1        -0.046/L1
-0.046/L1          0             (-q2_0-qD_0)/L1         0
q2_0/L1             0              -qD_0/L1;

-0.04/L2    -0.04/L2      -0.08/L2    -0.08/L2+w       -0.046/L2
-0.046/L2    q1_0/L2         0  (-q1_0-qD_0)/L2   0    -qD_0/L2       0;

-0.04/L2    -0.04/L2      -0.08/L2-w    -0.08/L2       -0.046/L2
-0.046/L2            0                q1_0/L2             0
(-q1_0-qD_0)/L2    0          -qD_0/L2;

-0.046/L3     -0.046/L3      -0.046/L3    -0.046/L3        -0.072/L3
-0.072/L3+w          q1_0/L3                0                q2_0/L3
0            -qD_0/L3       0;

-0.046/L3     -0.046/L3      -0.046/L3    -0.046/L3         -0.072/L3-w
-0.072/L3          0                    q1_0/L3              0
q2_0/L3           0          -qD_0/L3;

(1-q1_0)/C1  0  (-q1_0)/C1  0  (-q1_0)/C1  0  0  w  0  0  0  0;

0  (1-q1_0)/C1  0     (-q1_0)/C1  0    (-q1_0)/C1    -w     0  0  0  0  0;

(-q2_0)/C2  0  (1-q2_0)/C2  0  (-q2_0)/C2  0  0  0  0   w  0   0;

0  (-q2_0)/C2  0  (1-q2_0)/C2  0  (-q2_0)/C2   0  0   -w   0  0  0;

(qD_0)/C3  0  (qD_0)/C3  0  (qD_0)/C3  0  0  0   0  0 -1/(R*C3)  w;

0  (qD_0)/C3  0  (qD_0)/C3  0  (qD_0)/C3  0  0  0  0  -w  -1/(R*C3);];
AMF=[A11,A12;A21,A22];

BMF=[1/L1*E1  1/L2*E2 zeros(1,16)]';

XMF=-AMF^-1*BMF;

%M matrix construction

[v0,d]=eig(AMF);ld1=d(1,1);ld2=d(2,2);ld3=d(3,3);ld4=d(4,4);ld5=d(5,5);
ld6=d(6,6);
```

```
v=v0(1:6,1:6);

vec1=v(:,1);vec2=v(:,2);vec3=v(:,3);vec4=v(:,4);vec5=v(:,5);vec6=v(:,6);

I=eye(12);

Hs1=A12*(ld1*I-A22)^-1*A21;Hs2=A12*(ld2*I-A22)^-1*A21;

Hs3=A12*(ld3*I-A22)^-1*A21;

Hs4=A12*(ld4*I-A22)^-1*A21;Hs5=A12*(ld5*I-A22)^-1*A21;

Hs6=A12*(ld6*I-A22)^-1*A21;

H=[Hs1*vec1,Hs2*vec2,Hs3*vec3,Hs4*vec4,Hs5*vec5,Hs6*vec6];

M1=real(H*v^-1);


AM=A11+M1;

B=[1/L1    0      0;
   0    1/L2     0;
   0    0       0;
   0    0       0;
   0    0       0;
   0    0      -1/C3];
U=[E1;E2;0];

X=-AM^-1*B*U;
X1=X(1)
X2=X(2)
X3=X(3)
X4=X(4)
X5=X(5)
X6=X(6)

%Scale Matrices
D_d=diag([0.1,0.1]);
D_w=diag([5.6,2.6,1]);
D_e=diag([1/0.5,1/0.2]); % allowed error: 0.5V and 0.2A


Ad=AM;
Bd=[(A1-A3)*X+(B1-B3)*U (A2-A3)*X+(B2-B3)*U]*D_d;%B matrix for control
input
%dx/dt=A*x+Bw*w+Bd*d; w=[e1;e2;iout];d=[d1;d2];
Cd=D_e*[0 0 0 0 0 1;0 1 0 0 0 0];%C matrix has been scaled
Fd=[0 0;0 0];

Aw=AM;
Bw=B*D_w;% B matrix for disturbance
Cw=D_e*[0 0 0 0 0 1;0 1 0 0 0 0];
```

```
Fw=[0 0 0;0 0 0];

% control-to-output transfer function
misepic=ss(Ad,Bd,Cd,Fd);
Gd=tf(misepic);
Gd_s=sysbal(pck(Ad,Bd,Cd,Fd));

% disturbance to output transfer function
disturbance=ss(Aw,Bw,Cw,Fw);
Gw=tf(disturbance);
Gw_s=sysbal(pck(Aw,Bw,Cw,Fw));

%y=G*d+Gw*w;
Awd=AM;
Bwd=[Bw,Bd];
Cwd=Cw;
Fwd=zeros(2,5);

wd=ss(Awd,Bwd,Cwd,Fwd);
Gwd=tf(wd);
Gwd_s=sysbal(pck(Awd,Bwd,Cwd,Fwd));
```

APPENDIX B. SYNTHESIS OF THE DECENTRALIZED CONTROLLER

Appendix C includes the MATLAB code to perform the controller synthesis for the MI-SEPIC controlled by a decentralized controller (as described in Chapter 4). The code is based on the multi-frequency modeling presented in Appendix A.

MATLAB Code

```
%Scale/Weight Matrices
D_d=daug(5,5);
Ww0=daug(1,1,0.6);
D_e_inv=daug(1/1,1/1); % allowed error: 1V and 1A
Wr=daug(1/21,0.4);

int=tf([1],[1 0])*eye(6);

Kp_v=1;
Ki_v=300;
Kp_i=5;
Ki_i=600;
k_v  = nd2sys([1 Ki_v],[1 0.00001],Kp_v);
k_i  = nd2sys([1 Ki_i],[1 0.00001],Kp_i);
[a,b,c,d]=unpck(daug(k_v,k_i));
K=tf(ss(a,b,c,d));

A_del=diag([1/L1,1/L2,1/L3,1/C1,1/C2,1/C3])*[1 1 0 0;1 1 0 0;1 1 0 0;0
0 1 0;0 0 0 1;0 0 1 1];
Bw=B;
Bd=Bd_M*D_d;
del_coefficient=diag([0.1,0.1,0.1,0.1]);
C_del=del_coefficient*[0 0 0 1 0 1;0 0 0 0 1 1; -1 -1 -1 0 0 0;-1 -1 -1
0 0 0];
CC=[0 0 0 0 0 1;0 1 0 0 0 0];
H=[1/21,0;0 0.4];
We=eye(2);

systemnames = 'Bd Bw Ww0 A_del AM int CC C_del H We Wr';
inputvar='[u{4}time-varying;w{3};r{2};d{2}]';
outputvar='[C_del;CC;We]';
input_to_A_del='[u]';
input_to_Bd='[d]';
input_to_Ww0='[w]';
input_to_Bw='[Ww0]';
input_to_int='[A_del+Bw+Bd+AM]';
input_to_AM='[int]';
input_to_C_del='[int]';
input_to_CC='[int]';
input_to_H='[CC]';
input_to_Wr='[r]';
```

```
input_to_We='[Wr-H]';
sysoutname='P_s';
clearnupsysic='yes';
sysic;
Ns=minreal(lft(P_s,K));
% [a,b,c,d]=ssdata(Ns);
% N=ltisys(a,b,c,d);

omega=logspace(-2,5,100);
Nf=frd(Ns,omega);

% mu
% blk = [1 1;1 1;1 1;1 1];
% [mubnds,muinfo]=mussv(N,blk);
% size(N)
Nnp = Nf(5:6,5:9);
[mubnds,mu_NP_info] = mussv(Nnp,[5,2],'a');
mu_NP=mubnds(:,1);
[muNPinf,muNPw] = norm(mu_NP,inf)
%% RS
Nrs=Nf(1:4,1:4);
[mubnds,muinfo]=mussv(Nrs,[-1 0;-1 0;-1 0;-1 0],'a');
muRS=mubnds(:,1);[muRSinf,muRSw]=norm(muRS,inf)
bodemag(muRS,'',omega)
%% RP
% [mubnds,muinfo]=mussv(Nf,[-1 0;-1 0;-1 0;-1 0;5 2],'c');
% muRP=mubnds(:,1); muRPinf=fnorm(muRP); [muRPinf,muRPw] =
norm(muRP,inf) % muRPinf=5.7726
% bodemag(muRP,'',muRS,'--',omega)
Nrp = Nf(1:6,1:7);
[mubnds,muinfo]=mussv(Nrp,[-1 0;-1 0;-1 0;-1 0;3 2],'c');
muRP=mubnds(:,1);
% muRPinf=fnorm(muRP);
[muRPinf,muRPw] = norm(muRP,inf) % muRPinf=5.7726
% [mu_RP, dvec, sens, pvec] = mu(Nf,[1 1;1 1;1 1;1 1;1 1;1 1;1 1;1 1;1 1;1
1;1 1;1 1;1 1;1 1;1 1;1 1;9 4]);
bodemag(muRP,'--',omega)
%
bodemag(muRP,'',muRS,'--',mu_NP,'-.',omega)
```

APPENDIX C. MULTIVARIABLE STATE-FEEDBACK CONTROLLER DESIGN

Appendix C includes the MATLAB code to generate the controller K in (5.27). The simulation performed by the MATLAB is also described in Fig. A.2.

MATLAB Code

```
addpath(genpath('D:\Program Files (x86)\MATLAB\mpt'));

clear all
clc

n = 13;

L1=320e-6;L2=320e-6;L3=320e-6;L4=320e-6;
C1=470e-6;C2=470e-6;C3=470e-6;C4=470e-6;CM=470e-6;
R1=0.02;R2=0.02;RM=0.1;
rL1=0.02;rL2=0.02;rL3=0.02;rL4=0.02;r11=0.05; r12=0.05; r21=0.05;
r22=0.05; r31=0.05;r32=0.05;r41=0.05;r42=0.05;
E3=0;E4=0;
EM=26.6;
% a1=rL1+D1*r11+(1-D1)*r12; a2=rL2+D2*r21+(1-D2)*r22; a3=rL3+D3*r31+(1-
D3)*r32;a4=rL4+D4*r41+(1-D4)*r42;
a1=0.07;a2=0.07;a3=0.07;a4=0.07;

Anom0=[-1/(R1*C1)   -1/C1    0       0      0      0      0      0      0;
         1/L1     -a1/L1   0       0      0      0      0      0      0;
         0        0    -1/(R2*C2)  -1/C2   0      0      0      0      0;
         0        0     1/L2      -a2/L2  0      0      0      0      0;
         0        0       0        0     0      -1/C3   0      0      0;
         0        0       0        0    1/L3    -a3/L3  0      0      0;
         0        0       0        0      0       0    0      -1/C4   0;
         0        0       0        0      0       0   1/L4    -a4/L4  0;
         0        0       0        0      0       0     0      0   -
1/(RM*CM)];

Bnom0 =[0      0      0      0;
      EM/L1   0      0      0;
      0       0      0      0;
      0    EM/L2     0      0;
      0       0      0      0;
      0       0     EM/L3   0;
      0       0      0      0;
      0       0      0   EM/L4;
      0       0      0      0;];

C =[0 1 0 0 0 0 0 0 0;
   0 0 0 1 0 0 0 0 0;
   0 0 0 0 1 0 0 0 0;
   0 0 0 0 0 0 1 0 0];
```

```
Anom=[Anom0,zeros(9,4);-C,zeros(4,4)];
Bnom=[Bnom0;zeros(4,4)];

E1_range=[12,18];
E2_range=[12,18];
alpha_range=[0.02;0.1];
beta_range=[0.02;0.1];
D3_range = [0,1];
D4_range = [0,1];
% IL1_range = [0,2];%Èç¹û²»ÐÐ£¬¿¼ÂÇÍÆµ¼duty ºÍ IL, E1µÄ¹ØÏµ
% IL2_range = [0,2];
% p1_range = [0.008,0.06];
% p2_range = [0.008,0.06];

x=0;

Ax=Anom;Bx=Bnom;

for e1=1:2
    for e2=1:2
       for r3=1:2
          for r4=1:2
             for d3=1:2
                for d4=1:2
%                    for i1=1:2
%                       for i2=1:2
                           beta = beta_range(r4);
                           alpha = alpha_range(r3);
                           E2 = E2_range(e2);
                           E1 = E1_range(e1);
                           D4 = D4_range(d4);
                           D3 = D3_range(d3);
                           p1 = alpha*D3;
                           p2 = beta*D4;
%                            p1 = p1_range(j1);
%                            p2 = p2_range(j2);
%                            IL1 = IL1_range(i1);
%                            IL1 = IL1_range(i1);
%                            IL2 = IL2_range(i2);

                           IL1 = 2;
                           IL2 = 2;

                           D1=(EM-E1)/EM;
                           D2=(EM-E2)/EM;
                           x=x+1;
                           Ax(2,9)= -(1-D1)/L1;
                           Ax(4,9)= -(1-D2)/L2;
                           Ax(6,9)= -(1-D3)/L3;
                           Ax(8,9)= -(1-D4)/L4;
                           Ax(9,2)= (1-D1)/CM;
                           Ax(9,4)= (1-D2)/CM;
```

```
                                    Ax(9,6)= (1-D3)/CM;
                                    Ax(9,8)= (1-D4)/CM;
                                    Ax(5,5)= -1/(C3)*alpha;
                                    Ax(7,7)= -1/(C4)*beta;
                                    eval(['Ag',int2str(x),' = [Ax]']);
                                    Bx(9,1)=-IL1/CM;
                                    Bx(9,2)=-IL2/CM;
                                    Bx(9,3)=alpha*D3*EM/CM;
                                    Bx(9,4)=beta*D4*EM/CM;
                                    eval(['Bgd',int2str(x),' = [Bx]']);

%a1=rL1+D1*r11+(1-D1)*r12; a2=rL2+D2*r21+(1-D2)*r22; a3=rL3+D3*r31+(1-
D3)*r32;a4=rL4+D4*r41+(1-D4)*r42;
A = [-1/(R1*C1)   -1/C1     0       0      0      0      0      0      0;

1/L1     -a1/L1    0       0      0      0      0      0     -(1-D1)/L1;

0        0    -1/(R2*C2)  -1/C2   0      0      0      0          0;

0        0     1/L2     -a2/L2   0      0      0      0     -(1-D2)/L2;

0        0       0        0  -1/(C3)*alpha  -1/C3   0      0         0;

0        0       0        0    1/L3    -a3/L3  0      0     -(1-D3)/L3;
0        0       0        0      0      0  -1/(C4)*beta -1/C4      0;
0        0       0        0      0      0    1/L4   -a4/L4   -(1-D4)/L4;
0   (1-D1)/CM  0    (1-D2)/CM   0   (1-D3)/CM  0  (1-D4)/CM  -1/(RM*CM);];
B =[1/(R1*C1)    0      0      0         0;
    0           0      0      0         0;
    0        1/(R2*C2)  0      0         0;
    0           0      0      0         0;
    0           0    1/(C3)*alpha 0         0;
    0           0      0      0         0;
    0           0      0      1/(C4)*beta  0;
    0           0      0      0         0;
    0           0      0      0         1/(RM*CM); ];
Bgw = [B;zeros(4,5)];%B:6by4;Bgw:10by4
Cg = [C,zeros(4,4)];%Cg:4by10
Ezw = zeros(4,4);
Ezu = zeros(4,4);
U = [E1,E2,E3,E4,EM]';
X = -A^-1*B*U;
%                   Bdx = [A1*X,A2*X,A3*X,A4*X;];
%                         end
%                     end
                  end
               end
            end
         end
      end
end

W = sdpvar(13,13);
```

```
Y = sdpvar(4,13,'full');
sdpvar t;

F = W>0;
for i=1:64
   eval(['G',int2str(i),' = [Ag', int2str(i) '*W+W*transpose(Ag',
int2str(i) ')+Bgd', int2str(i),'*Y+transpose(Y)*transpose(Bgd',
int2str(i) ') Bgw
W*transpose(Cg)+transpose(Y)*transpose(Ezu);transpose(Bgw) -t*eye(5)
zeros(5,4);Cg*W+Ezu*Y zeros(4,5) -t*eye(4)]']);
end

F =
[F,G1<0,G2<0,G3<0,G4<0,G5<0,G6<0,G7<0,G8<0,G9<0,G10<0,G11<0,G12<0,G13<0
,G14<0,G15<0,G16<0,G17<0,G18<0,G19<0,G20<0,G21<0,G22<0,...

G23<0,G24<0,G25<0,G26<0,G27<0,G28<0,G29<0,G30<0,G31<0,G32<0,G33<0,G34<0
,G35<0,G36<0,G37<0,G38<0,G39<0,G40<0,G41<0,G42<0,G43<0,G44<0,G45<0,G46<
0,G47<0,...

G48<0,G49<0,G50<0,G51<0,G52<0,G53<0,G54<0,G55<0,G56<0,G57<0,G58<0,G59<0
,G60<0,G61<0,G62<0,G63<0,G64<0];

alpha=1000; rou=2*pi/(40*1e-5);theta=25*pi/180;

for i=1:64
   eval(['GB',int2str(i),' = [Ag', int2str(i) '*W+W*transpose(Ag',
int2str(i) ')+Bgd', int2str(i),'*Y+transpose(Y)*transpose(Bgd',
int2str(i) ')+2*alpha*W]']);
end
F =
[F,GB1<0,GB2<0,GB3<0,GB4<0,GB5<0,GB6<0,GB7<0,GB8<0,GB9<0,GB10<0,GB11<0,
GB12<0,GB13<0,GB14<0,GB15<0,GB16<0,GB17<0,GB18<0,GB19<0,GB20<0,GB21<0,G
B22<0,GB23<0,...

GB24<0,GB25<0,GB26<0,GB27<0,GB28<0,GB29<0,GB30<0,GB31<0,GB32<0,GB33<0,G
B34<0,GB35<0,GB36<0,GB37<0,GB38<0,GB39<0,GB40<0,GB41<0,GB42<0,GB43<0,GB
44<0,GB45<0,...

GB46<0,GB47<0,GB48<0,GB49<0,GB50<0,GB51<0,GB52<0,GB53<0,GB54<0,GB55<0,G
B56<0,GB57<0,GB58<0,GB59<0,GB60<0,GB61<0,GB62<0,GB63<0,GB64<0];

for i=1:64
   eval(['GC',int2str(i),' = [-rou*W W*transpose(Ag', int2str(i)
')+transpose(Y)*transpose(Bgd', int2str(i) ');Ag', int2str(i) '*W+Bgd',
int2str(i),'*Y, -rou*W]'])
end
F =
[F,GC1<0,GC2<0,GC3<0,GC4<0,GC5<0,GC6<0,GC7<0,GC8<0,GC9<0,GC10<0,GC11<0,
GC12<0,GC13<0,GC14<0,GC15<0,GC16<0,GC17<0,GC18<0,GC19<0,GC20<0,GC21<0,G
C22<0,...

GC23<0,GC24<0,GC25<0,GC26<0,GC27<0,GC28<0,GC29<0,GC30<0,GC31<0,GC32<0,G
```

```
C33<0,GC34<0,GC35<0,GC36<0,GC37<0,GC38<0,GC39<0,GC40<0,GC41<0,GC42<0,GC
43<0,...

GC44<0,GC45<0,GC46<0,GC47<0,GC48<0,GC49<0,GC50<0,GC51<0,GC52<0,GC53<0,G
C54<0,GC55<0,GC56<0,GC57<0,GC58<0,GC59<0,GC60<0,GC61<0,GC62<0,GC63<0,GC
64<0];

for i=1:64
       eval(['GD',int2str(i),' = [cos(theta)*(Ag', int2str(i) '*W+
W*transpose(Ag', int2str(i) ') + Bgd',
int2str(i),'*Y+transpose(Y)*transpose(Bgd', int2str(i) ')),
sin(theta)*(Ag', int2str(i) '*W - W*transpose(Ag', int2str(i) ') + Bgd',
int2str(i),'*Y - transpose(Y)*transpose(Bgd', int2str(i)
'));sin(theta)*(-Ag', int2str(i) '*W + W*transpose(Ag', int2str(i) ') -
Bgd', int2str(i),'*Y+transpose(Y)*transpose(Bgd', int2str(i)
')),cos(theta)*(Ag', int2str(i) '*W+ W*transpose(Ag', int2str(i) ') +
Bgd', int2str(i),'*Y+transpose(Y)*transpose(Bgd', int2str(i) '))]'])
end
   F =
[F,GD1<0,GD2<0,GD3<0,GD4<0,GD5<0,GD6<0,GD7<0,GD8<0,GD9<0,GD10<0,GD11<0,
GD12<0,GD13<0,GD14<0,GD15<0,GD16<0,GD17<0,GD18<0,GD19<0,GD20<0,GD21<0,G
D22<0,...

GD23<0,GD24<0,GD25<0,GD26<0,GD27<0,GD28<0,GD29<0,GD30<0,GD31<0,GD32<0,G
D33<0,GD34<0,GD35<0,GD36<0,GD37<0,GD38<0,GD39<0,GD40<0,GD41<0,GD42<0,GD
43<0,GD44<0,...

GD45<0,GD46<0,GD47<0,GD48<0,GD49<0,GD50<0,GD51<0,GD52<0,GD53<0,GD54<0,G
D55<0,GD56<0,GD57<0,GD58<0,GD59<0,GD60<0,GD61<0,GD62<0,GD63<0,GD64<0];

solvesdp(F,t)
% State-feedback Controller
K=double(Y)*inv(double(W));
%for correctness check
%t;
%Wd=double(W);
%eig(Wd)
```

APPENDIX D. SYNTHESIS OF THE STATE-FEEDBACK CONTROLLER

MATLAB Code

```
clear all
clc
%Scale/Weight Matrices
L1=320e-6;L2=320e-6;L3=320e-6;L4=320e-6;
C1=470e-6;C2=470e-6;C3=470e-6;C4=470e-6;CM=470e-6;
R1=0.15;R2=0.15;RM=0.1;

EM=26.6;
del_coefficient=diag([3,3,3,3,0.5,0.5,0.5,0.5,0.5,0.5,1,1,0.02,0.02]);
C_del=[0   1/EM   0   0   0   0   0   0   0;
0   0   0   0   0   0   0   0   1/-EM;
0   0   0   1/EM   0   0   0   0   0;
0   0   0   0   0   0   0   0   1/-EM;
0   0   0   0   -1  0   0   0   0;
0   0   0   0   0   0   -1  0   0;
0   0   0   0   0   1   0   0   0;
0   0   0   0   0   0   0   0   1;
0   0   0   0   0   0   0   1   0;
0   0   0   0   0   0   0   0   1;
0   0   0   0   0   0   0   0   0;
0   0   0   0   0   0   0   0   0;
0   0   0   0   0   0   0   0   0;
0   0   0   0   0   0   0   0   0;];
C_del_scaled=del_coefficient*C_del;

A_del=[0   0   0   0   0   0   0   0   0   0   0   0   0   0   0;
0   1   0   0   0   0   0   0   0   0   0   0   0   0   0;
0   0   0   0   0   0   0   0   0   0   0   0   0   0   0;
0   0   0   1   0   0   0   0   0   0   0   0   0   0   0;
0   0   0   0   1   0   0   0   0   0   0   0   0   0   0;
0   0   0   0   0   0   0   1   0   0   0   0   0   0   0;
0   0   0   0   0   1   0   0   0   0   0   0   0   0   0;
0   0   0   0   0   0   0   0   0   1   0   0   0   0   0;
1   0   1   0   0   0   1   0   1   0   1   1   1   1   1;];

A_del_scaled=diag([1/L1,1/C1,1/L2,1/C2,1/L3,1/C3,1/L4,1/C4,1/CM])*A_del;

P1=0.034;P2=0.034;IL1=0;IL2=0;
Bd =[   0      0      0      0;
      EM/L1    0      0      0;
      0       0      0      0;
      0     EM/L2     0      0;
      0       0      0      0;
      0       0     EM/L3    0;
      0       0      0      0;
      0       0      0   EM/L4;
      -IL1/CM     -IL2/CM     P1*EM/CM    P2*EM/CM ;];
```

```
G3=0.05;G4=0.05;
Bw =[1/(R1*C1)    0      0      0        0;
     0          0      0      0        0;
     0        1/(R2*C2)  0      0        0;
     0          0      0      0        0;
     0          0   1/(C3)*G3 0          0;
     0          0      0      0        0;
     0          0      0   1/(C4)*G4    0;
     0          0      0      0        0;
     0          0      0      0        1/(RM*CM); ];
% Bw =[1/(R1*C1)    0      0      0        0;
%      0          0      0      0        0;
%      0        1/(R2*C2)  0      0        0;
%      0          0      0      0        0;
%      0          0   1/(C3)*VC3 0          0;
%      0          0      0      0        0;
%      0          0      0   1/(C4)*VC4    0;
%      0          0      0      0        0;
%      0          0      0      0        1/(RM*CM); ];
% w=[E1, E2, G3, G4, EM]
int_9=tf(1,[1 0])*eye(9);D3=0.5;D4=0.5;

a1=0.07;a2=0.07;a3=0.07;a4=0.07;E1=40;E2=40;
A = [-1/(R1*C1)   -1/C1     0       0      0      0      0      0
0;
      1/L1     -a1/L1    0       0      0      0      0      0     -
E1/EM/L1;
        0        0    -1/(R2*C2)  -1/C2   0      0      0      0
0;
        0        0     1/L2     -a2/L2   0      0      0      0     -
E2/EM/L2;
        0        0       0        0  -1/C3*G3  -1/C3    0      0        0;
        0        0       0        0    1/L3    -a3/L3  0      0     -(1-
D3)/L3;
        0        0       0        0      0      0  -1/C4*G3 -1/C4
0    ;
        0        0       0        0      0      0    1/L4   -a4/L4   -(1-
D4)/L4;
        0      E1/EM/CM  0      E2/EM/CM   0   (1-D3)/CM  0  (1-D4)/CM  -
1/(RM*CM);];
% A = [-1/(R1*C1)   -1/C1     0       0      0      0      0      0
0;
%       1/L1     -a1/L1    0       0      0      0      0      0     -
E1/EM/L1;
%         0        0    -1/(R2*C2)  -1/C2   0      0      0      0
0;
%         0        0     1/L2     -a2/L2   0      0      0      0     -
E2/EM/L2;
%         0        0       0        0     0    -1/C3    0      0
0;
%         0        0       0        0    1/L3    -a3/L3  0      0     -
(1-D3)/L3;
```

```
%         0       0       0       0      0      0     0     -1/C4
0    ;
%         0       0       0       0      0      0    1/L4   -a4/L4   -
(1-D4)/L4;
%         0      E1/EM/CM  0      E2/EM/CM   0   (1-D3)/CM  0  (1-D4)/CM
-1/(RM*CM);];
C =[0 1 0 0 0 0 0 0;
    0 0 0 1 0 0 0 0;
    0 0 0 0 1 0 0 0;
    0 0 0 0 0 0 1 0];

int_4=tf(1,[1 0])*eye(4);

E=[0    0   0   0   0   0   0   0   0;
0   0   0   0   0   0   0   0   0;
0   0   0   0   0   0   0   0   0;
0   0   0   0   0   0   0   0   0;
0   0   1   0   0   0   0   0   0;
0   0   0   1   0   0   0   0   0;
0   0   0   0   0   0   0   0   0;
0   0   0   0   0   0   0   0   0;
0   0   0   0   0   0   0   0   0;
0   0   0   0   0   0   0   0   0;
0   0   0   0   0   -1  0   0   0;
0   0   0   0   0   0   -1  0   0;
0   0   0   0   0   0   0   1   0;
0   0   0   0   0   0   0   0   1;];

Ew_del=E(1:14,1:5);
Ed_del=E(1:14,6:9);

Dw=daug(4,6,0,0,0);
Dd=eye(4);
D_e_inv=daug(1/1,1/1,1/1,1/1); % allowed error: 1V and 1A
C_scaled=D_e_inv*C;
% State-feedback Controller K
K = [-3.6752e-002 -1.4563e-001 -5.0744e-005  5.4006e-005  2.5036e-003
1.8827e-004  2.3016e-003  1.8837e-004  2.0775e-002  2.1156e+002 -1.4097e-
001 -2.2587e+000  -2.3942e+000;
-5.6527e-005  2.9802e-005 -3.6753e-002 -1.4568e-001  2.4345e-003
1.9101e-004  2.3327e-003  1.7813e-004  2.0775e-002 -1.3680e-001
2.1157e+002 -2.1159e+000  -2.4434e+000;
6.5146e-004  7.6093e-003  7.0847e-004  7.1729e-003  9.8531e-001 -1.8217e-
001  1.8935e-002 -1.1952e-003  1.3831e-002  2.7507e-001  9.9931e-001 -
1.2999e+003  -5.3337e+001;
5.8941e-004  6.6923e-003  5.4778e-004  7.2734e-003  2.1069e-002 -7.8424e-
004  9.8276e-001 -1.7749e-001  1.3871e-002  3.7467e-001 -2.3516e-001 -
4.6057e+001  -1.2733e+003;];


K_I=eye(13); C_I=eye(14); Wr=eye(4);
```

```
systemnames = 'Wr Bd Bw Dd Dw A_del_scaled A int_9 int_4 C_scaled
C_del_scaled Ew_del Ed_del K_I C_I';

inputvar='[u{14};w{5};r{4};d{4}]';
outputvar='[C_I;C_scaled;K_I]';
input_to_Wr='[r]';
input_to_Bd='[74]';
input_to_Bw='[Dw]';
input_to_Dd='[d]';
input_to_Dw='[w]';
input_to_A_del_scaled='[u]';
input_to_A='[int_9]';
input_to_int_9='[A_del_scaled+Bw+Bd+A]';
input_to_int_4='[Wr-C_scaled]';
input_to_C_scaled='[int_9]';
input_to_C_del_scaled='[int_9]';
input_to_Ew_del='[Dw]';
input_to_Ed_del='[74]';
input_to_K_I='[int_9;int_4]';
input_to_C_I='[C_del_scaled+Ew_del+Ed_del]';

sysoutname='P_s';
clearnupsysic='yes';
sysic;

[MSYS,U]=minreal(lft(P_s,K));
Ns=MSYS;

% [a,b,c,d]=ssdata(Ns);
% N=ltisys(a,b,c,d);
% [a,b,c,d]=unpck(Ns);
% Ns_tf=tf(ss(a,b,c,d));
% N22 = P_s(15:18,15:23);
% N22_min = minreal(N22);
% [a,b,c,d]=ssdata(N22_min);
% N22_tf=tf(a,b,c,d);

omega=logspace(-3,6,1000);
Nf=frd(Ns,omega);

% Nnp = Nf(15:18,15:23);
% [mubnds,mu_NP_info] = mussv(Nnp,[9,4],'a');
% mu_NP=mubnds(:,1);
% [muNPinf,muNPw] = norm(mu_NP,inf)

Nnp = Nf(15:18,15:19);
[mubnds,mu_NP_info] = mussv(Nnp,[5,4],'a');
mu_NP=mubnds(:,1);
[muNPinf,muNPw] = norm(mu_NP,inf)

% [sv,w]=sigma(N22,omega);
% max(max(sv))
% N22 = P_s(15:18,15:23);
```

```
% [sv,w]=sigma(N22,omega);
% max(max(sv))
% vplot(vnorm(N22))
% mu
% blk = [1 1;1 1;1 1;1 1];
% [mubnds,muinfo]=mussv(N,blk);
% size(N)

%% RS
Nrs=Nf(1:14,1:14);
[mubnds,muinfo]=mussv(Nrs,[-1 0;-1 0;-1 0;-1 0;-1 0;-1 0;-1 0;-1 0;-1
0;-1 0;-1 0;-1 0;-1 0;-1 0;],'a');
% [mubnds,muinfo]=mussv(Nrs,[1 1;1 1;1 1;1 1;1 1;1 1;1 1;1 1;1 1;1 1;1
1;1 1;1 1;1 1;],'a');
muRS=mubnds(:,1);[muRSinf,muRSw]=norm(muRS,inf)

%% RP
% [mubnds,muinfo]=mussv(Nf,[-1 0;-1 0;-1 0;-1 0;5 2],'c');
% [mubnds,muinfo]=mussv(Nf,[-1 0;-1 0;-1 0;-1 0;-1 0;-1 0;-1 0;-1 0;-1
0;-1 0;-1 0;-1 0;-1 0;-1 0;9 4],'c');
Nrp = Nf(1:18,1:19);
[mubnds,muinfo]=mussv(Nrp,[-1 0;-1 0;-1 0;-1 0;-1 0;-1 0;-1 0;-1 0;-1
0;-1 0;-1 0;-1 0;-1 0;-1 0;5 4],'c');
muRP=mubnds(:,1);
% muRPinf=fnorm(muRP);
[muRPinf,muRPw] = norm(muRP,inf) % muRPinf=5.7726
% [mu_RP, dvec, sens, pvec] = mu(Nf,[1 1;1 1;1 1;1 1;1 1;1 1;1 1;1 1;1 1;1
1;1 1;1 1;1 1;1 1;1 1;9 4]);
% bodemag(muRP,'--',omega)

bodemag(muRP,'',muRS,'--',mu_NP,'-.',omega)
```

References

[1] G. M. Masters, *Renewable and efficient electric power systems*: Wiley-IEEE Press, 2004.

[2] S. D. Sudhoff, "Currents of Change," *Power and Energy Magazine, IEEE,* vol. 9, pp. 30-37, 2011.

[3] P. Gross and K. L. Godrich, "Total DC Integrated Data Centers," in *Telecommunications Conference, 2005 INTELEC '05 Twenty-Seventh International*, 2005, pp. 125-130.

[4] J. Baek, S. Gab-Su, C. Kyusik, P. Cheol-Woo, K. Hyejin, B. Hyunsu, and H. Bo, "DC Distribution system design and implementation for Green Building," *Green Building Power Forum2011,* 2011.

[5] A. Kwasinski, "Advanced power electronics enabled distribution architectures: Design, operation, and control," in *Power Electronics and ECCE Asia (ICPE & ECCE), 2011 IEEE 8th International Conference on*, 2011, pp. 1484-1491.

[6] S. P. Chowdhury, P. Crossley, and S. Chowdhury, *Microgrids and active distribution networks*: Institution of Engineering and Technology, 2009.

[7] S. Kulkarni, "Overcurrent Protection and Management in AC and DC Power Systems," Qualifying Exam Presentation, The University of Texas at Austin, Austin.

[8] R. W. Erickson and D. Maksimović, *Fundamentals of power electronics*: Springer, 2001.

[9] M. Meinhardt and G. Cramer, "Past, present and future of grid connected photovoltaic- and hybrid-power-systems," in *Power Engineering Society Summer Meeting, 2000 IEEE*, 2000, pp. 1283-1288 vol. 2.

[10] F. Yu and M. Xudong, "A Novel PV Microinverter With Coupled Inductors and Double-Boost Topology," *IEEE Transactions on Power Electronics,* vol. 25, pp. 3139-3147, 2010.

[11] M. Calais, J. Myrzik, T. Spooner, and V. G. Agelidis, "Inverters for single-phase grid connected photovoltaic systems-an overview," in *Power Electronics Specialists Conference, 2002 pesc 02 2002 IEEE 33rd Annual*, 2002, pp. 1995-2000.

[12] S. V. Dhople, J. L. Ehlmann, A. Davoudi, and P. L. Chapman, "Multiple-input boost converter to minimize power losses due to partial shading in photovoltaic modules," in *Energy Conversion Congress and Exposition (ECCE), 2010 IEEE*, 2010, pp. 2633-2636.

[13] A. Kwasinski, *A microgrid architecture with multiple-input DC/DC converters: Applications, reliability, system operation, and control*: ProQuest, 2007.

[14] F. D. Rodriguez and W. G. Imes, "Analysis and modeling of a two-input DC/DC converter with two controlled variables and four switched networks," in *Energy Conversion Engineering Conference, 1996 IECEC 96 Proceedings of the 31st Intersociety*, 1996, pp. 322-327 vol.1.

[15] M. Vilsan and I. Nita, "A hybrid wind-photovoltaic power supply for a telecommunication system," in *Telecommunications Energy Conference, 1997 INTELEC 97, 19th International*, 1997, pp. 589-591.

[16] J. Sebastian, P. J. Villegas, F. Nuno, and M. M. Hernando, "High-efficiency and wide-bandwidth performance obtainable from a two-input buck converter," *IEEE Transactions on Power Electronics,* vol. 13, pp. 706-717, 1998.

[17] F. Giraud and Z. M. Salameh, "Steady-state performance of a grid-connected rooftop hybrid wind-photovoltaic power system with battery storage," *IEEE Transactions on Energy Conversion,* vol. 16, pp. 1-7, 2001.

[18] A. Di Napoli, F. Crescimbini, L. Solero, F. Caricchi, and F. G. Capponi, "Multiple-input DC-DC power converter for power-flow management in hybrid vehicles," in *Industry Applications Conference, 2002 37th IAS Annual Meeting Conference Record of the*, 2002, pp. 1578-1585 vol.3.

[19] Y.-M. Chen, Y.-C. Liu, and F.-Y. Wu, "Multi-input DC/DC converter based on the multiwinding transformer for renewable energy applications," *IEEE Transactions on Industry Applications,* vol. 38, pp. 1096-1104, 2002.

[20] B. G. Dobbs and P. L. Chapman, "A multiple-input DC-DC converter topology," *IEEE Power Electronics Letters,* vol. 1, pp. 6-9, 2003.

[21] Y.-M. Chen, Y.-C. Liu, and S.-H. Lin, "Double-input PWM DC/DC converter for high/low voltage sources," in *Telecommunications Energy Conference, 2003 INTELEC '03 The 25th International*, 2003, pp. 27-32.

[22] H. Matsuo, W. Lin, F. Kurokawa, T. Shigemizu, and N. Watanabe, "Characteristics of the multiple-input DC-DC converter," *IEEE Transactions on Industrial Electronics,* vol. 51, pp. 625-631, 2004.

[23] L. Solero, A. Lidozzi, and J. A. Pomilio, "Design of multiple-input power converter for hybrid vehicles," *IEEE Transactions on Power Electronics,* vol. 20, pp. 1007-1016, 2005.

[24] N. D. Benavides and P. L. Chapman, "Power budgeting of a multiple-input buck-boost converter," *IEEE Transactions on Power Electronics,* vol. 20, pp. 1303-1309, 2005.

[25] H.-J. Chiu, H.-M. Huang, L.-W. Lin, and M.-H. Tseng, "A multiple-input DC/DC converter for renewable energy systems," in *Industrial Technology, 2005 ICIT 2005 IEEE International Conference on*, 2005, pp. 1304-1308.

[26] H. Tao, A. Kotsopoulos, J. L. Duarte, and M. A. M. Hendrix, "Multi-input bidirectional DC-DC converter combining DC-link and magnetic-coupling for fuel cell systems," in *Industry Applications Conference, 2005 Fourtieth IAS Annual Meeting Conference Record of the 2005*, 2005, pp. 2021-2028 Vol. 3.

[27] K. Kobayashi, H. Matsuo, and Y. Sekine, "Novel Solar-Cell Power Supply System Using a Multiple-Input DC-DC Converter," *IEEE Transactions on Industrial Electronics,* vol. 53, pp. 281-286, 2006.

[28] A.-A. Hussam, P. Michael, and B. Issa, "A Zero-Voltage Switching Three-Port Isolated Full-Bridge Converter," in *Telecommunications Energy Conference, 2006 INTELEC '06 28th Annual International*, 2006, pp. 1-8.

[29] H. Tao, A. Kotsopoulos, J. L. Duarte, and M. A. M. Hendrix, "Family of multiport bidirectional DC-DC converters," *Electric Power Applications, IEE Proceedings - ,* vol. 153, pp. 451-458, 2006.

[30] Y.-M. Chen, Y.-C. Liu, and S.-H. Lin, "Double-Input PWM DC/DC Converter for High-/Low-Voltage Sources," *Industrial Electronics, IEEE Transactions on,* vol. 53, pp. 1538-1545, 2006.

[31] M. Marchesoni and C. Vacca, "New DC-DC Converter for Energy Storage System Interfacing in Fuel Cell Hybrid Electric Vehicles," *IEEE Transactions on Power Electronics,* vol. 22, pp. 301-308, 2007.

[32] A. Kwasinski and P. T. Krein, "Multiple-input dc-dc converters to enhance local availability in grids using distributed generation resources," in *Applied Power Electronics Conference, APEC 2007 - Twenty Second Annual IEEE*, 2007, pp. 1657-1663.

[33] H. Al-Atrash and I. Batarseh, "Boost-Integrated Phase-Shift Full-Bridge Converter for Three-Port Interface," in *Power Electronics Specialists Conference, 2007 PESC 2007 IEEE*, 2007, pp. 2313-2321.

[34] A. Kwasinski, "Identification of Feasible Topologies for Multiple-Input DC-DC Converters," *IEEE Transactions on Power Electronics,* vol. 24, pp. 856-861, 2009.

[35] R. Zhao and A. Kwasinski, "Multiple-input single ended primary inductor converter (SEPIC) converter for distributed generation applications," in *Energy Conversion Congress and Exposition, 2009 ECCE 2009 IEEE*, 2009, pp. 1847-1854.

[36] Y.-C. Liu and Y.-M. Chen, "A Systematic Approach to Synthesizing Multi-Input DC-DC Converters," *IEEE Transactions on Power Electronics,* vol. 24, pp. 116-127, 2009.

[37] A. Khaligh, J. Cao, and Y.-J. Lee, "A Multiple-Input DC-DC Converter Topology," *IEEE Transactions on Power Electronics,* vol. 24, pp. 862-868, 2009.

[38] Y. Li, X. Ruan, D. Yang, and F. Liu, "Modeling, analysis and design for hybrid power systems with dual-input DC/DC converter," in *Energy Conversion Congress and Exposition, 2009 ECCE 2009 IEEE*, 2009, pp. 3203-3210.

[39] Z. Li, O. Onar, A. Khaligh, and E. Schaltz, "Design and Control of a Multiple Input DC/DC Converter for Battery/Ultra-capacitor Based Electric Vehicle Power System," in *Applied Power Electronics Conference and Exposition, 2009 APEC 2009 Twenty-Fourth Annual IEEE*, 2009, pp. 591-596.

[40] D. Yang, X. Ruan, Y. Li, and F. Liu, "Multiple-input full bridge dc/dc converter," in *Energy Conversion Congress and Exposition, 2009 ECCE 2009 IEEE*, 2009, pp. 2881-2888.

[41] Y. Li, X. Ruan, D. Yang, F. Liu, and C. K. Tse, "Synthesis of Multiple-Input DC/DC Converters," *IEEE Transactions on Power Electronics,* vol. 25, pp. 2372-2385, 2010.

[42] Z. Qian, O. Abdel-Rahman, and I. Batarseh, "An Integrated Four-Port DC/DC Converter for Renewable Energy Applications," *IEEE Transactions on Power Electronics,* vol. 25, pp. 1877-1887, 2010.

[43] S. H. Choung and A. Kwasinski, "Multiple-input modified inverse Watkins-Johnson converter without coupled inductors," in *Energy Conversion Congress and Exposition (ECCE), 2010 IEEE*, 2010, pp. 3253-3260.

[44] R.-J. Wai, C.-Y. Lin, J.-J. Liaw, and Y.-R. Chang, "Newly Designed ZVS Multi-Input Converter," *IEEE Transactions on Industrial Electronics,* vol. 58, pp. 555-566, 2011.

[45] A. Kwasinski, "Quantitative Evaluation of DC Microgrids Availability: Effects of System Architecture and Converter Topology Design Choices," *IEEE Transactions on Power Electronics,* vol. 26, pp. 835-851, 2011.

[46] S.-Y. Yu, J. Song, and A. Kwasinski, "A multiple-input current-source converter for a stand-alone hybrid power system," in *Applied Power Electronics Conference and Exposition (APEC), 2011 Twenty-Sixth Annual IEEE*, 2011, pp. 35-40.

[47] Q. Wang, J. Zhang, X. Ruan, and K. Jin, "Isolated Single Primary Winding Multiple-Input Converters," *IEEE Transactions on Power Electronics,* vol. 26, pp. 3435-3442, 2011.

[48] W. Li, J. Xiao, Y. Zhao, and X. He, "PWM Plus Phase Angle Shift (PPAS) Control Scheme for Combined Multiport DC/DC Converters," *IEEE Transactions on Power Electronics,* vol. 27, pp. 1479-1489, 2012.

[49] L. Palma and P. N. Enjeti, "A modular fuel cell, modular DC–DC converter concept for high performance and enhanced reliability," *IEEE Transactions on Power Electronics,* vol. 24, pp. 1437-1443, 2009.

[50] R. Zhao, "A multiple-input single ended primary inductor converter for modular micro-grids with hybrid low-power sources," Master's Thesis, Department of Electrical and Computer Engineering, The University of Texas at Austin, Austin, 2010.

[51] N. D. Benavides, T. Esram, and P. L. Chapman, "Ripple Correlation Control of a Multiple-Input Dc-Dc Converter," in *Power Electronics Specialists Conference, 2005 PESC '05 IEEE 36th*, 2005, pp. 160-164.

[52] S. Y. Yu and A. Kwasinski, "Analysis of a soft-switching technique for isolated time-sharing multiple-input converters," in *Applied Power Electronics Conference and Exposition (APEC), 2012 Twenty-Seventh Annual IEEE*, 2012, pp. 844-851.

[53] S. Bae and A. Kwasinski, "Maximum power point tracker for a multiple-input Cuk dc-dc converter," in *Telecommunications Energy Conference, 2009 INTELEC 2009 31st International*, 2009, pp. 1-5.

[54] V. Mummadi and K. K. Sawant, "Control of Multi-Input Integrated Buck-Boost Converter," in *Industrial and Information Systems, 2008 ICIIS 2008 IEEE Region 10 and the Third international Conference on*, 2008, pp. 1-6.

[55] J. M. Maciejowski, *Multivariable feedback design*, 1989.

[56] S. Skogestad and I. Postlethwaite, *Multivariable feedback control analysis and design*, 2005.

[57] G. C. Goodwin, S. F. Graebe, and M. E. Salgado, *Control system design* vol. 240: Prentice Hall New Jersey, 2001.

[58] J. Wei and B. Fahimi, "Multiport Power Electronic Interface—Concept, Modeling, and Design," *IEEE Transactions on Power Electronics,* vol. 26, pp. 1890-1900, 2011.

[59] W. Xiao, W. G. Dunford, P. R. Palmer, and A. Capel, "Regulation of Photovoltaic Voltage," *Industrial Electronics, IEEE Transactions on,* vol. 54, pp. 1365-1374, 2007.

[60] A. Dumais, "Grid-Connected Solar Microinverter Reference Design Using a dsPIC® Digital Signal Controller," 2010.

[61] M. G. Villalva and J. R. Gazoli, "Comprehensive approach to modeling and simulation of photovoltaic arrays," *IEEE Transactions on Power Electronics,* vol. 24, pp. 1198-1208, 2009.

[62] T. Esram, J. W. Kimball, P. T. Krein, P. L. Chapman, and P. Midya, "Dynamic maximum power point tracking of photovoltaic arrays using ripple correlation control," *IEEE Transactions on Power Electronics,* vol. 21, pp. 1282-1291, 2006.

[63] S. Chun and A. Kwasinski, "Analysis of Classical Root-Finding Methods Applied to Digital Maximum Power Point Tracking for Sustainable Photovoltaic Energy Generation," *IEEE Transactions on Power Electronics,* vol. 26, pp. 3730-3743, 2011.

[64] T. Suntio, J. Leppäaho, J. Huusari, and L. Nousiainen, "Issues on Solar-Generator Interfacing With Current-Fed MPP-Tracking Converters," *IEEE Transactions on Power Electronics,* vol. 25, pp. 2409-2419, 2010.

[65] M. H. Rashid, *Power electronics handbook*: Academic Pr, 2001.

[66] S.-Y. Yu and A. Kwasinski, "Analysis of a soft-switching technique for isolated time-sharing multiple-input converters," in *Applied Power Electronics Conference and Exposition (APEC), 2012 Twenty-Seventh Annual IEEE*, 2012, pp. 844-851.

[67] L. Bor-Ren and C. Chun-Chi, "Soft Switching Isolated Sepic Converter with the Buck-Boost Type of Active Clamp," in *Industrial Electronics and Applications, 2007 ICIEA 2007 2nd IEEE Conference on*, 2007, pp. 1232-1237.

[68] S.-Y. Yu, R. Zhao, and A. Kwasinski, "Design considerations of a multiple-input isolated single ended primary inductor converter (SEPIC) for distributed generation sources," in *Energy Conversion Congress and Exposition (ECCE), 2011 IEEE*, 2011, pp. 3960-3967.

[69] D. C. Hamill and P. T. Krein, "A `zero' ripple technique applicable to any DC converter," in *Power Electronics Specialists Conference, 1999 PESC 99 30th Annual IEEE*, 1999, pp. 1165-1171 vol.2.

[70] J. Jung and A. Kwasinski, "A multiple-input SEPIC with a bi-directional input for modular distributed generation and energy storage integration," in *Applied Power Electronics Conference and Exposition (APEC), 2011 Twenty-Sixth Annual IEEE*, 2011, pp. 28-34.

[71] Available: http://files.sma.de/dl/7418/Rueckstrom-UEN083010.pdf

[72] R. MUHAMMAD, *Power electonics handbook*, 2010.

[73] Available: http://www.power-sonic.com/images/powersonic/sla_batteries/ps_psg_series/12volt/PS-1250_11_Feb_21.pdf

[74] R. D. Middlebrook, "Small-signal modeling of pulse-width modulated switched-mode power converters," *Proceedings of the IEEE,* vol. 76, pp. 343-354, 1988.

[75] P. T. Krein, J. Bentsman, R. M. Bass, and B. L. Lesieutre, "On the use of averaging for the analysis of power electronic systems," *IEEE Transactions on Power Electronics,* vol. 5, pp. 182-190, 1990.

[76] J. Sun, D. M. Mitchell, M. F. Greuel, P. T. Krein, and R. M. Bass, "Averaged modeling of PWM converters operating in discontinuous conduction mode," *IEEE Transactions on Power Electronics,* vol. 16, pp. 482-492, 2001.

[77] Y. Fuad, W. L. de Koning, and J. W. van der Woude, "On the stability of the pulsewidth-modulated Cuk converter," *IEEE Transactions on Circuits and Systems II: Express Briefs,* vol. 51, pp. 412-420, 2004.

[78] V. A. Caliskan, O. C. Verghese, and A. M. Stankovic, "Multifrequency averaging of DC/DC converters," *IEEE Transactions on Power Electronics,* vol. 14, pp. 124-133, 1999.

[79] J. Mahdavi, A. Emaadi, M. D. Bellar, and M. Ehsani, "Analysis of power electronic converters using the generalized state-space averaging approach," *IEEE Transactions on Circuits and Systems I: Fundamental Theory and Applications,* vol. 44, pp. 767-770, 1997.

[80] J. W. van der Woude, W. L. de Koning, and Y. Fuad, "On the periodic behavior of PWM DC-DC converters," *IEEE Transactions on Power Electronics,* vol. 17, pp. 585-595, 2002.

[81] Y. Chen, A. Davoudi, and P. L. Chapman, "Multifrequency modeling of a multiple-input Dc-Dc converter," in *Power Electronics Specialists Conference, 2008 PESC 2008 IEEE*, 2008, pp. 4604-4610.

[82] I. J. Perez-Arriaga, G. C. Verghese, and F. C. Schweppe, "Selective Modal Analysis with Applications to Electric Power Systems, Part I: Heuristic Introduction," *Power Engineering Review, IEEE,* vol. PER-2, pp. 29-30, 1982.

[83] H. K. Khalil and J. Grizzle, *Nonlinear systems*: Macmillan Publishing Company New York, 1992.

[84] T. Esram and P. L. Chapman, "Comparison of Photovoltaic Array Maximum Power Point Tracking Techniques," *IEEE Transactions on Energy Conversion,* vol. 22, pp. 439-449, 2007.

[85] A. Lidozzi and L. Solero, "Power balance control of multiple-input DC-DC power converter for hybrid vehicles," in *Industrial Electronics, 2004 IEEE International Symposium on*, 2004, pp. 1467-1472 vol. 2.

[86] R. Zhao, S.-Y. Yu, and A. Kwasinski, "Modeling of multiple-input DC-DC converters considering input-coupling effects," in *Energy Conversion Congress and Exposition (ECCE), 2011 IEEE*, 2011, pp. 698-705.

[87] P. T. Krein, *Elements of power electronics* vol. 101: Oxford University Press New York, 1998.

[88] N. Mohan and T. M. Undeland, *Power electronics: converters, applications, and design*: Wiley-India, 2007.

[89] S. Tavakoli, I. Griffin, and P. J. Fleming, "Tuning of decentralised PI (PID) controllers for TITO processes," *Control engineering practice,* vol. 14, pp. 1069-1080, 2006.

[90] G. C. Goodwin, S. F. Graebe, and M. E. Salgado, "Control system design," 2001.

[91] Q. G. Wang, Z. Ye, and W. J. Cai, *PID control for multivariable processes* vol. 373: Springer Verlag, 2008.

[92] L. Shang and X. Wang, "Decentralized PI control for a congestion game," in *Control, Automation, Robotics and Vision Conference, 2004 ICARCV 2004 8th*, 2004, pp. 316-319 Vol. 1.

[93] S. Tavakoli, I. Griffin, and P. J. Fleming, "Decentralized PI control of a rolls-royce jet engine," in *Control Applications, 2005 CCA 2005 Proceedings of 2005 IEEE Conference on*, 2005, pp. 370-375.

[94] W. L. Luyben, "Simple method for tuning SISO controllers in multivariable systems," *Industrial & Engineering Chemistry Process Design and Development,* vol. 25, pp. 654-660, 1986.

[95] J. O'REILLY and W. Leithead, "Multivariable control by'individual channel design'," *International Journal of Control,* vol. 54, pp. 1-46, 1991.

[96] D. Chen and D. E. Seborg, "Design of decentralized PI control systems based on Nyquist stability analysis," *Journal of Process Control,* vol. 13, pp. 27-39, 2003.

[97] W. Leithead and J. O'REILLY, "Performance issues in the individual channel design of 2-input 2-output systems. I- Structural issues," *International Journal of Control,* vol. 54, pp. 47-82, 1991.

[98] W. Leithead and J. O'REILLY, "m-input m-output feedback control by individual channel design. I: Structural issues," *International Journal of Control,* vol. 56, pp. 1347-1397, 1992.

[99] R. Zhao and A. Kwasinski, "Analysis of decentralized controller for multiple-input converters," in *Applied Power Electronics Conference and Exposition (APEC), 2012 Twenty-Seventh Annual IEEE*, 2012, pp. 1853-1860.

[100] M. Morari and E. Zafiriou, *Robust process control*: Morari, 1989.

[101] M. Driels, *Linear control systems engineering*: McGraw-Hill Higher Education, 1995.

[102] R. Tymerski, "Worst-case stability analysis of switching regulators using the structured singular value," *IEEE Transactions on Power Electronics,* vol. 11, pp. 723-730, 1996.

[103] Z. Tao and B. Francois, "Energy Management and Power Control of a Hybrid Active Wind Generator for Distributed Power Generation and Grid Integration," *IEEE Transactions on Industrial Electronics,* vol. 58, pp. 95-104, 2011.

[104] P. Karlsson and J. Svensson, "DC bus voltage control for a distributed power system," *IEEE Transactions on Power Electronics,* vol. 18, pp. 1405-1412, 2003.

[105] D. Chen and L. Xu, "Autonomous DC Voltage Control of a DC Microgrid With Multiple Slack Terminals," *IEEE Transactions on Power Systems,* vol. PP, pp. 1-9, 2012.

[106] H. Kwakernaak, "Robust control and H ∞ -optimization--Tutorial paper," *Automatica,* vol. 29, pp. 255-273, 1993.

[107] R. Naim, G. Weiss, and S. Ben-Yaakov, "H∞ control applied to boost power converters," *IEEE Transactions on Power Electronics,* vol. 12, pp. 677-683, 1997.

[108] E. Vidal-Idiarte, L. Martinez-Salamero, H. Valderrama-Blavi, F. Guinjoan, and J. Maixe, "Analysis and design of H∞ control of nonminimum phase-switching converters," *IEEE Transactions on Circuits and Systems I: Fundamental Theory and Applications,* vol. 50, pp. 1316-1323, 2003.

[109] W. Hernandez, "H∞ integral control of a buck-boost dc-dc converter," in *Communications, Control and Signal Processing, 2008 ISCCSP 2008 3rd International Symposium on*, 2008, pp. 1425-1430.

[110] S. Boyd, L. El Ghaoui, E. Feron, and V. Balakrishnan, *Linear matrix inequalities in system and control theory* vol. 15: Society for Industrial Mathematics, 1994.

[111] V. F. Montagner and L. D. Peres, "H∞ control with pole location for a DC-DC converter with a switched load," in *Industrial Electronics, 2003 ISIE '03 2003 IEEE International Symposium on*, 2003, pp. 550-555 vol. 1.

[112] C. Olalla, R. Leyva, A. El Aroudi, P. Garces, and I. Queinnec, "LMI robust control design for boost PWM converters," *IET Power Electronics,* vol. 3, pp. 75-85, 2010.

[113] Q. G. Wang, *PID control for multivariable processes* vol. 373: Springer Verlag, 2008.

[114] G. Zames, "Feedback and optimal sensitivity: Model reference transformations, multiplicative seminorms, and approximate inverses," *IEEE Transactions on Automatic Control,* vol. 26, pp. 301-320, 1981.

[115] J. C. Doyle, K. Glover, P. P. Khargonekar, and B. A. Francis, "State-space solutions to standard H2 and H∞ control problems," *IEEE Transactions on Automatic Control,* vol. 34, pp. 831-847, 1989.

[116] D. Walker, I. Postlethwaite, J. Howitt, and N. Foster, "Rotorcraft flying qualities improvement using advanced control," in *NASA Ames Research Center, Piloting Vertical Flight Aircraft: A Conference on Flying Qualities and Human Factors* 1993, pp. 141-155.

[117] L. Xie, M. Fu, and C. E. de Souza, "H∞ control and quadratic stabilization of systems with parameter uncertainty via output feedback," *IEEE Transactions on Automatic Control,* vol. 37, pp. 1253-1256, 1992.

[118] L. Xie and E. de Souza Carlos, "Robust H∞ control for linear systems with norm-bounded time-varying uncertainty," *IEEE Transactions on Automatic Control,* vol. 37, pp. 1188-1191, 1992.

[119] C. E. de Souza, A. Trofino, and J. de Oliveira, "Robust H∞ control of uncertain linear systems via parameter-dependent Lyapunov functions," in *Decision and Control, 2000 Proceedings of the 39th IEEE Conference on*, 2000, pp. 3194-3199 vol.4.

[120] P. Gahinet and P. Apkarian, "A linear matrix inequality approach to H∞ control," *International Journal of Robust and Nonlinear Control,* vol. 4, pp. 421-448, 1994.

[121] P. Gahinet, A. Nemirovskii, A. J. Laub, and M. Chilali, "The LMI control toolbox," in *Decision and Control, 1994, Proceedings of the 33rd IEEE Conference on*, 1994, pp. 2038-2041 vol.3.

[122] K. Zhou and J. C. Doyle, *Essentials of robust control* vol. 104: Prentice Hall Upper Saddle River, NJ, 1998.

[123] C. Scherer and S. Weiland, "Linear matrix inequalities in control," *Lecture Notes, Dutch Institute for Systems and Control, Delft, The Netherlands,* 2000.

[124] M. G. Villalva, T. G. de Siqueira, and E. Ruppert, "Voltage regulation of photovoltaic arrays: small-signal analysis and control design," *Power Electronics, IET,* vol. 3, pp. 869-880, 2010.

[125] D. Liberzon, *Switching in systems and control*: Springer, 2003.

[126] C. N. Onwuchekwa and A. Kwasinski, "Analysis of Boundary Control for Buck Converters With Instantaneous Constant-Power Loads," *IEEE Transactions on Power Electronics,* vol. 25, pp. 2018-2032, 2010.

[127] J. Zhang, J. S. Lai, and W. Yu, "Bidirectional DC-DC converter modeling and unified controller with digital implementation," in *Applied Power Electronics*

Conference and Exposition, 2008 APEC 2008 Twenty-Third Annual IEEE, 2008, pp. 1747-1753.

[128] S. Skogestad and M. Morari, "Implications of large RGA-elements on control performance," *Industrial & engineering chemistry research,* vol. 26, pp. 2323-2330, 1987.

[129] M. G. Villalva, J. R. Gazoli, and E. R. Filho, "Comprehensive Approach to Modeling and Simulation of Photovoltaic Arrays," *Power Electronics, IEEE Transactions on,* vol. 24, pp. 1198-1208, 2009.

[130] F. Garofalo, G. Celentano, and L. Glielmo, "Stability robustness of interval matrices via Lyapunov quadratic forms," *IEEE Transactions on Automatic Control,* vol. 38, pp. 281-284, 1993.

[131] F. Amato, *Robust control of linear systems subject to uncertain time-varying parameters* vol. 325: Springer Verlag, 2006.

[132] H. Horisberger and P. Belanger, "Regulators for linear, time invariant plants with uncertain parameters," *IEEE Transactions on Automatic Control,* vol. 21, pp. 705-708, 1976.

[133] P. P. Khargonekar and M. A. Rotea, "Stabilization of uncertain systems with norm bounded uncertainty using control Lyapunov functions," in *Decision and Control, 1988, Proceedings of the 27th IEEE Conference on*, 1988, pp. 503-507A vol.1.

[134] J. Geromel, P. L. D. Peres, and J. Bernussou, "On a convex parameter space method for linear control design of uncertain systems," *SIAM Journal on Control and Optimization,* vol. 29, p. 381, 1991.

[135] J. Bernussou, P. L. D. Peres, and J. C. Geromel, "A linear programming oriented procedure for quadratic stabilization of uncertain systems," *Systems & Control Letters,* vol. 13, pp. 65-72, 1989.

[136] M. Chilali and P. Gahinet, "H∞ design with pole placement constraints: an LMI approach," *IEEE Transactions on Automatic Control,* vol. 41, pp. 358-367, 1996.

[137] J. Doyle, "Analysis of feedback systems with structured uncertainties," *Control Theory and Applications, IEE Proceedings D,* vol. 129, pp. 242-250, 1982.

Vita

Ruichen Zhao was born in Changzhou, China in 1986. He received his B.S. degree (with Best Undergraduate Thesis Award) in electrical engineering from the Harbin Institute of Technology, in 2008 and the M.S. degree in electrical and computer engineering from The University of Texas at Austin, in 2010. He received the *IEEE IAS-PELS* Student Travel Grant in 2011 and *IEEE COMPEL* Student Travel Grant in 2012. Mr. Ruichen Zhao is a reviewer for the Energy Conversion Congress & Exposition (*ECCE*) and Applied Power Electronics Conference *(APEC*). He is also a reviewer for the *IEEE Transactions on Power Electronics*. His research interests include power electronics, micro-grids, and modeling and control of power converters. His industrial experience includes work at Samsung Electronics, Suwon, Korea. Upon graduation, Mr. Zhao will join Baker Hughes Incorporated as a Research Electrical Engineer.

Email address: rzhao@utexas.edu

This dissertation was typed by the author.